

**Stress-induced martensitic transformations in
Co₄₉Ni₂₁Ga₃₀ high-temperature shape memory alloy
single crystals**

Dissertation zur Erlangung des Doktorgrades

an der Fakultät für Geowissenschaften

der Ludwig-Maximilians-Universität München

Vorgelegt von

Alexander Reul

München, 08.09.2021

Betreuer: Prof. Dr. Wolfgang W. Schmahl

Erstgutachter: Prof. Dr. Wolfgang W. Schmahl

Zweitgutachter: Prof. Dr. Guntram Jordan

Tag der mündlichen Prüfung: 29.03.2022

Abstract

Co-Ni-Ga high-temperature shape memory alloys (HT-SMAs) are considered as promising candidates for applications as damping devices at elevated temperatures. This is due to their good processability, low costs of the alloying elements and fully reversible superelastic response up to 500 °C. In particular, the possibility to reach high-temperature superelasticity without significant plastic deformation opens up new research and application fields. This fact is related to strengthening of the material by segregation of γ' nanoprecipitates in the austenitic phase (precipitation-hardening). However, the functional behavior of the material is strongly dependent on microstructural mechanisms. Therefore, detailed experimental investigations using *in situ* neutron diffraction, optical- and confocal laser scanning microscopy were conducted in the present work to assess the domain variant selection, stress-induced martensite morphology and superelastic response in $\text{Co}_{49}\text{Ni}_{21}\text{Ga}_{30}$ HT-SMAs.

The results show, that the stress-induced martensitic phase in the as-grown condition is able to withstand about 5 % elastic strain in [001]-oriented Co-Ni-Ga at ambient temperature which significantly increases the overall deformation capability of this alloy system. In the precipitation-hardened material fundamentally different stress-induced martensite microstructures were uncovered compared to the precipitate-free solution-annealed state and the as-grown state. Aging treatments performed at 350 °C introduce γ' nanoprecipitates which reduce lamellar martensite plate thickness and increase the number of habit plane interfaces. Under compression, γ' nanoprecipitates trigger stress-induced martensite microstructures with multiple orientations of habit planes (multi-variant martensite microstructure) and multiple domain variants. Such kind of microstructure with significant variant-variant interactions in multi-variant microstructures have been supposed to increase the stress hysteresis width. However, under tensile load only one set of parallel habit planes and one single domain variant of stress-induced martensite (“fully detwinned”) appear in the presence γ' nanoprecipitates. The results clearly show that γ' nanoprecipitates do not necessarily promote multi-variant interaction during tensile loading. Thus, reduced strain recoverability in Co-Ni-Ga SMAs upon aging cannot be solely attributed to this kind of interaction as has been proposed so far.

Contents

1	Introduction.....	1
2	Theoretical background.....	4
2.1	Martensitic transformation	4
2.2	Thermodynamic properties.....	7
2.3	Shape memory behavior	10
2.3.1	Shape Memory Effect (SME).....	10
2.3.2	Two-way Shape Memory Effect (TWSME)	11
2.3.3	Superelasticity (SE).....	12
2.4	Factors affecting the shape memory characteristics	15
3	Co based shape memory alloys.....	20
4	Co-Ni-Ga shape memory alloys.....	22
5	Overview of publications and author contributions.....	30
6	Instrumental methods.....	32
6.1	Specimen preparation	32
6.2	<i>In situ</i> optical microscopy (OM)	33
6.3	<i>In situ</i> neutron diffraction	34
6.3.1	<i>In situ</i> neutron diffraction (SXD).....	34
6.3.2	<i>In situ</i> neutron diffraction (STRESS-SPEC).....	36
6.4	Transmission electron microscopy	37
7	Experiments	38
7.1	<i>In situ</i> Neutron Diffraction Analyzing Stress-Induced Phase Transformation in [001]-oriented Co ₄₉ Ni ₂₁ Ga ₃₀ Shape Memory Alloy Single Crystals.....	38
7.1.1	Aim of this study	38
7.1.2	Experimental details	38
7.1.3	Results	39
7.1.4	Discussion	43

7.2	Effect of nanometric γ' precipitates on the stress-induced martensitic transformation in [001]-oriented $\text{Co}_{49}\text{Ni}_{21}\text{Ga}_{30}$ shape memory alloy single crystals	47
7.2.1	Aim of this study	47
7.2.2	Experimental details	47
7.2.3	Results and discussion.....	48
7.3	On the impact of nanometric γ' precipitates on the tensile deformation of superelastic $\text{Co}_{49}\text{Ni}_{21}\text{Ga}_{30}$	55
7.3.1	Aim of this study	55
7.3.2	Experimental details	55
7.3.3	Results	57
7.3.4	Discussion	66
8	Conclusions.....	72
9	References.....	76
10	Appendix	86

Abbreviations

A_f	Austenite finish temperature
A_s	Austenite start temperature
BCV	Bain-correspondence variant
CLSM	Confocal laser scanning microscopy
CVP	Correspondent variant pair
DSC	Differential scanning calorimetry
EDM	Electro-discharge machining
HARTEM	High-resolution transmission electron microscopy
HPV	Habit plane variant
HT-SMA	High-temperature shape memory alloy
M_d	Highest temperature above which martensite can no longer be stress-induced
M_f	Martensite finish temperature
M_s	Martensite start temperature
MT	Martensitic transformation
ND	Neutron diffraction
OM	Optical microscopy
PSD	Position-sensitive detector
SAED	Selected area electron diffraction
SE	Superelasticity
SIM	Stress-induced martensite
SMA	Shape memory alloy
SME	Shape memory effect
TEM	Transmission electron microscopy
TOF	Time-of-flight
TWSME	Two-way shape memory effect

1 Introduction

The demand for shape memory alloys (SMAs) as promising functional materials for actuators and damping devices has grown significantly in the last decades (Duerig et al. 1999; Otsuka and Wayman 1999; Lagoudas 2008; Ma et al. 2010; Mohd Jani et al. 2014). Their unique functional properties are based on a diffusionless and fully recoverable solid-to-solid phase transformation from high temperature austenite to low temperature martensite. The ability to recover a high amount of transformation strain is possible by heating (shape memory effect (SME)), unloading (superelasticity (SE)) or heating and cooling under isobaric conditions (two way shape memory effect (TWSME)) (Otsuka and Wayman 1999; Lagoudas 2008). The discovery of the shape memory effect in equiatomic Ni-Ti in 1963 (Buehler et al. 1963) was groundbreaking for the SMA research field. NiTi SMAs exhibit a maximum transformation strain of 10 % (Miyazaki et al. 1984) and excellent plastic slip resistance with a stable response over many cycles (Strnadel et al. 1995; Gall and Maier 2002). Currently, binary Ni-Ti (also referred to as Nitinol, NiTi) is the most widely employed functional metallic material due to the excellent corrosion resistance (Rondelli 1996), high damping properties (Van Humbeeck 2003), good biocompatibility (Es-Souni et al. 2005) and the excellent strength and ductility (Miyazaki et al. 1981, 1991). Particularly, the demand for functional materials in automotive, aerospace and turbine engine industries has grown significantly, where the operation temperatures often exceed 100 °C (Otsuka and Wayman 1999; Hartl and Lagoudas 2007; Lagoudas 2008; Ma et al. 2010). Thus, ternary Ni-Ti-X alloys (X = Zr, Hf, Au, Pt, Pd) have been designed to increase the transformation temperatures (Golberg et al. 1995; Hsieh and Wu 1998; Besseghini et al. 1999; Firstov et al. 2004; Noebe et al. 2005; Padula et al. 2008; Stebner et al. 2014; Evirgen et al. 2015). In this regard, SMAs with transformation temperatures above 100 °C are referred to as high-temperature shape memory alloys (HT-SMAs). Currently, Ni-Ti-Hf HT-SMAs impart remarkable functional properties exceeding transformation temperatures of 400 °C (Sehitoglu et al. 2017). However, the demand for high amounts of noble metals (Au, Pt, Pd) is associated with high production costs, and alloying Ni-Ti with refractory elements (Zr, Hf) causes limited workability due to pronounced brittleness (Ma et al. 2010). Additionally, key criteria for high-temperature applicability are long term microstructural and functional stability and high resistance against plastic deformation (Lagoudas 2008; Ma et al. 2010). However, the operation of NiTi SMAs is limited to 75 °C (Sehitoglu et al. 2000, 2017). In particular, thermal instabilities and activation of slip remain challenging problems as they

promote functional degradation impeding the transformation recoverability (Miyazaki et al. 1986).

In recent years, Heusler-type Co-Ni-Ga SMAs turned out to be promising alternatives for applications at elevated temperatures, due to improved formability by controlled ductile γ -phase formation (disordered fcc) within the β -phase matrix (Oikawa et al. 2001). In addition, the relatively inexpensive alloying element of this system compared to Ni-Ti-Hf alloys, are attractive for industrial applications (Ma et al. 2010). A large SE response with a fully reversible stress-induced martensitic transformation up to 500 °C and excellent long-term cyclic stability without functional degradation up to 100 °C have been shown in single crystalline material (Dadda et al. 2006; Krooß et al. 2015, 2016), qualifying Co-Ni-Ga for high-temperature damping applications. In addition, appropriate heat treatment procedures have been shown to open up new possibilities for actuator applications at elevated temperatures by aging in the stress-induced martensitic phase, referred to as SIM-aging. As pointed out by Niendorf et al. (2015) and Lauhoff et al. (2018) SIM-aging brought an increase of the transformation temperatures by about 150 °C as well as a fully reversible martensitic transformation upon thermo-mechanical cycling. As dislocation slip is suppressed in the $\{110\}(001)$ slip system, most of the work on Co-Ni-Ga was addressed to single crystals in $[001]$ -orientation in order to study the fundamental mechanisms in this alloy system. Co-Ni-Ga single crystals in $[001]$ orientation reveal large maximum SE strains of -4.6 % and 8.6 % in compression and tension, respectively, as well as excellent functional properties as compared to single crystals of other orientations or polycrystals (Dadda et al. 2006, 2008; Chernenko et al. 2007; Monroe et al. 2010; Niendorf et al. 2013; Vollmer et al. 2015; Lauhoff et al. 2018). In particular, polycrystalline Co-Ni-Ga alloys often suffer from intergranular fracture upon thermomechanical processing due to the pronounced anisotropic transformation behavior (Dadda et al. 2008; Vollmer et al. 2015; Lauhoff et al. 2019b). However, substantial progress has been made very recently in terms of the establishment of robust processing routes and improved functional performance. Via hot extrusion (Karsten et al. 2019; Niendorf et al. 2019) and additive manufacturing (Lauhoff et al. 2020b, 2020a) microstructures characterized by minimized grain constraints have been introduced featuring high damage tolerance and good functional properties.

Furthermore, precipitation hardening at intermediate-temperature aging treatments effectively improves the functional properties at elevated temperatures. This has been shown in various

SMAAs (Miyazaki et al. 1983; Pons et al. 1993; Cesari et al. 1994; Shimizu et al. 1998; Sehitoglu et al. 2000; Gall and Maier 2002). In Co-Ni-Ga SMAAs for instance, the introduction of γ' nanoprecipitates increases the yield strength of the material (Chumlyakov et al. 2008, 2012; Kireeva et al. 2013, 2014). However, the size and morphology (spherical or elongated) of γ' nanoprecipitates modifies the martensitic microstructure and strongly affects the functional properties in Co-Ni-Ga SMAAs (Kireeva et al. 2013, 2014). It is of utmost importance to characterize the impact of martensitic microstructures with respect to the mechanical material behavior which is necessary for potential industrial applications. Up to now, the effect of γ' nanoprecipitates on the functional properties in Co-Ni-Ga SMAAs was mainly investigated in thermally induced martensite (Kireeva et al. 2013, 2014). So far, no studies are available discussing the role of morphology and domain variant selection of stress-induced martensite. Hence, detailed investigations were carried out on single crystalline Co-Ni-Ga SMAAs to assess the effect of γ' nanoprecipitates on stress-induced martensite under compressive and tensile single cycle superelastic deformation.

Mackenzie and Bowles 1954; Otsuka and Wayman 1999; Lagoudas 2008). The unit vectors characterizing the normal of the habit plane and the transformation direction are denoted as n and m , respectively. The transformation is accompanied by a shape change and can be broken into two components: A shear component along m_x (invariant plane strain (IPS)), while the dilatation component perpendicular to the habit plane along m_y represents a small distortion. The invariant plane strain is obtained by coordinated atomic displacements which convert the initial austenite to the final martensite lattice (Bowles and Mackenzie 1954; Mackenzie and Bowles 1954). In the final martensite structure this invariant plane strain is a simple shear on a twinning plane or in twinning direction (Bowles and Mackenzie 1954). During martensitic transformation a spontaneous strain arises around martensite which is associated with the shape change and the corresponding mismatch in crystal lattice between martensite and austenite (Otsuka and Wayman 1999; Ma et al. 2010). Consequently, strain reduction is attained either by introducing slip or twins as shown in Fig. 2.2.

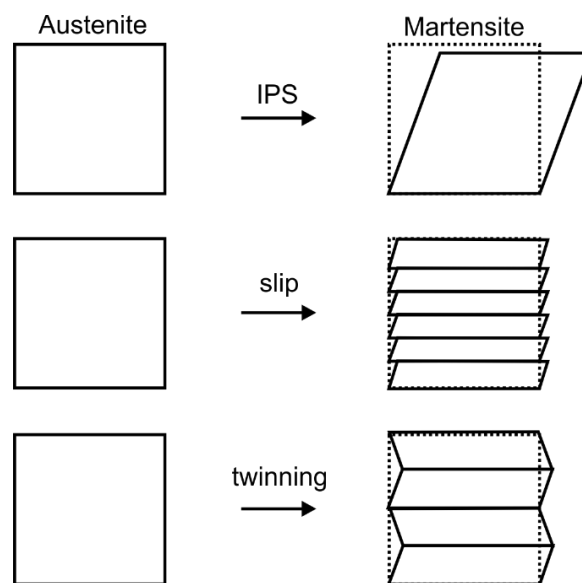


Fig. 2.2: Schematic of the shape change upon martensitic transformation and strain reduction (accommodation) by introducing slip or twins (modified after Otsuka and Wayman 1999).

Slip deformation and twinning results in the formation of a self-accommodated martensite microstructure without macroscopic shape change (Otsuka and Wayman 1999; Lagoudas 2008). However, slip leads to plastic and irreversible deformation of the material, whereas twinning in martensite enables a crystallographically reversible phase transformation to the

initial austenite configuration. Both mechanisms depend on the type of alloy (Otsuka and Wayman 1999). In SMAs twinning of martensite is favored to accommodate the strain which gives SMAs their unique properties (Bhattacharya 2003). Consequently, the composition of the alloy has to be adjusted to increase the resistance against plastic deformation (Otsuka and Wayman 1999).

A typical observable feature in SMAs is the twinned martensite microstructure which comprises two symmetry-related martensite domain variants (V_1 and V_2), termed correspondent variant pair (CVP) as shown schematically in Fig. 2.3. Domain variants have the same structure but their orientations are different (Otsuka and Wayman 1999; Bhattacharya 2003; Ma et al. 2010). When the martensite lattice is obtained from the austenite lattice a stress-free twin plane between two domain variants forms the twin interface (Otsuka and Wayman 1999; Bhattacharya 2003). This structural change produces different regions of the crystal exhibiting domain patterns of symmetry-related domain variants of martensite in a length scale of nanometers up to tenths of millimeters (Bhattacharya 2003).

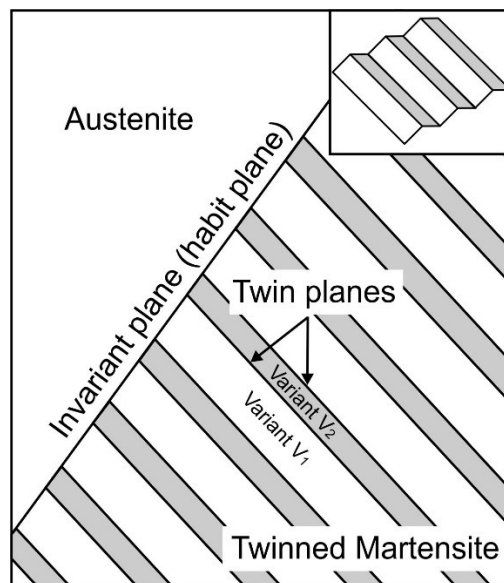


Fig. 2.3: Schematic of a twinned martensitic microstructure separated by the habit plane interface from austenite. The domain pattern of martensite is composed of twin-related domain variants V_1 and V_2 . The topography of the domain pattern is highlighted by the inset. (modified after Lagoudas 2008).

It is worth noting, that low magnifications enable only the visualization of martensite plates by an optical contrast. In order to reveal domain patterns of martensitic microstructures a higher

magnification is required. Based on the high mobility of twin planes and habit plane interfaces martensitic phase transformations are crystallographically reversible. In this case the shape memory response is characterized by a narrow transformation hysteresis and the driving force is very small as shown in Fig. 2.4 for an Au-Cd alloy (Otsuka and Wayman 1999). This type of reversible transformation is referred to as thermoelastic.

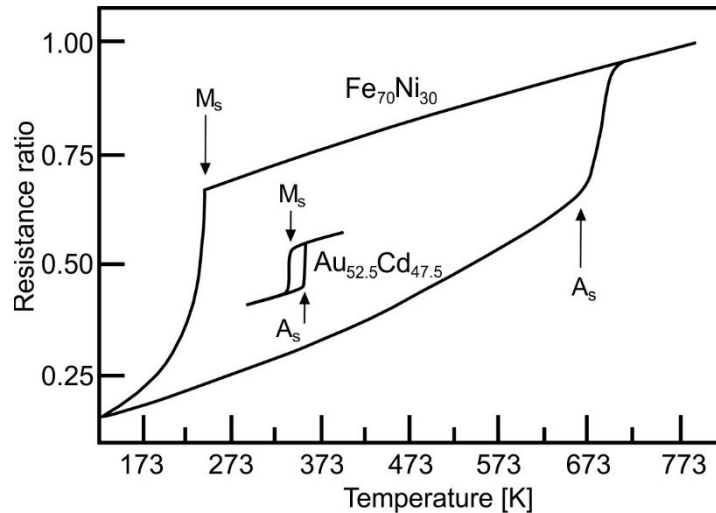


Fig. 2.4: Electrical resistance as a function of temperature of Au-Cd (thermoelastic) and Fe-Ni (non-thermoelastic) alloys during heating and cooling (modified after Kaufman and Cohen 1958).

On the other hand, a large transformation hysteresis is associated with a large driving force as demonstrated in the Ni-Fe alloy. This fact is attributed to immobile austenite-martensite interfaces and the reverse transformation occurs by the renucleation of austenite which is denoted as non-thermoelastic (Otsuka and Wayman 1999).

2.2 Thermodynamic properties

The martensitic transformation may be represented by the Gibbs free energies G for austenite and martensite phases as a function of temperature T :

$$G = H - TS \quad (1)$$

H is the enthalpy and S the entropy of the thermodynamic system. The Gibbs free energies of austenite G_A and martensite G_M as a function of temperature are schematically illustrated in Fig. 2.5. The Gibbs free energy curves of austenite and martensite intersect at the thermodynamic equilibrium temperature T_0 , where the Gibbs free energies of both phases are

equal. At temperatures different than T_0 the phase with the lower Gibbs free energy is thermodynamically stable. In this case, martensite is the stable phase below T_0 , whereas austenite is the stable phase above T_0 . However, a driving force is required for thermally induced phase transformations which is correlated with a shift in transformation temperatures with respect to the equilibrium temperature T_0 . Correspondingly, undercooling ΔT^- initiates the nucleation of martensite during the forward transformation and superheating ΔT^+ the reverse transformation from martensite to austenite.

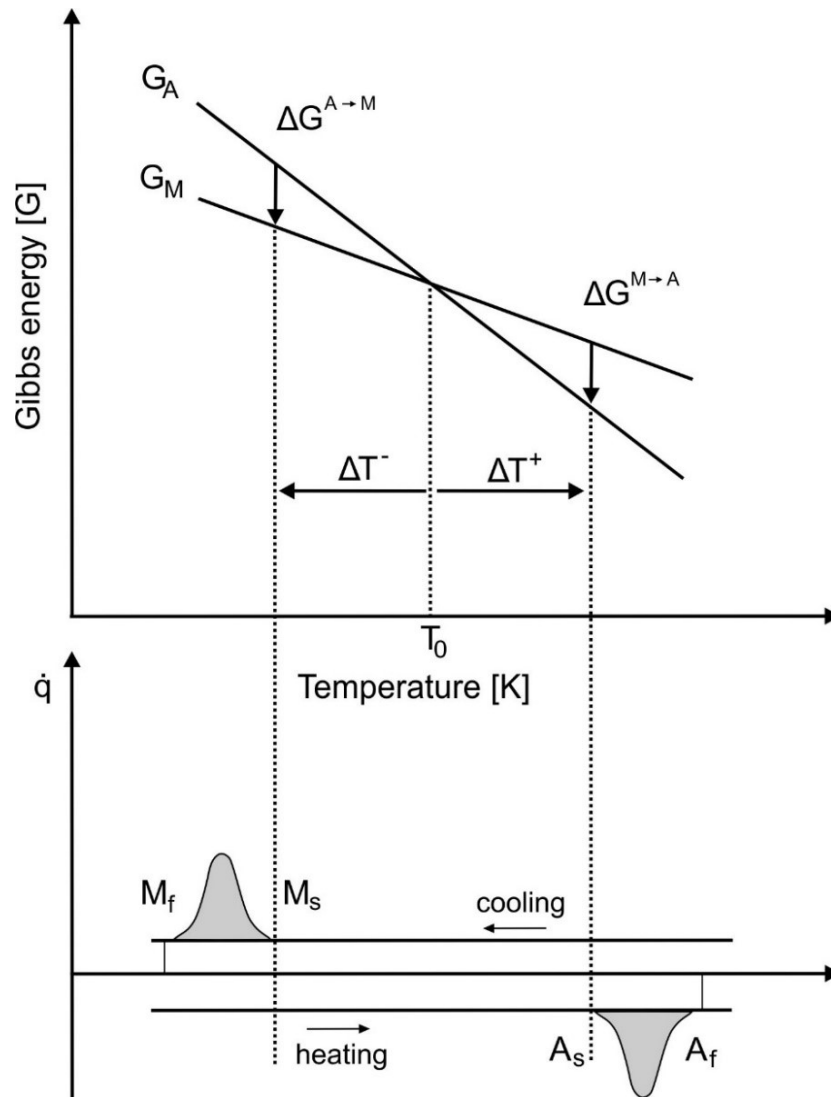


Fig. 2.5: Schematic representation of the Gibbs free energies of martensitic and austenitic phases in relation to the M_s and A_s temperatures. The driving force ΔT is required for thermally induced martensitic transformation. The DSC curve for an SMA shows the transformation temperatures and the associated heat flow as a function of temperature (Schäfer 2012, modified after Otsuka and Wayman 1999; Lagoudas 2008).

Thus, the transformation to martensite and austenite occurs at certain transformation temperatures denoted as martensite start temperature M_s and austenite start temperature A_s , respectively. The difference in Gibbs free energies ΔG upon martensitic transformation may be written as follows:

$$\Delta G = \Delta G_c + \Delta G_s + \Delta G_e = \Delta G_c + \Delta G_{nc}, \quad (2)$$

where ΔG_c is a chemical energy term due to the structural change between both phases, ΔG_s is a surface term between austenite and martensite phase and ΔG_e is an elastic energy term around martensite which is associated with the shape and volume changes of the transformation. The non-chemical term is represented by $\Delta G_{nc} = \Delta G_s + \Delta G_e$ (Otsuka and Wayman 1999). The difference between T_0 and the transformation temperatures is associated with the non-chemical contribution and can be interpreted by frictional stress at interface boundaries and the stored elastic energy around martensite which resist the phase transformation. As a consequence, start and finish transformation temperatures are not the same and further driving force is required to support the martensitic transformation (Otsuka and Wayman 1999). Thus, during the forward transformation martensite formation is completed at the martensitic finish temperature (M_f). Conversely, during the reverse transformation austenite formation is completed at the austenite finish temperature (A_f). A standardized testing method of the phase transformation temperatures in engineering applications is Differential Scanning Calorimetry (DSC). As shown in Fig. 2.5, the heat flow is measured as a function of temperature to determine the transformation temperatures of the material. During heating and cooling a transformation peak is recorded which represents the endothermic (additional heat required for austenite formation) and exothermic (release of latent heat during martensite formation) transformation, respectively (Otsuka and Wayman 1999; Lagoudas 2008).

There is also a stress induced phase transformation in addition to thermally induced martensite. The linear relationship between the level of stress and the transformation temperature under uniaxial load is represented by the Clausius-Clapeyron relationship (Otsuka and Wayman 1999; Otsuka and Ren 2005):

$$\frac{d\sigma}{dT} = \frac{\Delta H}{\varepsilon T_0}, \quad (3)$$

where σ is a uniaxial stress, ε a transformation strain and ΔH the enthalpy of the transformation. In stress-temperature space each of these transformation temperatures (M_s , M_f , A_s , A_f) follows

the Clausius-Clapeyron relationship approximately as a straight line as shown in $\sigma - T$ space (Fig. 2.9)

2.3 Shape memory behavior

In general, shape memory behavior may be represented by three mechanisms such as the shape memory effect (SME), superelasticity (SE) and the two-way shape memory effect (TWSME). Thereby, temperature reduction (SME, TWSME) or application of stress (SE) act as driving forces to induce the martensitic phase transformation. In the following, the shape memory behavior is represented on $\sigma - T$ and $\sigma - T - \varepsilon$ diagrams.

2.3.1 Shape Memory Effect (SME)

Cooling austenite (A in Fig. 2.6) without external applied stress below M_f results in the formation of a twinned martensite microstructure (B). When twinned martensite is subjected to an external applied stress that exceeds the critical transformation stress level σ_s , certain domain variants rearrange and a new microstructure is formed. In this case, domain variants energetically favored with respect to the applied stress grow at the expense of others by reorientation and detwinning to accommodate the deformation (Otsuka and Wayman 1999; Bhattacharya 2003; Lagoudas 2008). The stress-strain response appears as a plateau due to the high twin boundary mobility. Complete detwinning (C) of martensite occurs at load levels above the detwinning finish stress σ_f at the end of the stress-strain plateau which gives the largest transformation strain. Further loading beyond the stress-strain plateau results in the elastic deformation of martensite. After unloading (D) the specimen remains in the detwinned martensitic state which leads to an external shape change. Subsequent heating in the absence of stress to a temperature above A_s initiates the reverse transformation to austenite which is completed at A_f . Above A_f only the parent austenitic phase is stable. Thereby the original shape and the transformation strain from detwinning are recovered (E). Cooling back to a temperature below M_f leads to the formation of self-accommodated martensite with no associated shape change (Otsuka and Wayman 1999; Lagoudas 2008; Ma et al. 2010). This mechanism is referred to as the shape memory effect (SME), or one-way shape memory behavior since only the austenite shape is memorized (Otsuka and Ren 2005; Ma et al. 2010).

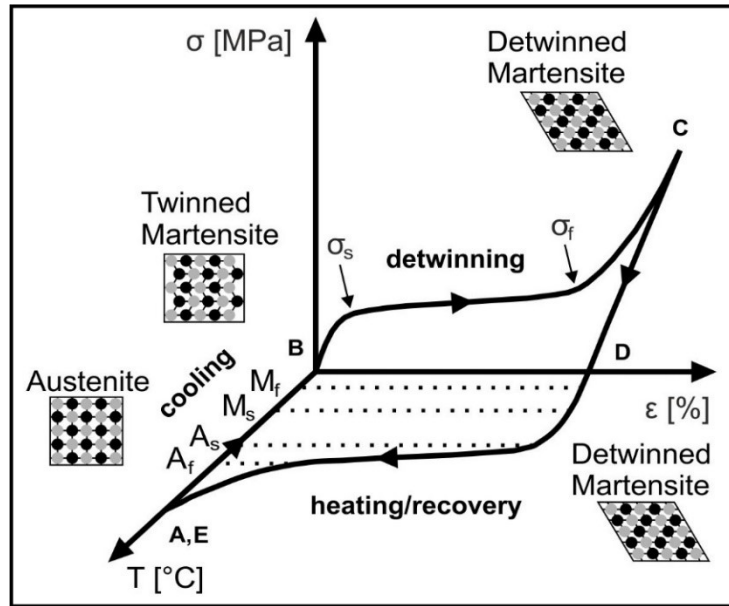


Fig. 2.6: Demonstration of the SME in the $\sigma - T - \varepsilon$ diagram. Cooling austenite (A) below M_f leads to the formation of self-accommodated martensite (B). Deformation of martensite below M_f causes detwinning (C). Martensite remains in the detwinned configuration after removal of the external applied stress (D). Heating above A_f restores the austenitic (E) state (modified after Lagoudas 2008).

2.3.2 Two-way Shape Memory Effect (TWSME)

The two-way shape memory effect enables a repeatable shape change in a thermally induced martensitic transformation without applied mechanical load as shown in Fig. 2.7. This behavior necessitates subsequent thermomechanical treatments of the material over a large number of cooling and heating cycles under constant applied load which is referred to as “training” or isobaric thermal cycling (Lagoudas 2008; Ma et al. 2010; Sehitoglu et al. 2017). Cooling austenite under applied load may induce dislocations and inelastic strains in the microstructure of martensite. Consequently, the residual internal stress fields created around dislocations stabilize a martensite configuration with preferred domain variants (Otsuka and Wayman 1999; Lagoudas 2008). Reheating the material under constant applied load results in the reverse transformation to austenite. Repeated thermomechanical training recovers the inelastic strains and stabilizes the hysteretic response of the material. As a result, trained specimens exhibit TWSME which enables the switching between austenite and a certain martensite microstructure just by temperature change. This behavior is termed two-way shape memory effect, since a

martensite shape different from that of austenite is memorized (Otsuka and Ren 2005; Ma et al. 2010).

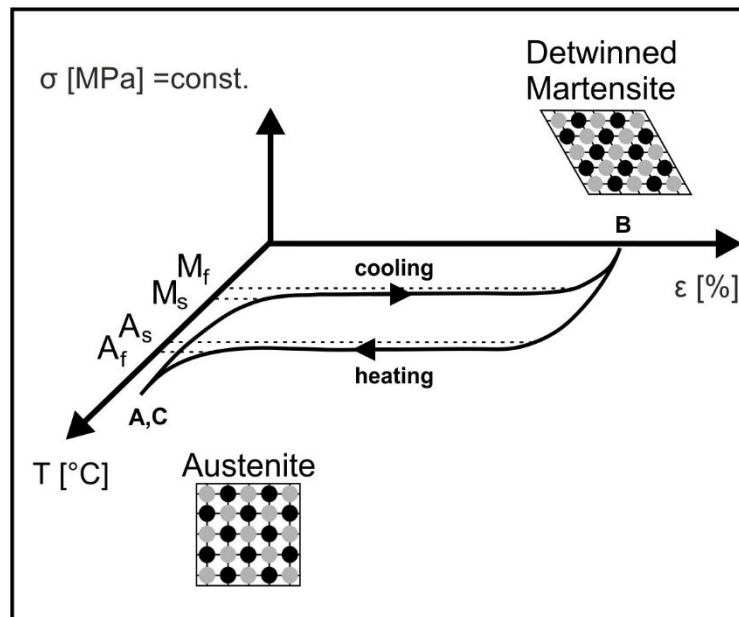


Fig. 2.7: TWSME is demonstrated using the $\sigma - T - \varepsilon$ diagram. “Training” of thermally induced martensite under constant applied stress is a prerequisite to employ TWSME. (modified after Lagoudas 2008).

2.3.3 Superelasticity (SE)

In addition to thermally induced martensitic transformation, superelasticity occurs when a SMA is subjected to an external stress above A_f . Initially, austenite (A in Fig. 2.8) is the stable phase and deforms linear elastically upon loading. The departure of the SE curve from the linear elastic behavior of austenite is marked by the onset of a critical transformation stress level (σ_{M_s}). Upon further loading the formation of stress-induced martensite (SIM) proceeds which is associated by a favorable growth of domain variants in load direction, a continuous increase in transformation strain and a plateau-type character of the superelastic stress-strain curve (Lagoudas 2008; Ma et al. 2010). Once the critical transformation stress level σ_{M_f} is reached the transformation from austenite to stress-induced martensite is complete. As the loading proceeds the ascending stress strain curve is attributed to elastic deformation of martensite (B). Stress induced martensitic transformations may produce twinned or detwinned microstructures of martensite which depends on the orientation of the specimen (Gall and Maier 2002; Dadda et al. 2008) or microstructural properties (Kireeva et al. 2014). Upon unloading SIM becomes

unstable during the reverse transformation and begins to transform back to austenite at a critical transformation start stress level σ_{As} . Exceeding σ_{Af} the transformation to austenite (C) is finished (Otsuka and Wayman 1999; Lagoudas 2008; Ma et al. 2010).

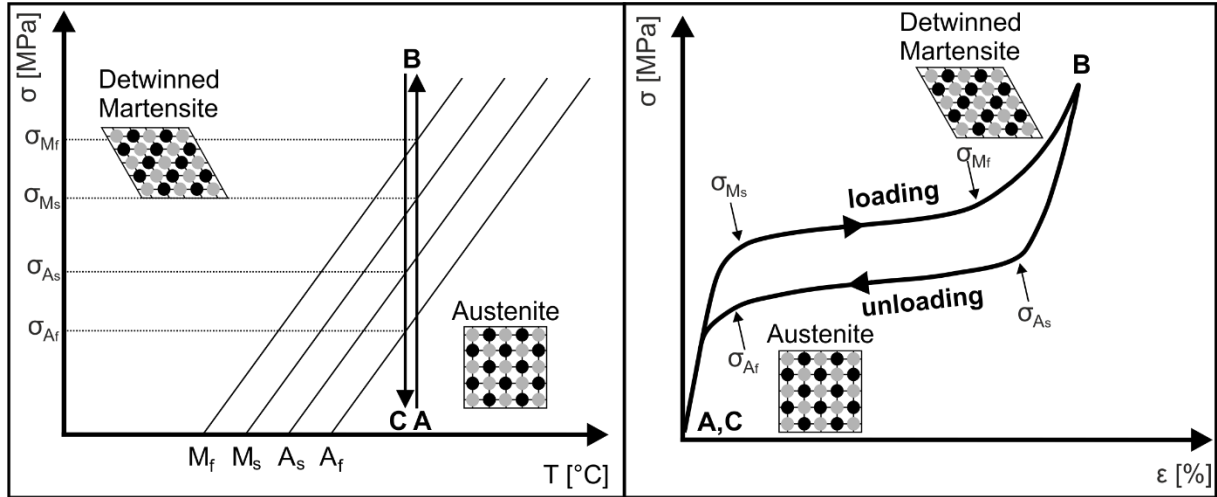


Fig. 2.8: SE is demonstrated using the $\sigma - T$ and $\sigma - \epsilon$ diagram. Austenite is deformed above A_f (A). SIM transformation is finished above σ_{Mf} , followed by an elastic deformation of SIM (B). Austenite (C) is recovered upon unloading (modified after Lagoudas 2008).

Superelasticity (SE) is observed in a certain stress-temperature region, referred to as “superelastic window” (Ma et al. 2010). In general, the austenite finish temperature A_f , the critical transformation stress to induce martensite σ_{Ms} and the critical stress for slip σ_y (yield stress of austenite) constrain the dimension of the superelastic window as depicted in Fig. 2.9. Superelasticity occurs above A_f , where the martensitic phase is completely unstable in the absence of stress (Otsuka and Wayman 1999; Otsuka and Ren 2005). The straight line with the positive slope represents the temperature dependence of the critical transformation stress σ_{Ms} , following the CC-relationship. The critical transformation stress to induce martensite increases with increasing temperature, because the austenitic phase becomes more stable at higher test temperature (Otsuka and Wayman 1999; Ma et al. 2010; Sehitoglu et al. 2017). Thus, when the difference between A_f and the test temperature becomes larger, a greater driving force (σ_{Ms}) is required to initiate the stress-induced martensite formation. The straight line with the negative slope represents the yield stress of austenite σ_y (A and B). It decreases with increasing temperature (Otsuka and Wayman 1999). The intersection of the critical transformation stress σ_{Ms} with the yield stress of austenite σ_y (A) defines the temperature M_d . Above the M_d temperature martensite can no longer be stress-induced and plastic deformation occurs first.

Since slip does not recover upon unloading the applied stress must be below σ_y (A) to avoid irreversible processes in the material (Ma et al. 2010; Sehitoglu et al. 2017). If the critical transformation stress is as low as the yield stress of austenite in the dashed line (σ_y B), slip occurs prior to the onset of stress-induced martensite (SIM) and SE is not realized (Otsuka and Wayman 1999). Slip activity is strongly dependent on crystallographic orientation. For instance, Gall and Sehitoglu (1999) showed that single crystalline NiTi SMAs possess a lower slip activity and higher fatigue resistance in [100] orientation as compared to the [111] orientation. It is worth noting, that SME and SE are observable in the same specimen, depending on the test temperature. SME occurs below A_s , followed by heating above A_f , while SE occurs above A_f . In the temperature regime between A_s and A_f both are realized partially (Otsuka and Wayman 1999).

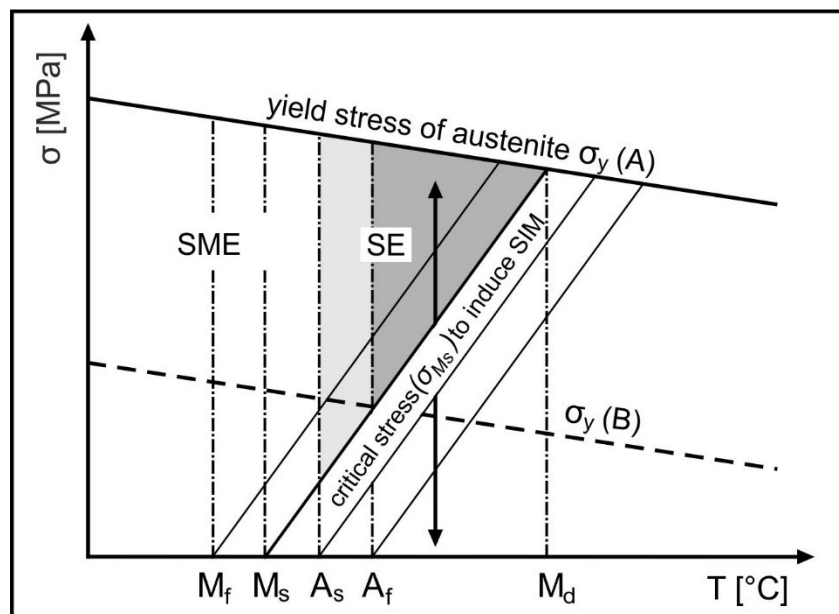


Fig. 2.9: Schematic $\sigma - T$ diagram representing the region of superelasticity (SE, highlighted in dark grey) and shape memory effect (SME). Superelasticity is observed between A_f and M_d . (A) represents the transformation stress for a high yield stress of austenite σ_y . (B) represents the transformation stress for a low yield stress of austenite σ_y (modified after Otsuka and Wayman 1999).

The stress-strain relationship reflects an elastic stress hysteresis $\Delta\sigma$, which is characterized by a difference in stress between the forward and reverse branch of the superelastic stress-strain curve (Fig. 2.10). The stress hysteresis width ($\Delta\sigma$) is linked to energy dissipation occurring during martensitic phase transformation in addition to the irrecoverable (residual) strain (ϵ_{irr}) and the critical transformation stress to induce SIM (σ_{crit}). These properties are measures of the

dissipation of the driving force through irreversible processes and reflect the cyclic stability (number of exploitable transformation cycles) of the material (Lagoudas 2008; Ma et al. 2010).

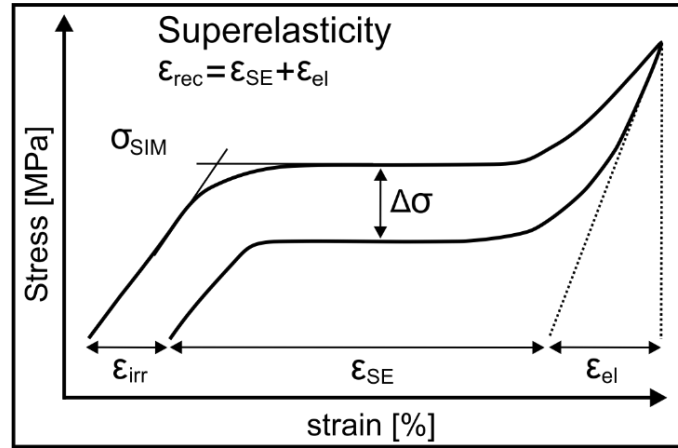


Fig. 2.10: The schematic of a superelastic stress-strain curve illustrates the irrecoverable strain ϵ_{irr} , the critical transformation stress to induce SIM (σ_{crit}) and the stress hysteresis width ($\Delta\sigma$).

2.4 Factors affecting the shape memory characteristics

Important properties in SMA applications are large recoverable transformation strain levels and resistance against plastic deformation imparting long term cyclic stability. However, numerous irreversible processes such as plastic deformation through slip and microstructural instabilities strongly affect the transformation characteristics of SMAs. In particular, the accumulation of irrecoverable strain due to slip deformation results in rapid degradation of functional properties (Miyazaki et al. 1986; Gall and Maier 2002).

Extensive work on the superelastic characteristics of Ni-Ti during cyclic deformation was conducted by Miyazaki et al. (1986). This study demonstrated functional degradation of the superelastic stress-strain response with increasing number of cycles as shown in Fig. 2.11. The effect of cyclic deformation featured an increase of residual strain (ϵ_{irr}), a decrease in critical transformation stress (σ_{crit}) and a decrease of stress hysteresis ($\Delta\sigma$). Furthermore, the authors demonstrated the dependence of cyclic degradation on stress and test temperature, i.e. cyclic degradation increased with increasing stress and test temperature. The change of the superelastic stress-strain response during cyclic deformation was attributed to the generation of dislocations (Miyazaki et al. 1986). In particular, slip deformation and stabilization of the

martensitic phase due to dislocation activities were considered to be causes for the occurrence of residual strain during cyclic deformation as already pointed out by Melton and Mercier (1979). The formation of internal stress fields due to dislocation slip support the stabilization of the martensitic phase (Miyazaki et al. 1986). In this case the mobility of moving austenite/martensite phase boundaries decreases in the vicinity of dislocations. This process is referred to as pinning-induced martensite stabilization (Kustov et al. 2004).

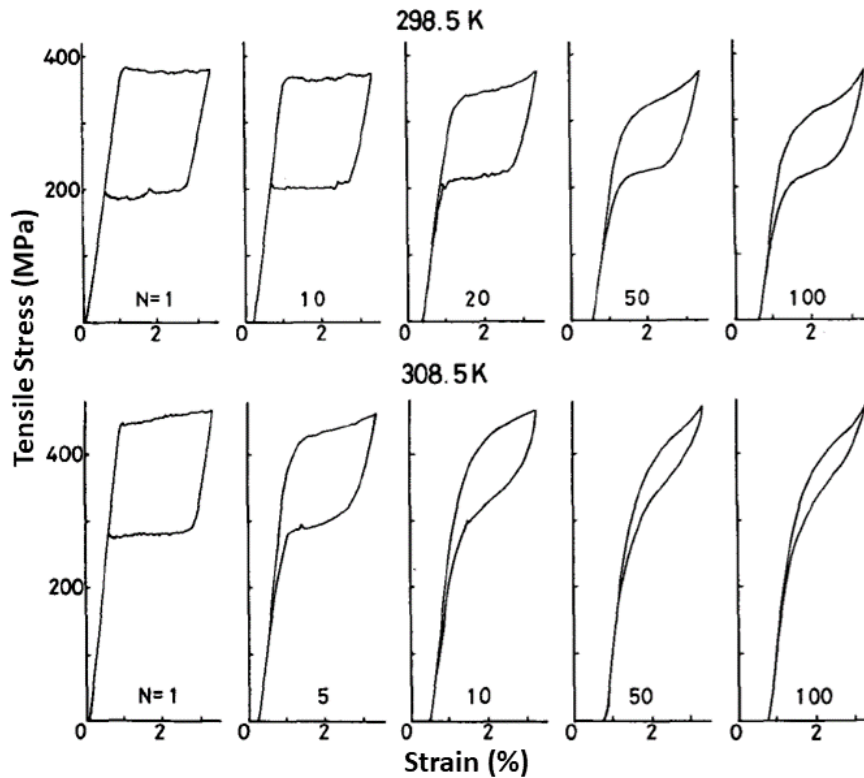


Fig. 2.11: Superelastic stress-strain curves of the $Ni_{49.5}Ti_{50.5}$ alloy for $N = 1, 10, 20, 50$ and 100 cycles. Enhanced functional degradation with increasing numbers of cycles. This effect is more pronounced at higher test temperature (modified after Miyazaki et al. 1986).

As a consequence, the critical transformation stress for inducing martensite decreases in the subsequent cycle due to the stabilization of the martensitic phase. Hence, with increasing number of cycles the residual (stabilized) martensitic phase increases in volume. However, the residual strain, critical transformation stress and stress hysteresis values saturate with increasing number of cycles and steady state superelastic characteristics occur (Miyazaki et al. 1986). In order to improve the cyclic deformation capability, it is important to raise the yield strength of the austenite matrix and thus the resistance against dislocation slip (Miyazaki et al. 1983) by a proper choice of heat treatment. Consequently, the precipitation process in Ni rich NiTi alloys

can be used to tailor the functional properties (Miyazaki et al. 1982; Nishida et al. 1986). In addition, Ti_3Ni_4 precipitates lead to the formation of large local stress fields and local changes of the chemical composition in the matrix (Gall et al. 1999) as illustrated in Fig. 2.12.

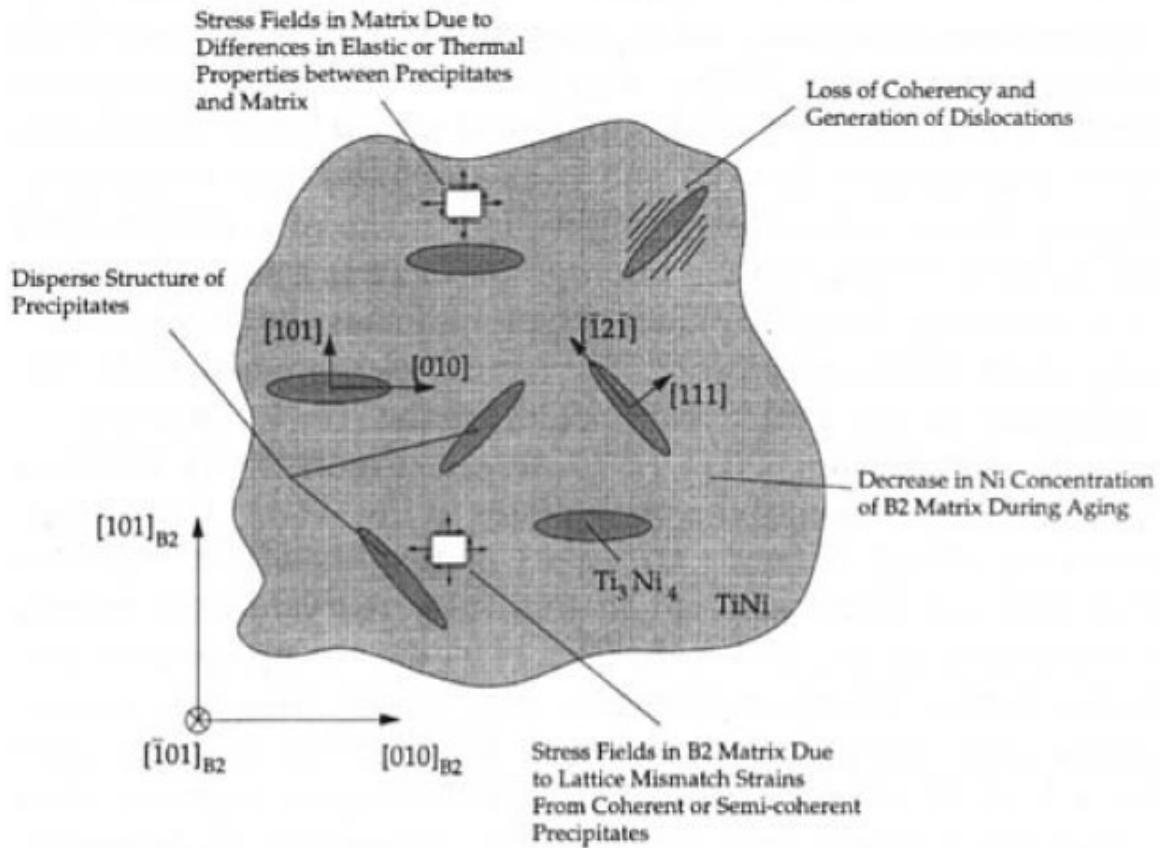


Fig. 2.12: Schematic of Ti_3Ni_4 precipitate interactions with the matrix in Ni-Ti (Gall et al. 1999, reproduced with permission from American Society of Mechanical Engineers ASME).

Related work (Gall and Maier 2002) uncovered that the cyclic degradation resistance and transformation characteristics strongly depend on size and coherency of Ti_3Ni_4 precipitates in addition to dislocation activity and martensite stabilization. Small coherent Ti_3Ni_4 precipitates (10 nm) improved the degradation resistance as compared to large incoherent Ti_3Ni_4 precipitates (500 nm). The residual strain and stress hysteresis, as a measure for the cyclic stability of the material, are less pronounced in Ni-Ti containing small coherent Ti_3Ni_4 precipitates (Fig. 2.13a) compared to NiTi containing large incoherent Ti_3Ni_4 precipitates (Fig. 2.13b).

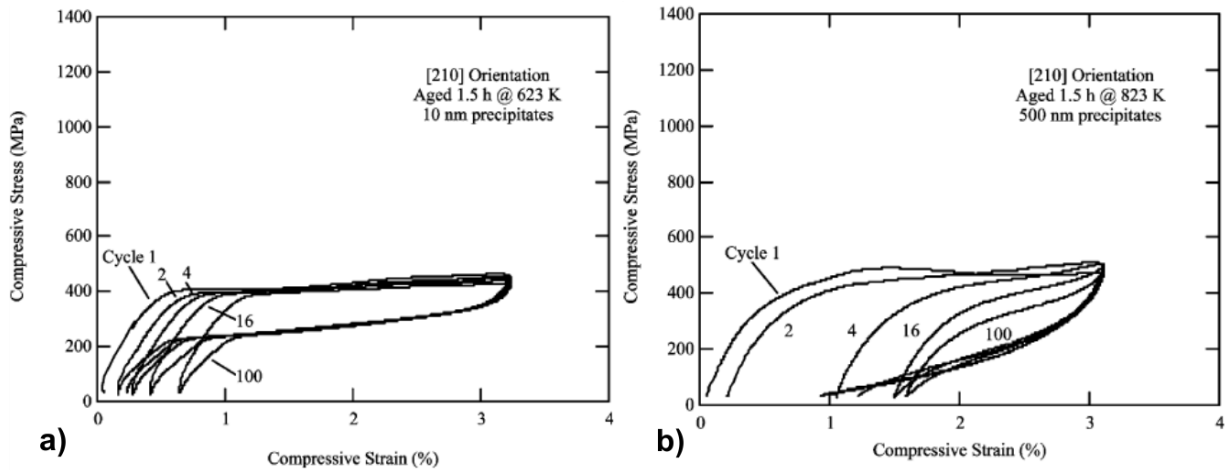


Fig. 2.13: Cyclic superelastic stress-strain curves of $[210]$ oriented NiTi single crystals after different heat treatments, i.e. (a), aged at 350°C for 1.5 h and (b) aged at 550°C for 1.5 h (Gall and Maier 2002, reproduced with permission from Elsevier).

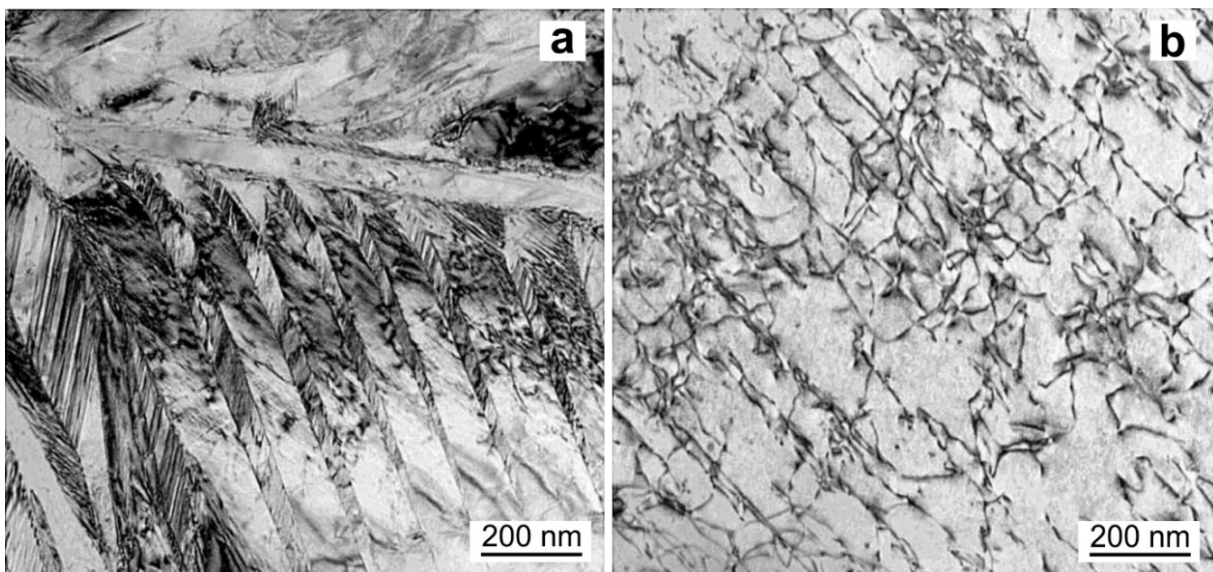


Fig. 2.14: TEM images of a Ni-Ti single crystal containing large incoherent Ti_3Ni_4 precipitates (500 nm). Stabilized martensitic phase (a) and pronounced dislocation activity (b) due to mechanical cycling (Gall and Maier 2002, reproduced with permission from Elsevier).

Heat treatment on Ni-Ti producing small coherent Ti_3Ni_4 precipitates prevented the formation of dislocations during stress-strain cycling. However, strong local stress fields developed in the Ni-Ti matrix due to the lattice mismatch between the Ti_3Ni_4 precipitates and the matrix (Martin 1980; Gall et al. 1999). This fact supported the interaction of austenite/martensite phase boundaries with Ti_3Ni_4 precipitates which caused the mechanical stabilization of the martensitic

phase and accumulation of residual strain (Gall and Maier 2002). On the other hand, large incoherent Ti_3Ni_4 precipitates (500 nm) resulted in the formation of stabilized martensite (Fig. 2.14a) and significant dislocation activity (Fig. 2.14b).

Furthermore, the study of Gall and Maier (2002) demonstrated a strong dependence of cyclic degradation resistance with respect to different crystallographic orientations. It was shown that a low resolved shear stress on the active slip systems of NiTi alloys resulted in improved cyclic degradation resistance, i.e. lower interfacial friction and stress hysteresis. It was concluded that irrespective of the heat treatment (precipitate size) and crystallographic orientation NiTi single crystals with low stress hysteresis showed good cyclic degradation resistance (Gall and Maier 2002).

3 Co based shape memory alloys

The phase constitution of Co-Ni-Al alloys plays a key role for the understanding and development of high temperature shape memory materials. It has been shown that the austenitic β phase ((Co,Ni)Al: B2) is attractive as high temperature structural material due to the high melting point and excellent oxidation resistance, while the γ' phase ((Ni,Co)₃Al: L1₂) enhances high temperature strength (Kainuma et al. 1996). Co-Ni-Al β phase alloys undergo a thermoelastic transformation from B2 austenite to L1₀ martensite within a limited composition range and exhibit the shape memory effect (Ishida et al. 1991). However, the low ductility of the β phase restricts practical applications. Significant improvement of hot-workability and room temperature ductility has been demonstrated in Co-Ni-Al β -based alloy systems due to the introduction of γ phase (Ni,Co,Al: A1) within the β matrix by proper choice of composition and heat treatment (Ishida et al. 1991). Moreover, investigations on phase equilibria among γ (A1), γ' (L1₂) and β (B2) phases through different heat treatments in the Ni-(0-70 at %) Co-(20-30 at %) Al system have been shown by (Kainuma et al. (1996). The authors demonstrated that the $\beta + \gamma$ phase region widens with decreasing temperature as illustrated in Fig. 3.1. Simultaneously, the γ' phase field stabilizes with decreasing temperature as well. Hence, Co-Ni-Al alloys show a wide range of transformation temperatures from -100 °C to +200 °C due to the change in composition of β matrix upon of heat treatment in the $\beta + \gamma$ two phase structure. However, the poor workability of high Co $\beta + \gamma$ alloys was related to the fact that CoAl β phase is much harder and more brittle than the NiAl β phase as pointed out by (Kimura et al. (1994).

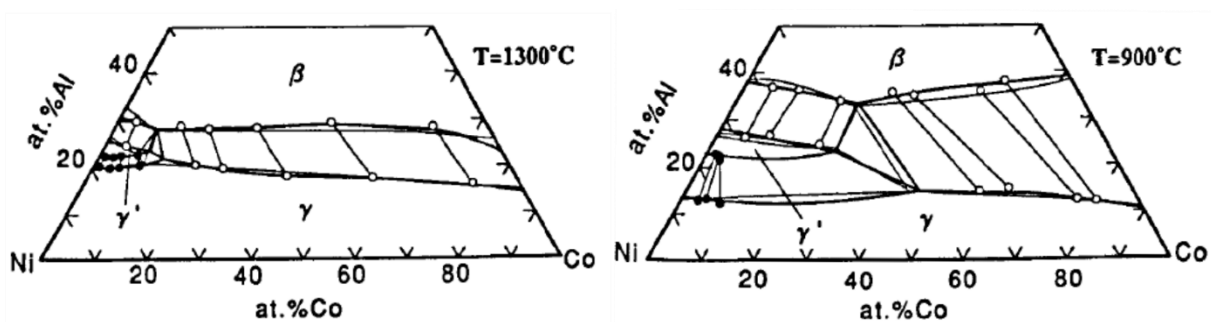


Fig. 3.1: Isothermal sections of the Co-Ni-Al ternary system at 1300°C and 900°C (modified after Kainuma et al. 1996).

Good mechanical properties of the $\beta+\gamma+\gamma'$ multi-phase alloys were reported in the Co-Ni-Al system by microstructural control through thermo-mechanical treatment (Kainuma et al. 1996). In a series of 25 at % Al specimens the authors showed that polycrystalline $\text{Ni}_{35}\text{Co}_{40}\text{Al}_{25}$ exhibits a maximum tensile strength of 1000 MPa and 8 % elongation. Furthermore, Co-Ni-Al alloys are promising HTSMAs due to a large shape memory strain and perfect superelasticity at temperatures as high as 250 °C (Karaca et al. 2003; Dadda et al. 2009).

4 Co-Ni-Ga shape memory alloys

Recently, extensive work on phase equilibria and phase transformations was conducted on Co-Ni-Ga alloys due to their similar characteristics as the Co-Ni-Al alloys (Oikawa et al. 2001, 2006; Liu et al. 2006). The $\beta + \gamma$ two phase region in Co-Ni-Ga alloys extends widely from the Co-Ga side to near the Ni-Ga side as shown in Fig. 4.1. This is very similar to Co-Ni-Al ternary system. Co-Ni-Ga alloys turned out to be promising for applications at elevated temperatures, due to improved formability by controlled ductile γ -phase formation (fcc disordered structure) within the β -phase matrix and the wide range of transformation temperatures (Oikawa et al. 2001, 2006). Moreover, it has been shown in Co-(10-50 at %) Ni-(30-32 at %) Ga alloys that martensite start (M_s) values in 30 at % Ga are considerably higher than in the 30 at% Al, at any given Co content (Oikawa et al. 2001). Dadda *et al.* (2007) examined transformation temperatures of single crystalline $\text{Co}_{49}\text{Ni}_{21}\text{Ga}_{30}$ alloys in the as-grown condition (without subsequent heat treatment) using differential scanning calorimetry (DSC), i.e. the austenite start (A_s), austenite finish (A_f), martensite start (M_s) and martensite finish (M_f) temperatures are -2.4, 1.3, -18, -22.4 °C, respectively. However, heat treatment of Co-Ni-Ga alloys significantly changes transformation temperatures and mechanical properties (Monroe et al. 2010; Chumlyakov et al. 2012; Kireeva et al. 2013, 2014). Heat treatment above 1100 °C and subsequent quenching to room temperature leads to the formation of β single phase alloys. Between 1100 °C and 600 °C the $\beta + \gamma$ two phase region exists in a wide range of compositions (Oikawa et al. 2006). The precipitation of the Ga poor γ phase within the $\beta + \gamma$ two phase region is correlated with the enrichment of Ga in the β phase matrix and a decrease of transformation temperatures which has been reported by (Oikawa et al. (2006) for Co-Ni-Ga alloys with compositions in the range of Co-(18-50 at %) Ni-(30-32 at %) Ga. Although ductility can be improved by γ phase formation which is crucially needed for polycrystalline specimens, shape memory reversibility is reduced because the γ phase does not transform (Hamilton et al. 2005). Heat treatment between 800 °C and 300 °C leads to γ' phase formation within the β phase matrix. γ' phase precipitates (ordered fcc with $L1_2$ structure) keep a coherent orientation relationship to the β phase and enhance the hardness of the Co-Ni-Ga alloy system as pointed out by (Liu et al. 2006; Kireeva et al. 2013). Furthermore, it has been shown that γ' precipitates have a strong influence on the martensitic transformation decreasing the transformation temperatures and enhancing the stress hysteresis (Chumlyakov et al. 2012; Kireeva et al. 2013, 2014).

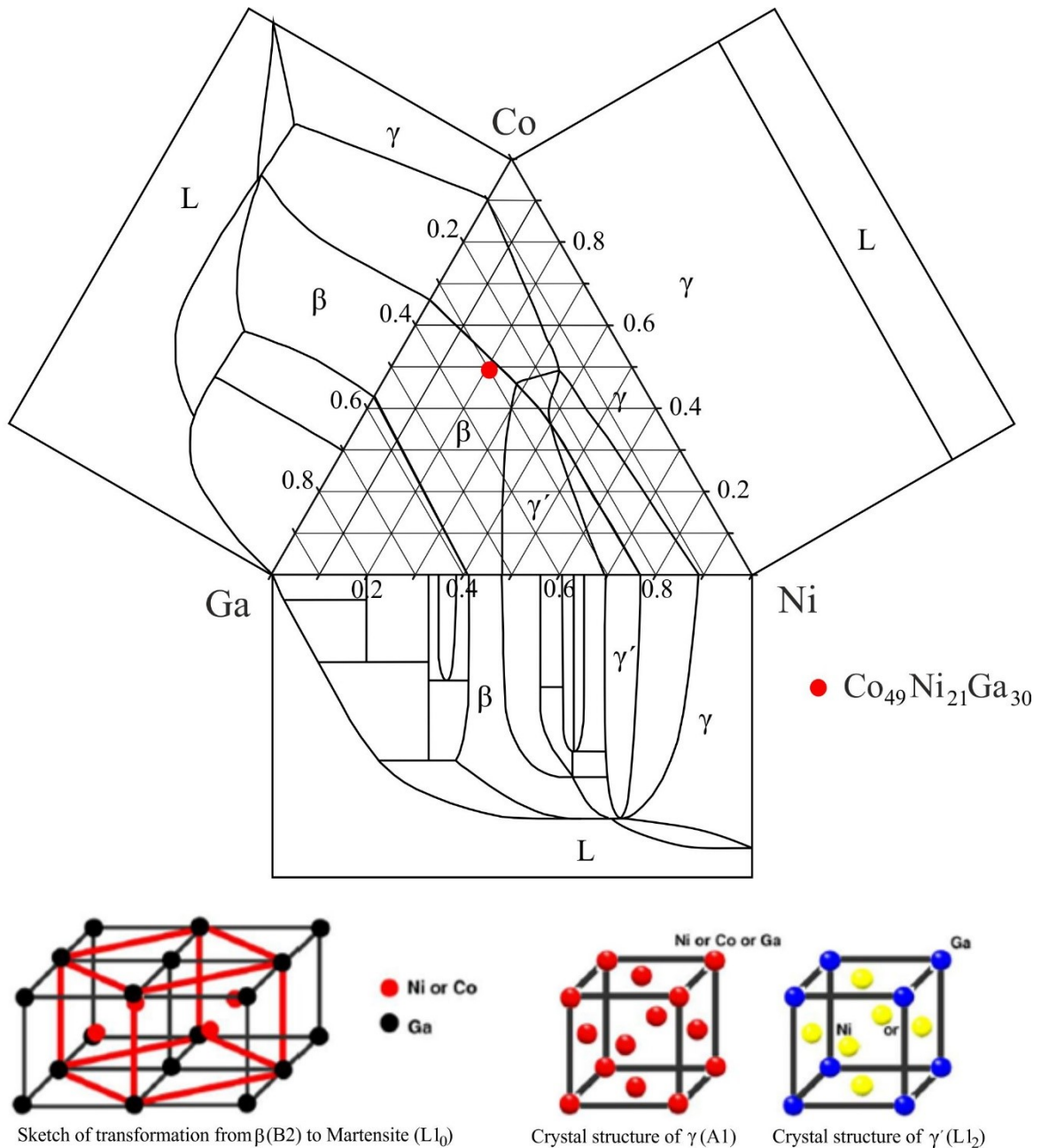


Fig. 4.1: Co-Ni-Ga ternary diagram and the corresponding crystal structures of $\beta(B2: Pm-3m)$, $\beta'(L1_0: P4/mmm)$, $\gamma(A1: Fm-3m)$ and $\gamma'(L1_2: Pm-3m)$ phases (modified after Liu et al. 2006).

Co-Ni-Ga alloys undergo a thermoelastic transformation from B2 austenite to $L1_0$ martensite as already reported in Co-Ni-Al alloys. The number of domain variants formed depends on the change in symmetry from austenite to martensite. In the cubic to tetragonal phase transformation three domain variants of martensite can be obtained (Bhattacharya 2003). Consequently, twinning two symmetry related domain variants (Fig. 4.2a) is possible along six

diagonal stress-free twin planes (Fig. 4.2b) of the type $\{110\}$. In this regard, six CVPs can emerge from 6 possible twin planes.

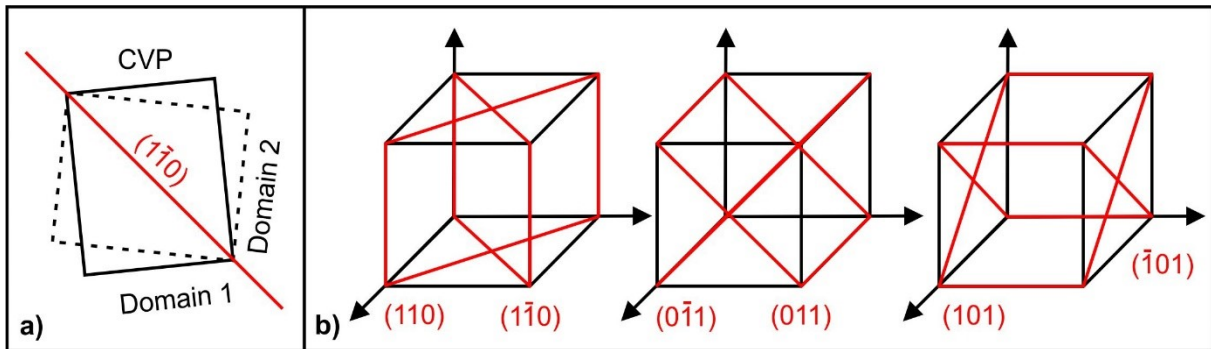


Fig. 4.2: (a) Two symmetry-related domain variants form a correspondent variant pair (CVP). The twin interface (highlighted for $(1\bar{1}0)$) between Domain 1 and Domain 2 is marked by the red diagonal. (b) Six possible diagonal twin planes of the type $\{110\}$ in the cubic austenite lattice.

A large superelastic response with a fully reversible stress-induced martensite transformation up to 500 °C have been shown in single crystalline material qualifying Co-Ni-Ga for high-temperature damping (Dadda et al. 2006; Krooß et al. 2015). Further work on Co-Ni-Ga alloys uncovered dislocation activities and martensite stabilization above 120 °C that strongly affect the evolution of microstructure and superelastic transformation characteristics (Dadda et al. 2010). The authors demonstrated that dislocation activities trigger the formation of stress-induced martensite microstructures with multiple orientations of habit planes (multi-variant martensite) under compressional load (Fig. 4.3). Furthermore, dislocations cause the mechanical stabilization of stress-induced martensite due to the immobilization (pinning) of the moving austenite-martensite phase boundaries as already pointed out by (Kustov et al. 2004). As a consequence, the enhanced stress hysteresis observed under compressional load above 120°C is correlated with increased frictional energy between moving habit planes with multiple orientations (Dadda et al. 2010). Below 100 °C, the authors demonstrated the formation of martensite plates between few well-defined parallel habit planes (Fig. 4.4). This fact was attributed to low dislocation activities imparting stable superelastic stress-strain behavior.

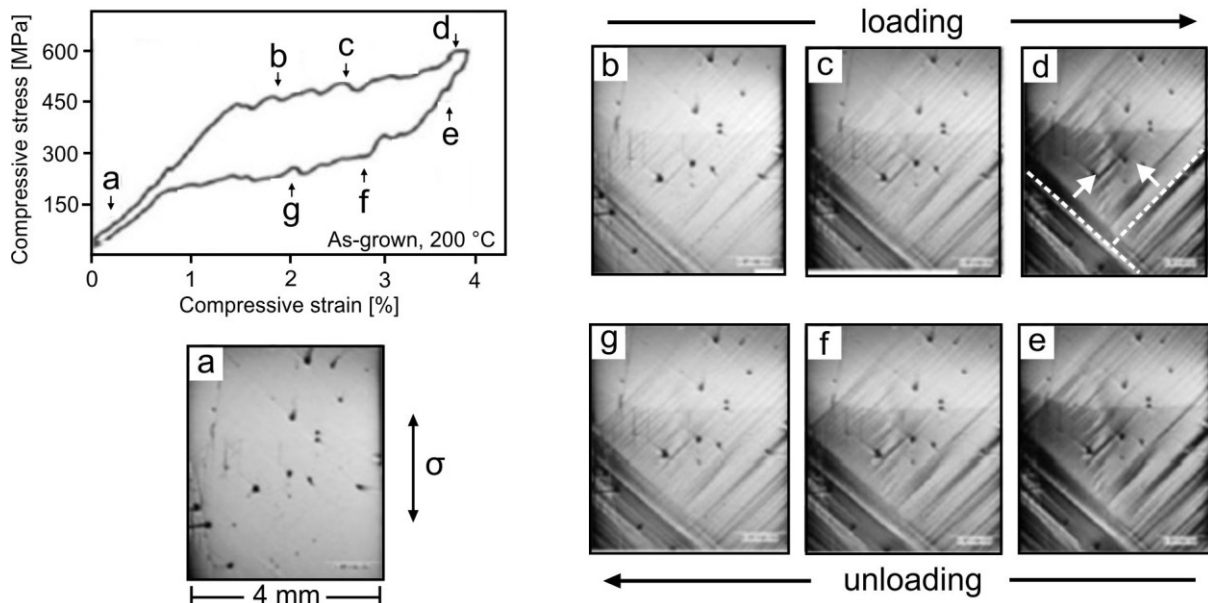


Fig. 4.3: In-situ optical micrographs of [001]-oriented as-grown $Co_{49}Ni_{21}Ga_{30}$ single crystals under compression. Multi-variant stress-induced martensite microstructures comprising multiple orientations of parallel habit planes at 200 °C (modified after Dadda et al. 2010).

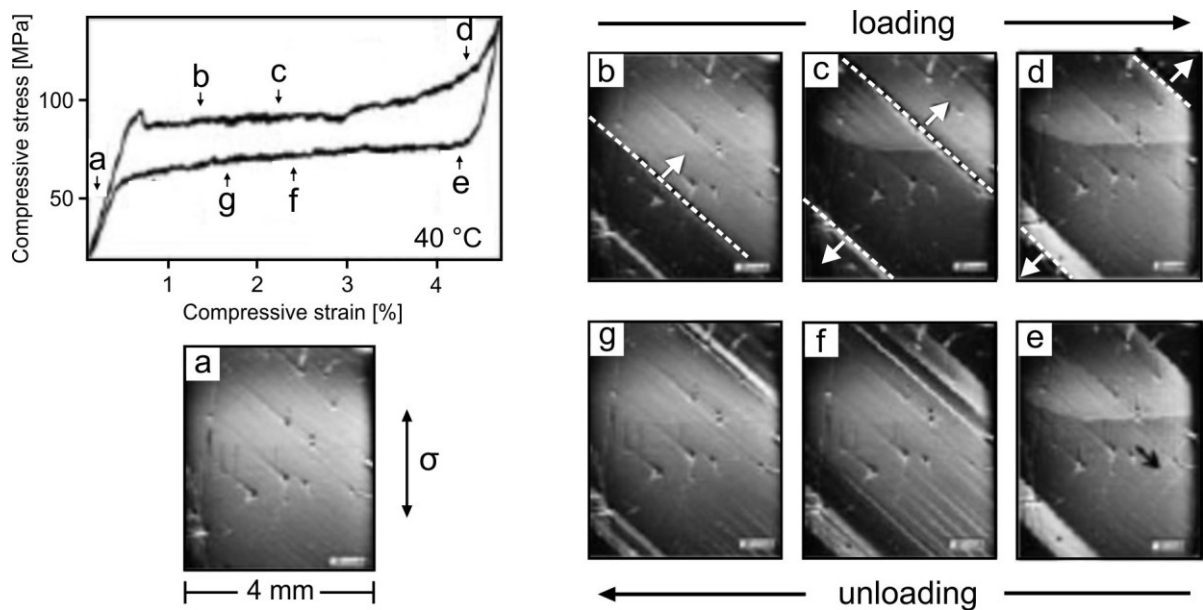


Fig. 4.4: In-situ optical micrographs of [001]-oriented as-grown $Co_{49}Ni_{21}Ga_{30}$ single crystals under compression. Formation of martensite plates between few well-defined parallel habit planes at 40 °C (modified after Dadda et al. 2010).

Related work investigated the mechanisms of cyclic deformation in single crystalline Co-Ni-Ga under compression and tension (Krooß et al. 2015). This study revealed excellent long-term

cyclic stability without any kind of functional degradation up to 100 °C under compression (Fig. 4.5) and tension (Fig. 4.6).

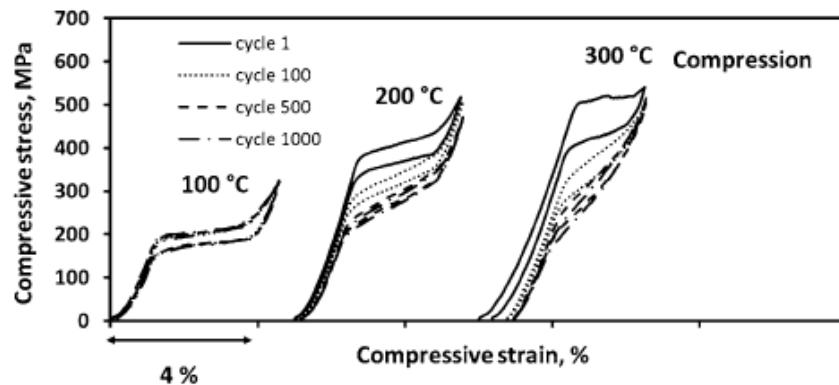


Fig. 4.5: Cyclic SE response of [001]-oriented as-grown $\text{Co}_{49}\text{Ni}_{21}\text{Ga}_{30}$ single crystals under compression tested at different temperatures (Krooß et al. 2015, reproduced with permission from Springer Nature).

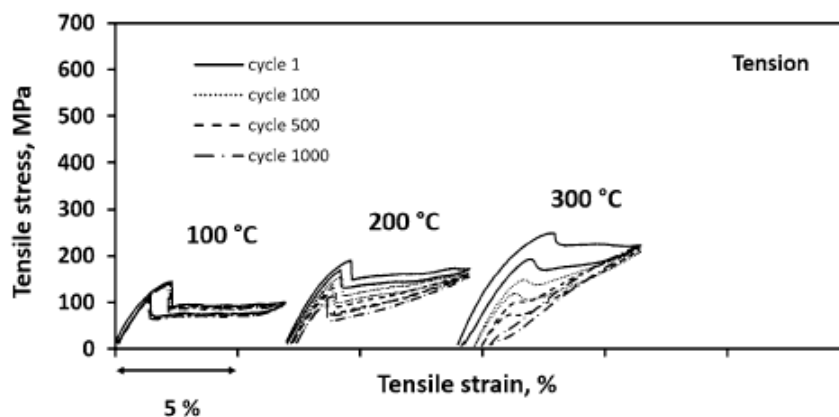


Fig. 4.6: Cyclic SE response of [001]-oriented as-grown $\text{Co}_{49}\text{Ni}_{21}\text{Ga}_{30}$ single crystals under tension tested at different temperatures (Krooß et al. 2015, reproduced with permission from Springer Nature).

However, under compressional load above 100 °C (Fig. 4.5) cyclic degradation occurred which is attributed to the formation of martensitic microstructures with multiple orientations of habit planes (Dadda et al. 2010). This work concluded that slip deformation assists the introduction of dislocations and stabilization of the martensitic phase (residual martensite) which causes irrecoverable strain during cyclic loading. Furthermore, the stabilization of the martensitic

phase is correlated with a decrease in critical transformation stress to induce stress-induced martensite in subsequent cycles which has been reported in various SMAs (Picornell et al. 2001, 2009; Gall and Maier 2002; Chernenko et al. 2004; Kustov et al. 2004; Kadletz et al. 2015; Niendorf et al. 2015).

Co-Ni-Ga single crystals in [001] orientation show significant tension-compression asymmetry with maximum theoretical transformation strains of 4.3 % and 8.6 % under compression and tension, respectively (Dadda et al. 2010; Monroe et al. 2010; Niendorf et al. 2013; Krooß et al. 2015). The large transformation strain obtained under tension has been attributed to detwinning of stress-induced martensite (Monroe et al. 2010). However, the amount of dissipated energy (stress hysteresis width) at elevated temperatures is considerably smaller under tension as compared to compression (Krooß et al. 2015). This fact has been inferred by the suppression of stress-induced martensite microstructures with multiple orientations of habit planes. Specifically, the accumulation of irrecoverable strain and stabilization of the martensitic phase as a result of dislocation activities at the austenite/martensite phase boundary is significantly reduced under tensile load (Krooß et al. 2015). The deterioration of the superelastic transformation characteristics in Co-Ni-Ga SMAs examined above 120 °C is attributed to two important degradation mechanisms, such as martensite stabilization and dislocation activities. However, this work revealed that both mechanisms are less pronounced under tension as compared to compression.

Beside the segregation of ductile γ phase, in Co-Ni-Ga SMAs nanometric γ' precipitates (ordered fcc with $L1_2$ structure) can be introduced in the austenitic phase at intermediate-temperature aging treatments above 300 °C (Chumlyakov et al. 2012; Kireeva et al. 2013, 2014). Aging treatments for 1 h at 350 °C (Fig. 4.7a) trigger the formation of spheroidal and coherent γ' precipitate with 5 nm diameter (Chumlyakov et al. 2012; Kireeva et al. 2013), while after a longer aging treatment for 3 h at 350 °C (Fig. 4.7b) the γ' precipitates adopt elongated shapes with a thickness around 5-8 nm and a length of about 10-25 nm (Chumlyakov et al. 2012; Kireeva et al. 2013, 2014). As pointed out by Dogan et al. (2011), Chumlyakov et al. (2012) and Kireeva et al. (2013, 2014), γ' precipitates are effective for increasing the hardness of the austenite matrix and strongly affect the functional properties with respect to SME and SE in Co-Ni-Ga SMAs. Precipitation-hardening is a common approach in SMA systems in particular, to attain high-temperature SE, eventually hampering plastic deformation and dislocation slip (Miyazaki et al. 1986; Gall and Maier 2002; Ma et al. 2010).

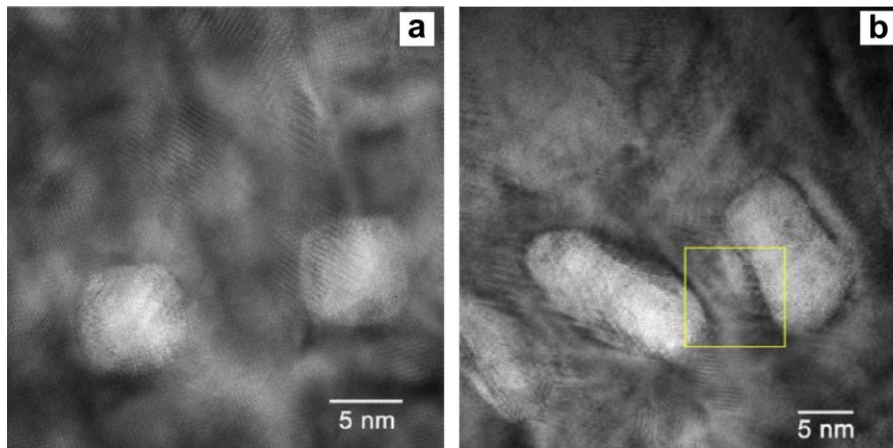


Fig. 4.7: HRTEM images of spheroidal and elongated γ' precipitates formed after aging at 350°C for 1 h (a) and 3 h (b), respectively (Kireeva et al. 2013, reproduced with permission from Elsevier).

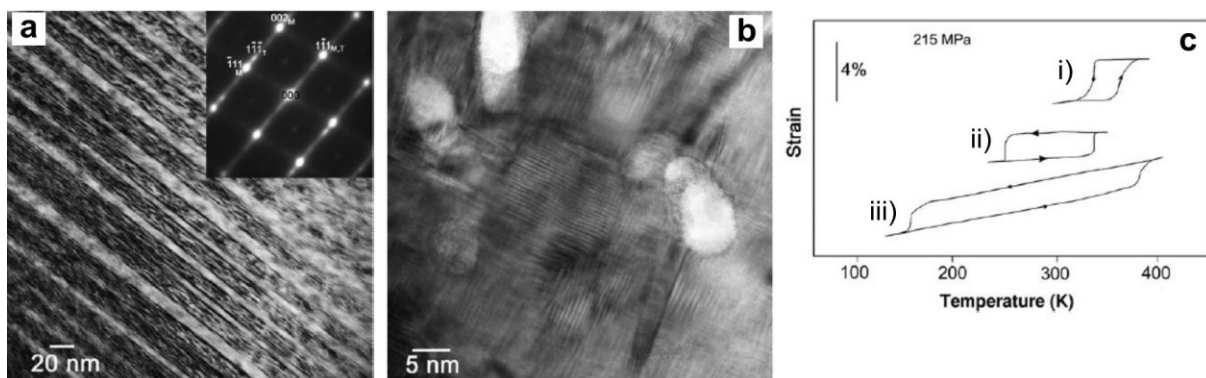


Fig. 4.8: TEM- (a) and HRTEM micrographs (b) of thermally induced martensite obtained after aging at 350 °C for 1 h (a) and 3 h (b). (c) Strain-temperature curves recorded at 215 MPa for three thermal treatments: 1 h at 350 °C (ii), 3 h at 350 °C (iii) and the solution-annealed (i) reference state being free of any secondary phases (Kireeva et al. 2013, reproduced with permission from Elsevier).

However, the martensite microstructure is substantially modified by the size and morphology of the γ' precipitates (Kireeva et al. 2014). For instance, a notable twin-thickness reduction in thermally induced martensite has been observed with increasing particle size and was related to both pronounced elastic energy accumulation and difficulties in accommodating the transformation strain around the irregular stress fields of the non-transforming γ' precipitates (Kireeva et al. 2013). As shown in Fig. 4.8b the reduction of martensite twin thickness is more pronounced for larger γ' precipitates compared to small (spheroidal) γ' precipitates (Fig. 4.8a).

Above a critical size the γ' precipitates become impenetrable obstacles for the moving austenite-martensite phase front. As a consequence, martensite showed internal micromodulations (nano-twinning) between large elongated γ' precipitates (Fig. 4.8b). Additionally, γ' precipitates strongly affect the functional properties as shown in Fig. 4.8c. In this case, γ' precipitates cause an enhancement of the temperature hysteresis (ΔT), the reduction of the transformation temperatures (M_s , M_f , A_s , A_f) and -strains (ε_{tr}) in relation to the solution annealed reference state (Kireeva et al. 2013, 2014). However, a thorough understanding of the stress-induced martensitic transformation under the influence of γ' precipitates in Co-Ni-Ga SMAs has not been addressed so far. In this regard, a detailed understanding of the role of the morphology and variant selection of stress-induced martensite will be established in this work. This, in turn, will contribute to a comprehensive knowledge about the complex interrelationships between microstructure, MT and functional properties.

5 Overview of publications and author contributions

This thesis is the detailed report of the author's Ph.D research work on the stress-induced martensitic transformation in Co-Ni-Ga high-temperature shape memory alloys. Three chapters of the thesis are based on scientific research manuscripts which were published as a journal article (chapter 7.1, 7.2 and 7.3). The author of this thesis is the principal author and co-author of chapter 7.1, 7.3. and chapter 7.2, respectively.

Chapter 7.1 was published as:

A. Reul, C. Lauhoff, P. Krooß, M.J. Gutmann, P.M. Kadletz, Y.I. Chumlyakov, T. Niendorf, W.W. Schmahl, In Situ Neutron Diffraction Analyzing Stress-Induced Phase Transformation and Martensite Elasticity in [001]-Oriented $\text{Co}_{49}\text{Ni}_{21}\text{Ga}_{30}$ Shape Memory Alloy Single Crystals, Shape Mem. Superelasticity. 4 (2018) 61–69.

AR, CL, PK and PMK conducted the experiments under the supervision of the beamline scientist MJG (ISIS). AR analyzed and interpreted the neutron diffraction data and drafted the manuscript. YIC prepared the Co-Ni-Ga single crystals. All authors contributed to discussions and the final manuscript.

Chapter 7.2 was published as:

C. Lauhoff, A. Reul, D. Langenkämper, P. Krooß, C. Somsen, M.J. Gutmann, I. Kireeva, Y.I. Chumlyakov, W.W. Schmahl, T. Niendorf, Effect of nanometric γ' particles on the stress-induced martensitic transformation in $\langle 001 \rangle$ -oriented $\text{Co}_{49}\text{Ni}_{21}\text{Ga}_{30}$ shape memory alloy single crystals, Scr. Mater. 168 (2019) 42–46

AR and CL conducted the neutron diffraction experiments under the supervision of the beamline scientist MJG (ISIS). AR analyzed, interpreted and evaluated the neutron diffraction data. DL and CS performed the transmission electron microscopy experiments and analyzed the data. CL carried out mechanical testing, optical microscopy and drafted the manuscript. YIC prepared the Co-Ni-Ga single crystals. All authors contributed to discussions and the final manuscript.

Chapter 7.3 was published as:

A. Reul, C. Lauhoff, P. Krooß, C. Somsen, D. Langenkämper, M.J. Gutmann, B. Pedersen, M. Hofmann, W.M. Gan, I. Kireeva, Y. I. Chumlyakov, G. Eggeler, T. Niendorf, W.W. Schmahl, On the impact of nanometric γ' precipitates on the tensile deformation of superelastic $\text{Co}_{49}\text{Ni}_{21}\text{Ga}_{30}$, *Acta Materialia* 230 (2022) 117835

AR and CL conducted the neutron diffraction experiments under the supervision of the beamline scientists MJG (ISIS), MH (FRM-II) and WMG (FRM-II). AR evaluated the neutron diffraction data and drafted the manuscript. DL and CS performed the transmission electron microscopy experiments and analyzed the data. CL carried out mechanical testing, optical microscopy. The Co-Ni-Ga crystals were prepared and tested for single crystallinity by YIC and BP (FRM-II), respectively. All authors contributed to discussions and the final manuscript.

6 Instrumental methods

6.1 Specimen preparation

Single crystalline specimens were provided by project partners from the Siberian Physical-Technical Institute at Tomsk State University (Russia) under the supervision of Prof. Yuri I. Chumlyakov. Large single crystals (30 mm in diameter and 100 mm length) with a nominal composition of $\text{Co}_{49}\text{Ni}_{21}\text{Ga}_{30}$ (at %) were grown using the Bridgeman technique in a helium inert gas environment. Compressive and tensile specimens were obtained by electro-discharge machining (EDM) from the bulk single crystal as shown in Fig. 6.1.

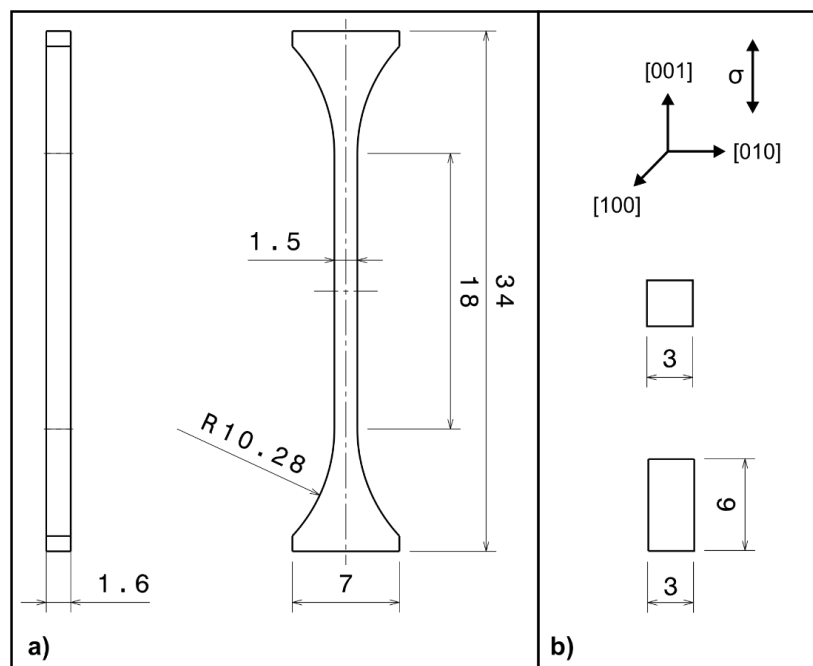


Fig. 6.1: Geometries of tensile and compressive specimens are shown in (a) and (b), respectively. Note, the compressive specimen with geometry of $4 \times 4 \times 8 \text{ mm}^3$ is not shown. The direction of stress σ is parallel to the $[001]$ crystal direction (tension and compression) as illustrated at top of (b).

For tensile tests flat biconcave specimens with a gauge length of 18 mm and a cross section of 1.5 mm x 1.5 mm were prepared (Fig. 6.1a). For compression tests specimens with geometry of $3 \times 3 \times 6 \text{ mm}^3$ and $4 \times 4 \times 8 \text{ mm}^3$ were used (Fig. 6.1b). The longer loading axis of compressive and tensile specimens were parallel to the $[001]$ crystal direction of the austenitic phase, while the normal vectors of the lateral surfaces were parallel to $[100]$ and $[010]$ as shown at top of Fig. 6.1b.

Following EDM, specimens were mechanically ground in order to remove the EDM affected surface layer. Specimens were prepared for experimental tests in as-grown, solution-annealed and aged condition. Specimens in the as-grown condition (which is the most studied state in literature (Chernenko et al. 2004, 2007; Dadda et al. 2006, 2008, 2010; Kadletz et al. 2015; Krooß et al. 2015, 2016; Reul et al. 2018) were tested without preceding heat treatment. In order to obtain a single-phase condition free of any secondary phases (Kireeva et al. 2013, 2014) all samples (except for the as-grown condition) were solution-annealed at 1200 °C for 12 h. Solution-annealing was conducted in sealed quartz glass tubes under argon atmosphere followed by breaking of the quartz tubes and air cooling to room temperature. Aging of the solution-annealed specimens to form nanometric γ' precipitates (~ 5 nm size) with spheroidal shape were performed at 350 °C for 1 h under ambient atmosphere. The aging parameter was selected in accordance to (Chumlyakov et al. 2012; Kireeva et al. 2013).

6.2 *In situ* optical microscopy (OM)

Quasi-static uniaxial compression and tension experiments were performed at 100 °C at a nominal strain rate of $1.0 \times 10^{-3} \text{ s}^{-1}$ on a servo-hydraulic load frame in displacement control. Superelastic single cycle stress-strain curves were performed up to a maximum strain of 11 % upon loading and a given minimum load of -50 N for unloading. The selected test temperature ensured a fully austenitic state prior to superelastic testing. Heating of the specimen to test temperature was achieved by controlled convection furnaces. Temperatures were measured with a thermocouple attached to one of the lateral sample surfaces. For calculation of the nominal strain the grips were treated as absolutely rigid. *In situ* OM analysis of the transforming specimen was performed on various stages of the superelastic stress-strain hysteresis. In addition to the mechanical grinding using silicon carbide down to 5 μm grit size, the side surfaces being investigated were mechanically polished using a colloidal SiO_2 polishing suspension with 0.05 μm particle size. Grinding and polishing were performed in the austenitic condition. Surface images were collected on a representative surface area of about $3.5 \times 2.5 \text{ mm}^2$ by using a Keyence digital microscope of the type VHX-600 equipped with a tele-zoom objective of the type VH-Z100. Furthermore, confocal laser scanning microscopy (CLSM) was employed using an Olympus LEXT OLS3100 equipped with a 408 nm violet laser. The CLSM has a maximum axial and lateral resolution of 10 nm and 120 nm, respectively.

6.3 In situ neutron diffraction

In situ characterization of stress-induced phase transformations is offered with neutron diffraction. In general neutron diffraction allows extracting information on the phase state and structural changes on an atomistic level from large bulk specimens, due to the high penetration depth of neutrons into matter (e.g. 20 mm into steel or 100 mm into aluminum) (Hofmann et al. 2006; Hoelzel et al. 2013). In this case, material characterization was conducted at two neutron diffractometers SXD and STRESS-SPEC.

6.3.1 In situ neutron diffraction (SXD)

In situ neutron diffraction was carried out using the single-crystal diffractometer SXD at the ISIS neutron source, Rutherford Appleton Laboratory, Oxfordshire. SXD uses the neutron time-of-flight technique to acquire diffraction data of a single crystalline specimen at a fixed orientation 2θ as illustrated in Fig. 6.2.

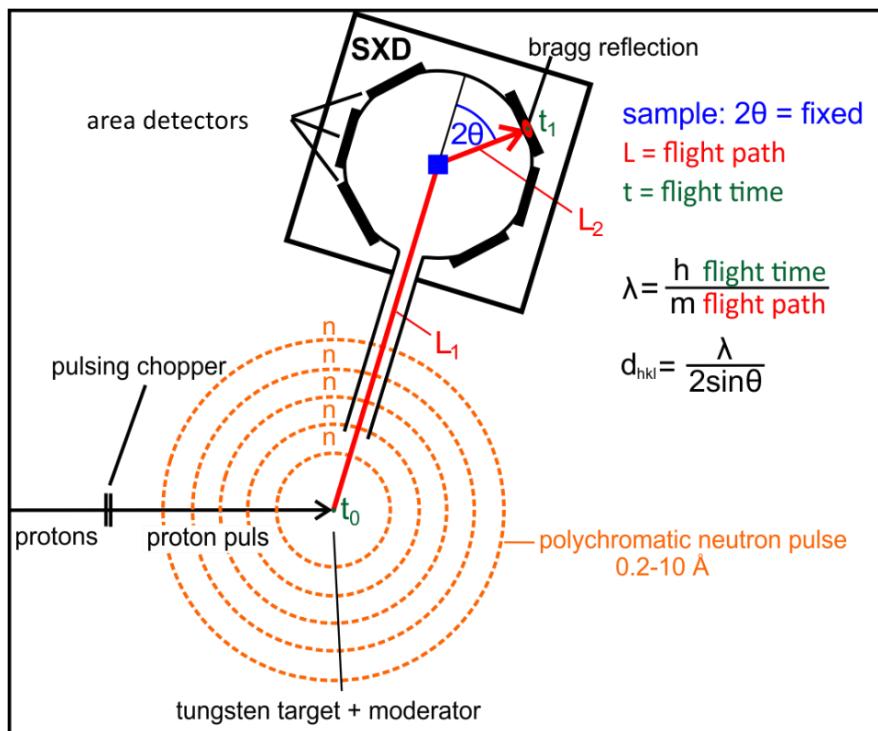


Fig. 6.2: Schematic setup of the single crystal diffractometer (SXD). The polychromatic neutron beam is scattered on the single crystal specimen surrounded by eleven 2D detectors. Time-of-flight is the time neutrons take from the spallation target to the detector. The crystal d -space is proportional to neutron time-of-flight for a given scattering angle 2θ .

A polychromatic neutron beam, covering wavelengths in a range of 0.2-10 Å, is scattered on the single-crystal specimen. Scattered neutrons are collected as a function of time-of-flight on eleven large area two-dimensional LiF/ZnS position-sensitive detectors (PSDs) arranged around the sample position. Time-of-flight represents the time the neutron takes from the spallation target to the detector, via the sample. Each detector has an active area of 192 x 192 mm and consists of 64 x 64 pixels, i.e. each pixel is 3 x 3 mm. The orders of a given reflection (e.g. 002, 004, 006) are collected on the same detector pixel and each order is collected at different time-of-flight. For a given scattering angle 2θ , the time-of-flight spectrum obtained from SXD data is proportional to the crystal spacing, d . This setup allows covering diffraction data within a wide range of reciprocal space increasing the speed of data collection compared to monochromatic single-crystal neutron diffractometers. For further details on the setup of SXD, the reader is referred to Keen et al. (2006).

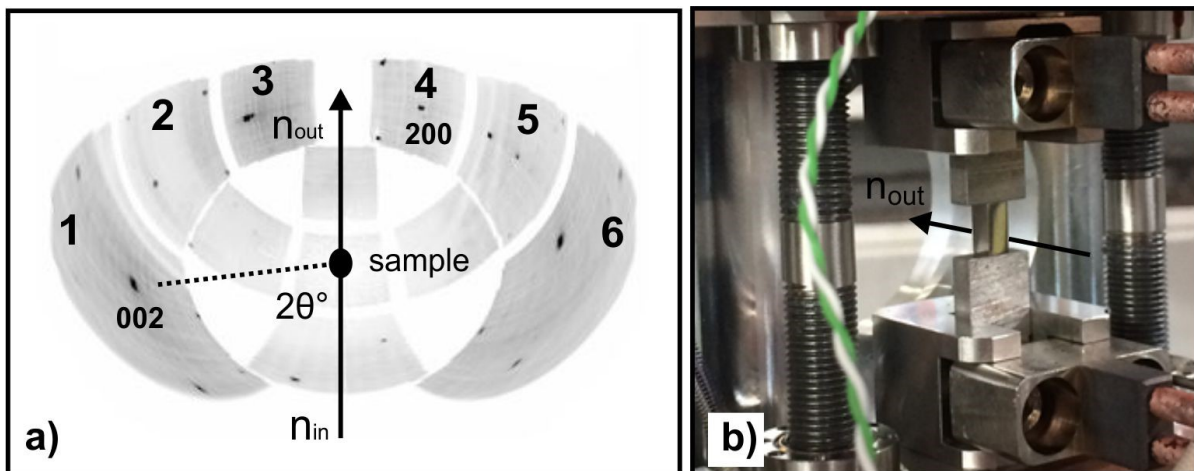


Fig. 6.3: (a) Diffraction data was collected on six equatorial detectors. Five detectors beneath the sample position were not accessible due to shading by the miniature load frame. Shaded regions on detectors are visible by the white contrast. (b) Compression sample mounted between the grips of the miniature load frame.

Uniaxial single cycle compression tests were performed on as-grown, solution-annealed and aged specimens using a newly installed miniature load frame (Kammrath und Weiss, Germany) capable of ± 10 kN in displacement control at a nominal displacement rate of 5×10^{-3} mms^{-1} . Displacement at each loading stage was derived from stress values from the *in situ* OM experiment. Strains were calculated from displacement data. Reflections from the 002 and 200 lattice planes of austenite were centered on high-angle detector 1 and low-angle detector 4 of

SXD by rotation of the sample around its vertical axis to a fixed position 2Θ (Fig. 6.2 and Fig. 6.3a). Diffraction data were recorded on six equatorial detectors during each loading stage in the austenitic and martensitic state for 20 and up to 130 min, respectively. Diffraction data were indexed and integrated using the software package SXD2001 (Keen et al. 2006). Four detectors at an angle of 45° to the equatorial plane and one directly beneath the sample position were not accessible in this experiment due to shading by the miniature load frame (Fig. 6.3b). Obviously, the shading of the detector array below the sample reduces the number of accessible diffraction peaks. However, it has no detrimental effect on the quality of data in this experiment, since Laue time-of-flight technique enables the complete determination of the lattice and phase state of the alloy.

6.3.2 In situ neutron diffraction (STRESS-SPEC)

In situ neutron diffraction was carried out using the STRESS-SPEC diffractometer at FRMII, Munich. The selection of three different monochromators (Ge (511), Si (400) and pyrolytic graphite PG (002)) and the continuous take-of angle variation between 30° and 130° allows covering a wavelength range of 1 - 2.4 Å. The instrument operates with a monochromatic neutron beam and offers a scattering angle range between 30° and 120° in 2Θ . Diffraction data were collected on a two-dimensional position-sensitive ^3He detector. This detector has an active area of 225 x 225 mm and consists of 256 x 256 pixels. A double column load frame designed for maximum load of ± 50 kN was used as illustrated in Fig. 6.4. In this setup the rotation frame allows a rotation of the load axis around the χ -tilting axis in a range between 0° and 90° . The orientation of the load axis with respect to the monochromatic incident beam was $\chi = 0^\circ$ (load axis vertical to the scattering plane) and $\chi = 90^\circ$ (load axis in the scattering plane, Fig. 6.4). Sample orientation with respect to the incident beam was adjusted by a rotation of the main sample table around the ω -axis.

Uniaxial single cycle tension tests were performed on as-grown Co-Ni-Ga specimen under the same conditions as in the case of the *in situ* OM experiments. Displacement at each loading stage was derived from stress values from the *in situ* OM experiment. At each loading stage, rocking scan measurements were performed in 0.1° steps at a fixed ω -orientation (orientation of the main sample table with respect to the incident beam) around $\omega \pm 1.5^\circ$ with 10 s data collection for each step. The software package Stress Texture Calculator (SteCa) was used for data extraction (Randau et al. 2011). For further details the on the setup of STRESS-SPEC the reader is referred to Hofmann et al. (2006) and Hoelzel et al. (2013).

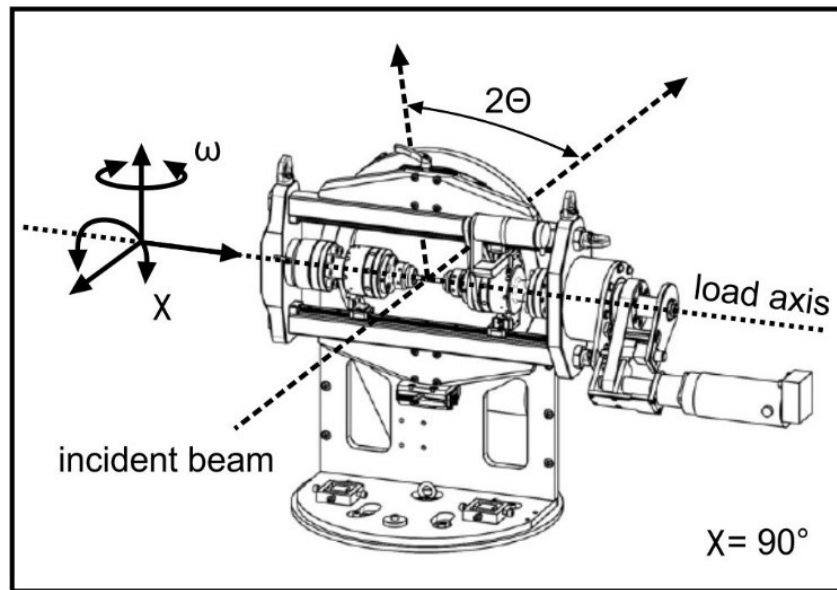


Fig. 6.4: A schematic view of the rotatable tensile rig in the horizontal setup. The orientation between the incident beam and the load axis is given by the angles ω and χ (modified after Hoelzel et al. 2013).

6.4 Transmission electron microscopy

Transmission electron microscopy was employed in cooperation with project partners from the chair for materials science and engineering at Ruhr University Bochum (Germany) under supervision of Prof. Dr.-Ing. Gunther Eggeler. A transmission electron microscope (TEM) of the type Tecnai F20 of the company FEI operated at a nominal voltage of 200 keV. For microstructural analysis selected area electron diffraction (SAED) and high-resolution transmission electron microscopy HRTEM was conducted. Small discs were cut perpendicular to the [001] loading direction from the austenitic single crystalline specimen. These discs were mechanically ground down to 0.15 μm and subsequently twin-jet polished using a perchloric acid solution containing 60 ml perchloric acid, 340 ml butanol and 600 ml methanol.

7 Experiments

7.1 In situ Neutron Diffraction Analyzing Stress-Induced Phase Transformation in [001]-oriented Co₄₉Ni₂₁Ga₃₀ Shape Memory Alloy Single Crystals

7.1.1 Aim of this study

All studies available in literature so far focus on the thermo-mechanical behavior and functional stability of Co-Ni-Ga only up to maximum theoretical transformation strains. Potential extension of the superelastic strain capability by exploration of the elastic martensite deformation has not been addressed so far. Thus, the focus of this study is the characterization of prevalent deformation mechanisms upon elastic deformation of SIM in a [001]-oriented Co₄₉Ni₂₁Ga₃₀ single crystal under compression at high stress levels up to about 1000 MPa. Besides dislocation activity or detwinning, additional twinning modes could be expected at high prevailing stresses to accommodate the deformation. In this regard, in situ neutron diffraction is an appropriate method for the evaluation of twinning under applied stress (Molnár et al. 2008) and phase quantification providing structural information from bulk specimens (Molnár et al. 2008; Stebner et al. 2014; Kadletz et al. 2015; Krooß et al. 2016) to assess elementary deformation mechanisms in Co-Ni-Ga bulk specimens.

7.1.2 Experimental details

In situ neutron diffraction was carried out using the single-crystal diffractometer SXD at the ISIS neutron source, Rutherford Appleton Laboratory, Oxfordshire as described in chapter 6.3. Uniaxial single cycle compression tests on the as-grown specimen with dimension of 4 x 4 x 8 mm³ were conducted at room temperature using a miniature load frame at a nominal displacement rate of 5 x 10⁻³ mms⁻¹ with a maximum load of 1030 MPa upon loading and a given minimum stress of -50 N after unloading. Strains were calculated from displacement data. For detailed information on sample preparation the reader is referred to chapter 6.1. Reflections from the 002 and 200 lattice planes of austenite were centered on high-angle detector 1 and low-angle detector 4 of SXD by rotation of the sample around its vertical axis to a fixed position of 26° (Fig. 6.3). Diffraction data were recorded on six equatorial detectors for 60 min during each loading stage, three in the austenite elastic region, four on the stress-strain plateau and eleven in the martensite elastic region. For further details on the setup of SXD, the reader is referred to Keen et al. (2006). Diffraction data were indexed and integrated using the software package SXD2001 (Keen et al. 2006).

7.1.3 Results

Fig. 7.1 presents the results of a superelastic uniaxial single cycle compression experiment at room temperature of the as-grown [001]-oriented $\text{Co}_{49}\text{Ni}_{21}\text{Ga}_{30}$ single crystal. Diffractograms were recorded at different stages during loading and unloading. For the sake of brevity, diffraction data of eight out of 18 diffractograms collected on high-angle detector 1 are displayed in Fig. 7.1a-h; two in the elastic austenite region (region I, Fig. 7.1a, h), two on the superelastic stress plateau (region II, Fig. 7.1 b, g) and four in the elastic martensite region (region III, Fig. 7.1c-f). In Region I the specimen in its initial state is entirely austenitic (Fig. 7.1a). After the initial linear elastic austenite deformation, the stress induced phase transformation from the partially ordered B2 austenite (Kadletz et al. 2015) to the partially ordered $L1_0$ martensite phase occurs gradually, which results in a constant stress plateau. In Region II near the end of the stress plateau the microstructure consists of almost 100 % martensite. Here the corresponding diffractogram (Fig. 7.1b) shows a weak austenite (A) reflection between two strong martensite reflections (V_1 and V_2) at a total strain of about 4.3 %. These two strong martensite reflections shown in Fig. 7.1b-g arise from the (200) V_1 and (002) V_2 lattice planes of two twin domain variants V_1 and V_2 , respectively. Correspondingly, at the end of the plateau, V_1 and V_2 form a simple regular twin structure. Space group and lattice parameters are Pm-3m (#221), $a=2.879(2)$ Å for as-grown austenite and P4/mmm (#123), $a=2.737(8)$ Å, $c=3.157(9)$ Å for stress-induced martensite (SIM). The inset in Fig. 7.1i sketches the formation of the two tetragonal martensite domain variants from B2 austenite under compressive load. As expected, their extensional c-axes, are perpendicular to the [001] compressive load direction and perpendicular to each other. Numerous additional observed reflections could be clearly assigned to various lattice planes of austenite in the initial stage (Fig. 7.2a-b) and martensite twin domain variants in the elastic martensite region (Fig. 7.2c-d). Beyond the end of the stress-strain plateau at 4.6 % strain, where the stress induced martensite transformation is completed, a further increase of stress is observed (Fig. 7.1j). The stress increase is due to elastic deformation of martensite (region III). The maximum strain achieved with 1030 MPa stress for the [001]-oriented Co-Ni-Ga single crystal is 10.7 % total strain, which includes phase transformation strain and elastic deformation (Fig. 7.1j), red dot highlighted “e”). Upon unloading from 1030 MPa in displacement control, a small hysteresis in measured stress for given displacement in the elastic region in the martensite phase (Fig. 7.1j) is observed.

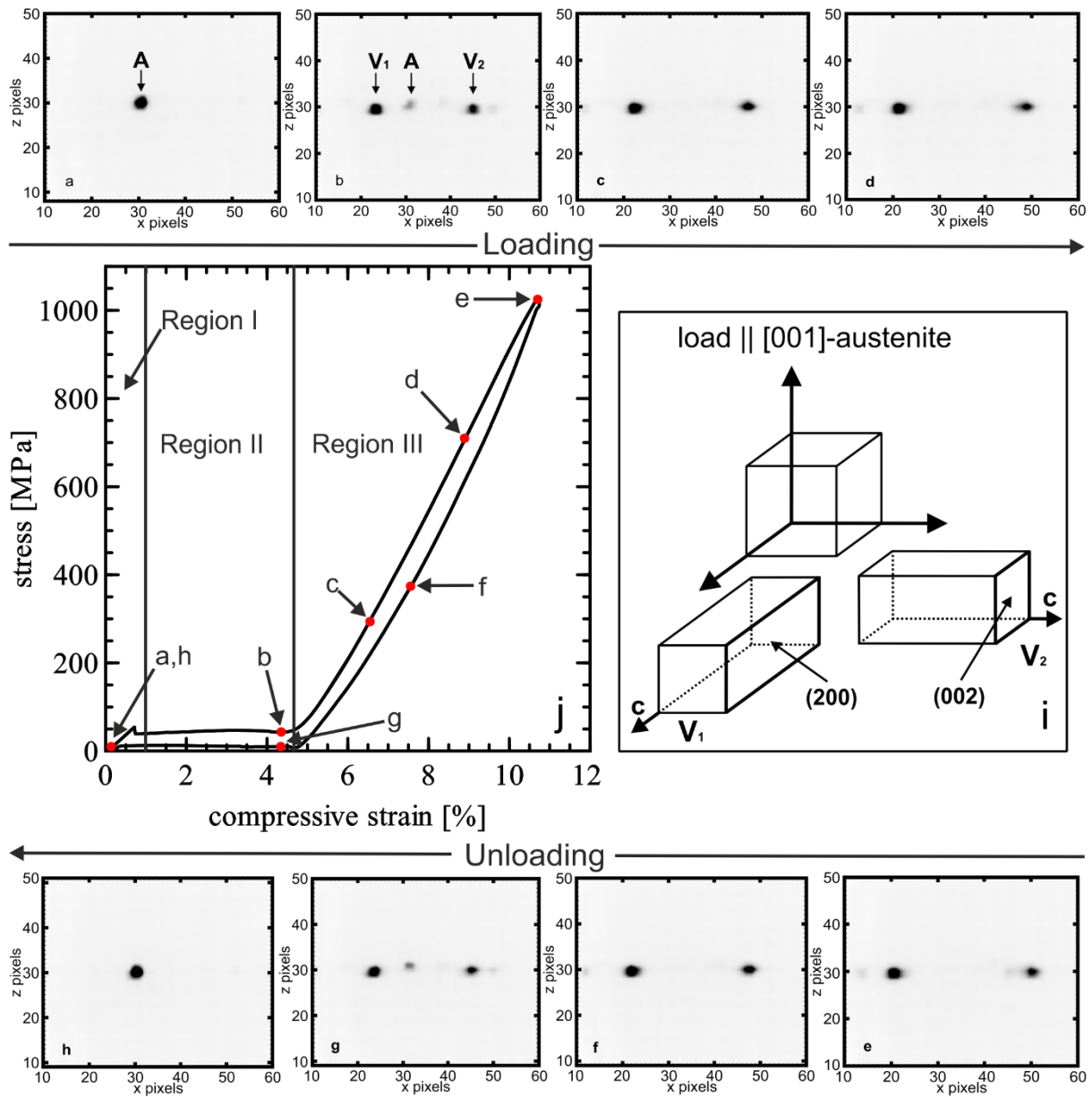


Fig. 7.1: Diffractograms of high angle detector 1 obtained from in situ neutron diffraction on $[001]$ -oriented $\text{Co}_{49}\text{Ni}_{21}\text{Ga}_{30}$ under compression. The phase state and variant selection is marked for different regions: Elastic austenite region I, stress plateau region II and elastic martensite region III. The inset (i) demonstrates the formation of two stress-induced martensite domain variants (V_1 and V_2) from bcc austenite. (See figure A1 and table A1 in the appendix for lattice parameters obtained on the marked positions in the stress-strain diagram)

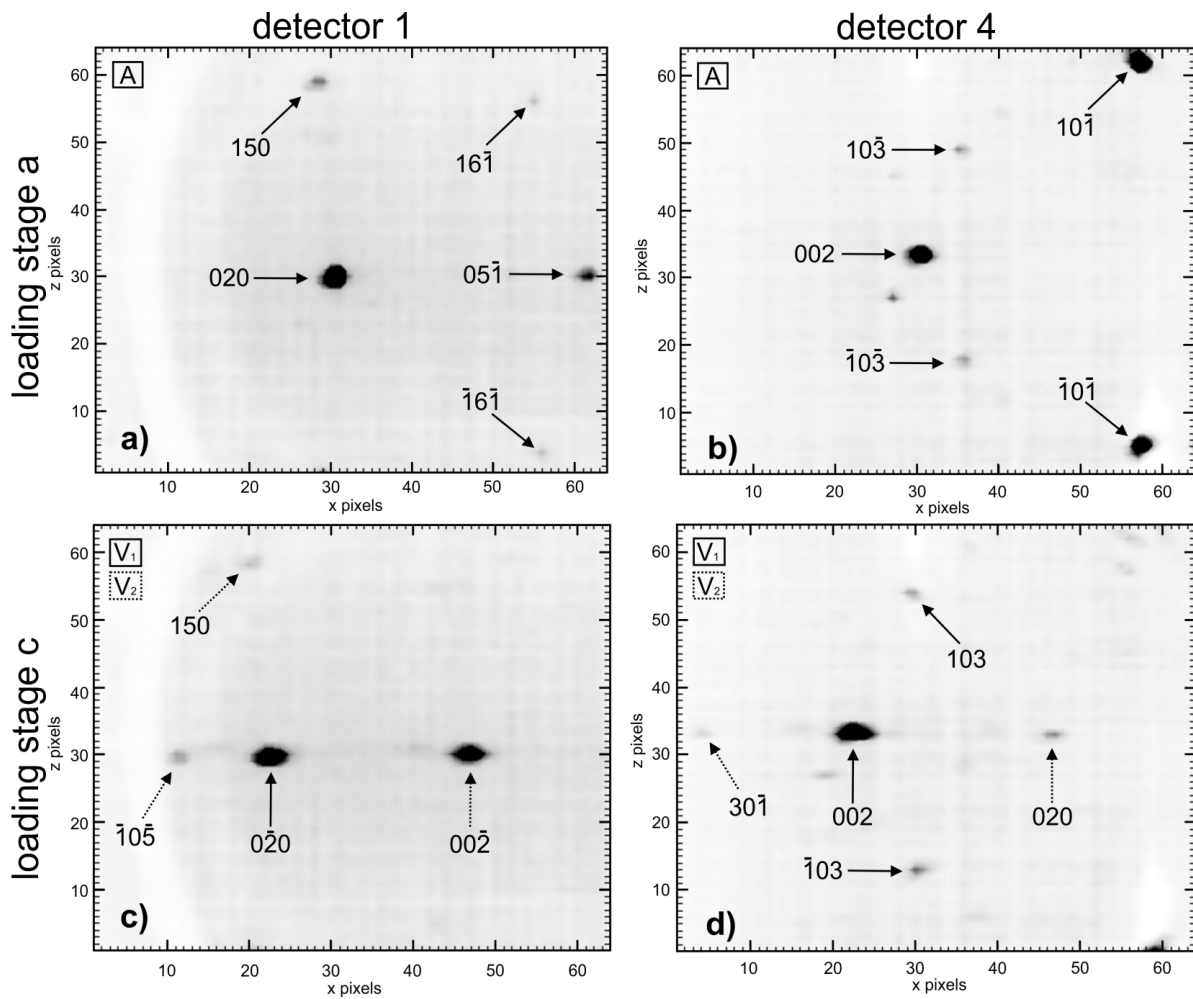


Fig. 7.2: Observed intensities on low- and high-angle detector 1 and 4; (a, b) intensities of austenite (A) without superimposed load; (c, d) intensities of two dominant stress-induced domain variants according to the schematic shown in Fig. 7.1i (V_1 and V_2) in the elastic martensite region. The formation of the third martensite domain variant is suppressed by the compressive stress along $[001]$.

Fig. 7.3 displays the measured diffraction intensities as a function of macroscopic strain and demonstrates the formation of stress induced martensite along the plateau (region II) during forward transformation and full recovery of austenite in the reverse transformation. A notable rise in intensity of martensite V_1 is observed at a very early stage of deformation of about 1 % strain, whereas the diffraction peak from martensite domain variant V_2 was observed only at the end of the stress-strain plateau. As we focused on the elementary deformation mechanisms in region III in this study, and measured only two diffractograms in the plateau region, the onset of variant formation and successive growth was not observed in detail here. In region III intensities of both martensite domain variants remain almost constant independent of the loading condition. This clearly indicates that the volume fraction of both martensite domain variants remains essentially constant upon loading and unloading in region III. An increase of the volume fraction of one of the martensite variants at the expense of the other one would have resulted in a change in their respective diffraction intensities. However, this was not observed during deformation in the elastic martensite region III up to 10.7 %.

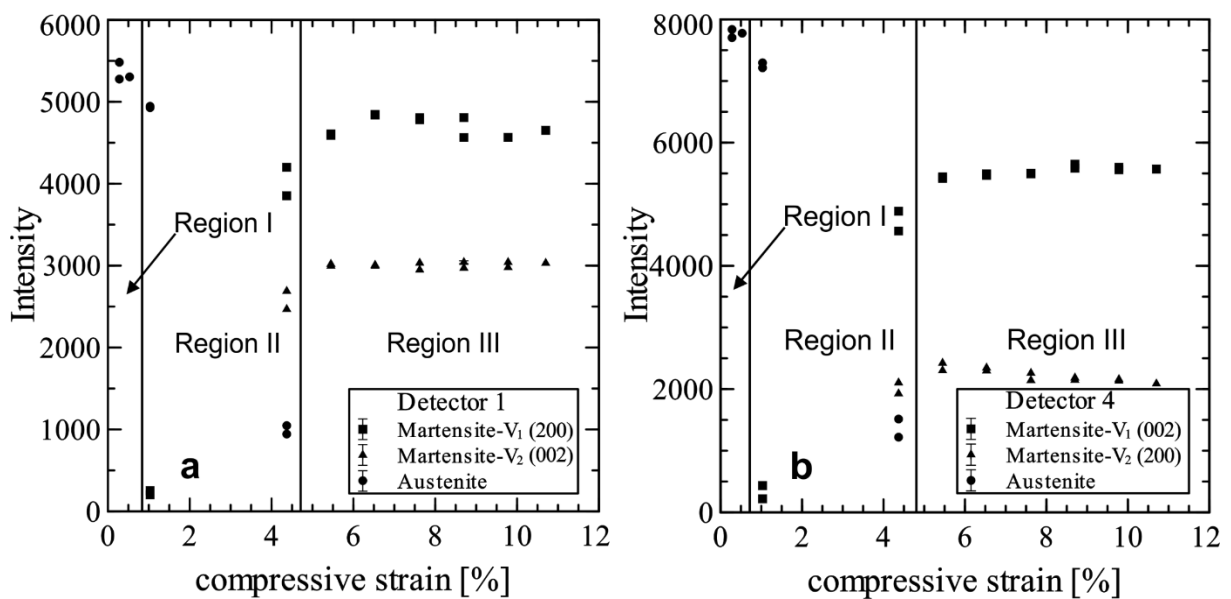


Fig. 7.3: Diffraction intensity plotted as a function of compressive strain. A higher intensity of V_1 during formation of stress-induced martensite (region II) demonstrates its favored growth with respect to V_2 . Constant intensities in region III reveal a constant volume fraction of both martensite domain variants.

The reverse transformation to austenite occurs at a constant plateau stress and its beginning is indicated by the formation of a weak austenite reflection between two strong martensite

reflections at a total strain of 4.3 % as marked in Fig. 7.1g. Finally, Fig. 7.1 h reveals the austenite as the dominant stable phase after unloading, indicating full strain recovery after a superelastic deformation following one cycle up to highest stresses and strains as detailed before.

7.1.4 Discussion

In this study in-situ neutron diffraction was employed to reveal the evolution of phase state and martensite domain variants upon stress induced martensite deformation of Co-Ni-Ga single crystals with an emphasis on the elastically strained martensite. For this, a newly installed testing setup on the SXD diffractometer was employed for the first time. The results obtained reveal a unique stress-strain response of Co-Ni-Ga single crystals in a [001] orientation. As expected, the plateau region is characterized by the transition from initial austenite to stress induced martensite upon loading of the sample. A similar transformation behavior of as-grown [001]-oriented $\text{Co}_{49}\text{Ni}_{21}\text{Ga}_{30}$ single crystals in compression at room temperature was described in (Dadda et al. 2010) and (Dadda et al. 2008); however, in these studies single crystalline material was only deformed to the end of the stress-strain plateau, i.e. to about 4.3 % strain. Furthermore, no microstructural information from the bulk material was provided. In-situ high-spatial resolution optical microscopy characterization only was provided for the surface of the compression samples. The analysis of elementary mechanisms of deformation of a Co-Ni-Ga single crystal beyond the stress plateau and up to 10.7 % strain provides new results broadening both the knowledge on and the application range of this HT-SMA. The formation of initially a single dominating variant of stress-induced martensite followed by a plateau type response with a maximum superelastic strain of 4.3 %, where the single martensite variant has become internally twinned, is in good agreement with the observations of (Dadda et al. 2008, 2010). As already pointed out by (Dadda et al. 2010) in untrained [001]-oriented $\text{Co}_{49}\text{Ni}_{21}\text{Ga}_{30}$ at room temperature, the width of the stress hysteresis is small as the potential generation of dislocations during deformation has only a very minor impact due to lack of suitable glide systems. In the present experiment we also observe that for the same reason the stress-induced martensite can be elastically deformed by another 6 % strain beyond the plateau.

The Bain strain resulting from Pm-3m to P4/mmm martensite elongates the tetragonal c-axis of the martensite and compresses the tetragonal a- and b-axis to provide a volume strain close to zero, as required for shape memory behavior. Thus, in the compressive strain experiment with strain along [001] cubic, the martensite domain variant V_3 with [001] martensite parallel to [001] cubic is suppressed, and only those two variants which have their c-axis perpendicular to

the loading axis, V_1 and V_2 , are formed. Even at the beginning of Region III (Fig. 7.2c,d) there is no evidence for the presence of the third domain variant. Moreover, from the two expected domain variants V_1 and V_2 , only one (labeled V_1) forms initially at the beginning of the stress-induced transformation; only at the end of the plateau the presence of both variants V_1 and V_2 is observed (Fig. 7.3a, b). As the focus of the current study was on the characterization of Region III, we could not locate the onset of the formation of V_2 on the stress plateau precisely. This will be subject of future work. However, in the experiments described by Dadda et al. (2010), the second martensite variant can be expected at least at a strain level of about 3 %.

During compressive deformation up to 10.7 % strain at room temperature, the initial Co-Ni-Ga single crystal runs through three different regimes of elastic or superelastic deformation, respectively (Fig. 7.1j). These are region I = elastic deformation of austenite, region II = phase transformation stress plateau and region III = elastic deformation of martensite. Region III starts at about 4.6 % macroscopic strain and continues up to the maximum load applied which gave 10.7 % strain. Since an elastic deformation of about 6 % is quite unusual for metallic alloys, the microstructural mechanisms which are accountable for the enormous elastic deformation of the martensite need to be analyzed in detail. Furthermore, the formation of a small hysteresis upon unloading in region III indicates a that the deformation of martensite in region III is not solely elastic, but there is a small non-elastic contribution. Thus, the following non-elastic potential mechanisms during deformation in region III need to be evaluated in light of the evolving stress hysteresis: (i) detwinning and concomitant phase/twin boundary friction, (ii) plastic deformation of the sample perpendicular to the loading axis, (iii) interaction/friction between the sample and the grips

The hysteretic stress-strain response could be rationalized by the occurrence of detwinning, due to frictional energies at variant-variant boundaries (Bhattacharya 2003; Laplanche et al. 2017). However, in the elastic martensite region, the volume ratio of both martensite domain variants remains nearly constant (Fig. 7.3). Hence, detwinning can be excluded as a potential explanation for the small stress-strain hysteresis seen. Plastic deformation of the material can be excluded as well, as the original austenite state is fully recoverable without residual strains (Fig. 7.1j, red dot highlighted “h”).

The lattice strain evolution along the c -axis (as measured by the lattice spacing $d_{(002)}$) and a -axis (as measured by $d_{(200)}$) of both martensite domain variants, and normalized with respect to the corresponding d -spacings of martensite at the end of the plateau for each loading stage in the elastic martensite region is summarized in Fig. 7.4a, b. According to the diffraction geometry used, lattice strains were only measured transverse to the load axis. The elastic lattice

strain for both crystallographic directions is distinctly non-linear; it is positive in c-direction and negative in a-direction, where the c-axis strain is consistently about twice as high as the absolute value of the a-axis strain.

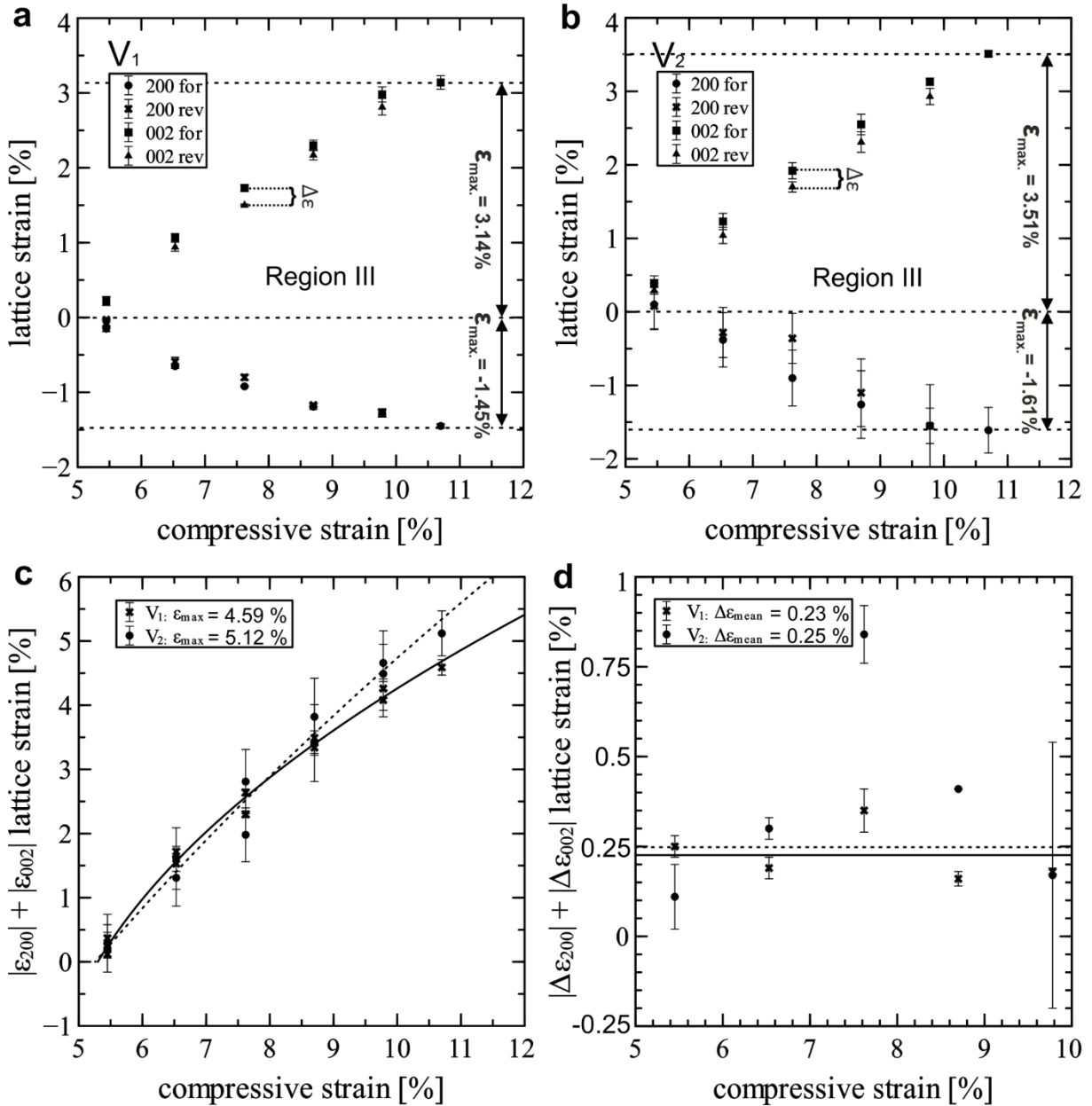


Fig. 7.4: (a,b) Lattice strain evolution of V_1 and V_2 transverse to the load axis for each loading stage, (c) stress-induced elastic lattice strain is non-linear and reaches 5%, while (d) the hysteretic offset is 0.25% strain on average.

Note that the compression of the a-direction is not measured parallel to the compressive load axis, but perpendicular to it. Martensite domain variant V_1 exhibits a maximum elastic lattice

strain of 3.14 % and -1.45 % along the c and a-axis, respectively. Martensite domain variant V_2 follows a very similar trend. The 2: -1 ratio of stress-induced elastic lattice strains along the c-axis and a-axis, respectively, reflects the ferroelastic order parameter of tetragonal Co-Ni-Ga. The spontaneous strain of the austenite to martensite transition displays the 2:-1 ratio such that the volume strain of the martensitic phase transition is zero, an important prerequisite for shape memory behavior (Bhattacharya 2003). Moreover, the non-linearity of the stress-strain response in region III further reflects this order parameter (Khalil-Allafi et al. 2006) (Fig. 7.4c). The total lattice strain of both martensite variants for each loading stage in region III is summarized in Fig. 7.4c revealing 4.59 % (V_1) and 5.12 % (V_2) at maximum applied stress. The unloading curve in region III reveals a small, but quantifiable stress-strain hysteresis for both martensite variants (Fig. 7.4a, b). The resulting lattice strain difference between loading and unloading is denoted as $\Delta\varepsilon$ and plotted in Fig. 7.4d. The hysteretic offset in lattice strain of V_1 and V_2 for any given macroscopic strain (as set in strain-controlled operation mode of the testing apparatus) is fairly constant at 0.23 % and 0.25 % (Fig. 7.4d), while the elastic strain in region III, i.e. for martensite, is in the order of 5 % for the maximum applied load (Fig. 7.4c). As detailed before, detwinning in the part of the specimen which was probed by the neutron beam can be excluded just like presence of a new, alternative twinning mode. Thus, we assume that the small observed stress-strain hysteresis in region III is an effect generated by self-accommodation in relation to the friction of the specimen in contact with the piston surfaces. This friction will prevent free lateral (transverse) deformation and pose local boundary conditions to austenite/martensite/twin self-accommodation which are different from the central, bulk part of the sample, where transverse deformation is rather free to occur. As the neutron beam is limited to avoid irradiation of the stress pistons, any processes occurring at the piston/sample interface are not visible directly in the diffractograms, but they would be visible in the observed stress-strain behavior. Consequently, none deteriorating elementary deformation mechanism seem to be activated at highest level loading of the stress induced martensite in [001]-oriented Co-Ni-Ga HT-SMA.

7.2 Effect of nanometric γ' precipitates on the stress-induced martensitic transformation in [001]-oriented $\text{Co}_{49}\text{Ni}_{21}\text{Ga}_{30}$ shape memory alloy single crystals

7.2.1 Aim of this study

A strong microstructural dependence of thermally induced martensite on size and morphology of the γ' precipitates has been reported by (Chumlyakov et al. 2012; Kireeva et al. 2013). In case of superelastic testing a more complex and multi-variant martensitic microstructure is supposed to dominate the stress-induced martensite transformation (SIMT) (Kireeva et al. 2014). So far, no studies are available in literature showing detailed microstructural investigations identifying the influence of γ' precipitates on the SIMT, martensite variant selection and martensite morphology, respectively. Dadda et al. (2006, 2008, 2010) only analyzed the complex microstructure evolution during SIMT as affected by temperature and training procedures in as-grown Co-Ni-Ga single crystals. The present study focuses on the SIMT of a [001]-oriented $\text{Co}_{49}\text{Ni}_{21}\text{Ga}_{30}$ single crystal in solution-annealed (precipitate-free) and aged condition. Fundamental differences in microstructure evolution were found and interrelationships between finely dispersed γ' precipitates and the MT are established.

7.2.2 Experimental details

Transmission electron microscopy (TEM)

Microstructural characterization of γ' precipitates was conducted using a transmission electron microscope (TEM) operating at a nominal voltage of 200 kV. For TEM work, small disk were cut perpendicular to the [001] crystal direction of the austenite. For further details the reader is referred to chapter 6.4.

In situ optical microscopy (OM)

For compression tests a single specimen with geometry of $4 \times 4 \times 8 \text{ mm}^3$ was used. Quasi-static uniaxial single cycle compression experiments were conducted at $100 \text{ }^\circ\text{C}$ on a servo-hydraulic test frame in displacement control at a nominal strain rate of $1 \times 10^{-3} \text{ s}^{-1}$ up to a maximum strain of -5 % upon loading and a minimum load of -200 N for unloading. The selected test temperature ensured a fully austenitic state prior to superelastic testing of both sample conditions. Strains were measured using a high-temperature extensometer with a gauge length of 12 mm directly attached to the grips. For calculation of the nominal strain the grips were

treated as absolutely rigid. In situ OM analysis was performed at various stages of the superelastic stress-strain hysteresis. For further details the reader is referred to chapter 6.2.

In situ neutron diffraction (TOF)

In situ neutron diffraction was carried out using the single-crystal diffractometer SXD at the ISIS neutron source, Rutherford Appleton Laboratory, Oxfordshire. Uniaxial compression tests were performed under the same conditions as in the in situ OM experiment. Diffraction data were recorded during each loading stage in the austenitic and martensitic state for 20 and 130 min, respectively. Displacement at each loading stage was derived from stress values from the in situ OM experiment. For further details the reader is referred to chapter 6.3 and Keen et al. (2006).

7.2.3 Results and discussion

Upon solution-annealing at 1200 °C, Co-Ni-Ga single crystals feature a single-phase microstructure as proven by TEM (not shown). Aging treatments at relatively low temperatures are effective for the formation of finely dispersed coherent second phase precipitates in the austenitic matrix (Chumlyakov et al. 2012; Kireeva et al. 2013). After aging at 350 °C for 1 h, selected area diffraction (SAED) patterns (Fig. 7.5a) obtained from the $[001]_{B2}$ zone axis reveal reflections attributed to the γ' phase (marked by the white arrows in (Fig. 7.5a). The γ' precipitates ($L1_2$, as revealed by the fast Fourier transformation (FFT) pattern (inset in Fig. 7.5b)) feature a spheroidal shape with diameters up to 5 nm, which is in good agreement to other studies (Chumlyakov et al. 2012; Kireeva et al. 2013).

Fig. 7.6 shows the compressive superelastic response at 100 °C of the $[001]$ -oriented single crystalline $Co_{49}Ni_{21}Ga_{30}$ specimen in solution-annealed and aged condition, respectively. Both conditions demonstrate excellent SE revealing fully reversible MT. The solution-annealed condition is characterized by a low critical stress σ_{cr} for MT of about 160 MPa, a narrow stress hysteresis $\Delta\sigma$ of 30 MPa, a transformation strain ϵ_{tr} of -4.2 % and a plateau-type character of the forward transformation. These functional properties are in excellent agreement with the superelastic behavior being already reported for solution-annealed (Niendorf et al. 2015) and as-grown (Dadda et al. 2006; Kireeva et al. 2009) Co-Ni-Ga single crystals. The subsequent aging treatment leads to the formation of finely dispersed γ' precipitates (Fig. 7.5) and causes a substantially different stress-strain response, i.e. an increase of both, σ_{cr} and $\Delta\sigma$, a decrease of ϵ_{tr} as well as strain -hardening during forward transformation (Fig. 7.6).

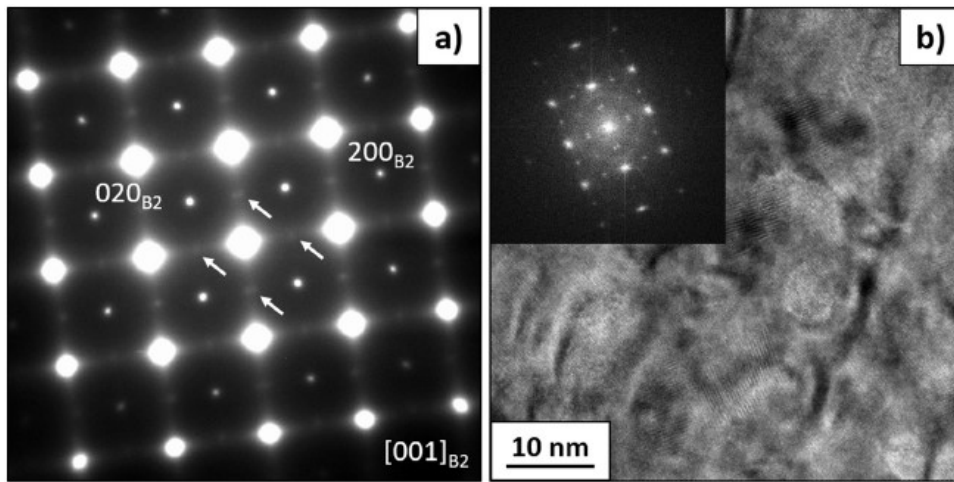


Fig. 7.5: TEM analysis of the $\text{Co}_{49}\text{Ni}_{21}\text{Ga}_{30}$ alloy following solution-annealing and aging at $350\text{ }^{\circ}\text{C}$ for 1 h. (a) SAED pattern with diffuse superlattice reflection spots of the γ' phase marked by the white arrows. (b) HRTEM image of γ' precipitates formed after aging. The inset shows the corresponding FFT pattern obtained in the $[001]_{\text{B}_2}$ zone axis.

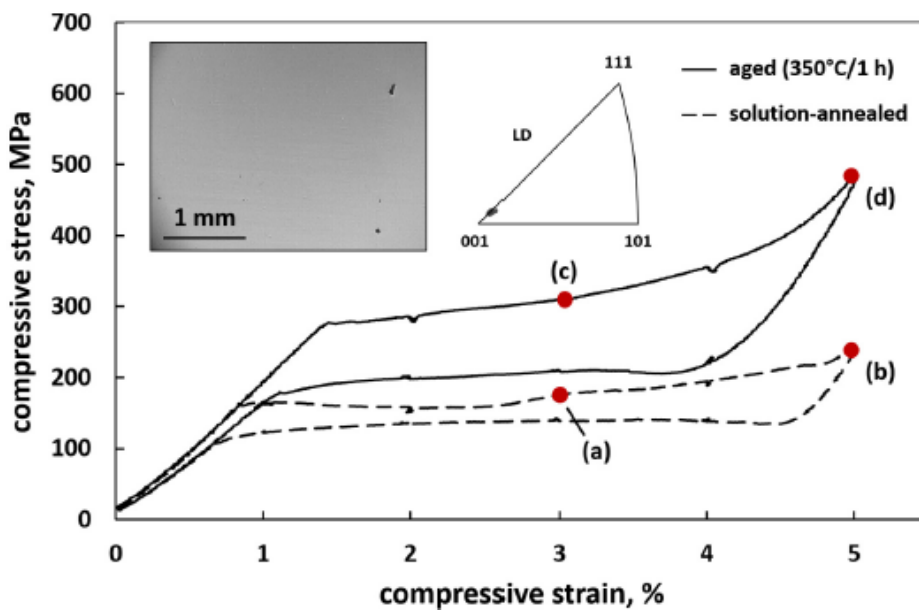


Fig. 7.6: Stress-strain curves of a $[001]$ -oriented $\text{Co}_{49}\text{Ni}_{21}\text{Ga}_{30}$ crystal, solution-annealed (lower hysteresis) and subsequently aged (upper hysteresis), under compressive load at $100\text{ }^{\circ}\text{C}$. The optical micrograph and the inverse pole figure show the reference austenitic microstructure of the specimen taken in the unloaded solution-annealed condition before testing and the orientation of the austenitic phase with respect to the loading direction (LD), respectively. The red points (a)-(d) correspond to the optical micrographs shown in Fig. 7.7.

In general, the underlying microstructural mechanisms responsible for these differences are reported in literature (Chumlyakov et al. 2012; Kireeva et al. 2013, 2014; Kretinina et al. 2015; Gerstein et al. 2018). Three terms additively contribute to the increased value of σ_{cr} , imposed by a change in the chemical and non-chemical contributions of the Gibbs free energy: The nanometric precipitates result in a change in the chemical composition of the matrix, an increase of the elastic energy accumulated during MT, and more pronounced energy dissipation. The last term mainly results from increased frictional work during interfacial motion and dissipation of high interfacial energy. This type of energy dissipation during superelastic loading is induced by complexly accommodated martensite in the vicinity of the precipitates. So far, this was only indicated for thermally induced $L1_0$ martensite (Kireeva et al. 2013, 2014). In fact, a complex multi-variant accommodation of martensite lowers the transformation strain and is decisive for the stress-hardening and the increased hysteresis values (Dadda et al. 2010; Kireeva et al. 2013, 2014). However, in order to shed light on these elementary microstructural mechanisms, the influence of the γ' precipitates on stress induced martensite will be presented and discussed in the following focusing on the martensite variant selection and morphology.

Expectedly, the presence of γ' precipitates strongly affects the SIMT, as evidenced by the in situ OM analysis. Fig. 7.7 shows optical micrographs that were recorded for the solution-annealed (Fig. 7.7a, b) and aged (Fig. 7.7c, d) condition at -3 % and -5 % strain upon loading, respectively. The reference austenitic microstructure of the specimen recorded before testing is shown in the inset of Fig. 7.6. For the sake of brevity, this study focuses only on the forward MT. In terms of the solution-annealed condition, the micrograph shown in Fig. 7.7a reveals a lamellar martensitic microstructure with a dominant martensite plate (top right corner) and a few additional smaller ones coexisting with the untransformed austenite (A) at -3 % strain. Martensite plates separated by a direct interface to austenite are termed habit plane variants (HPVs) in the following, and each martensite plate comprises two twin-related domain variants (Niklasch et al. 2008; Reul et al. 2018), referred to as correspondent variant pair (CVP). The HPVs in Fig. 7.7a featuring the same crystallographic orientation with respect to the loading direction, consist of the same CVP, referred to as CVP_1 . Following straining of the specimen to -5 % (Fig. 7.7b), the MT is fully accomplished without the formation of differently oriented HPVs. In consequence, the MT of the solution-annealed single-phase condition is characterized by the formation of a single (internally twinned) variant of stress-induced martensite, i.e. CVP_1 . (Fig. 7.7a, b). This heterogeneous transformation behavior (Dadda et al. 2010) is in excellent agreement with as-grown [001]-oriented $Co_{49}Ni_{21}Ga_{30}$ single crystals (Dadda et al. 2010; Reul

et al. 2018) The narrow stress hysteresis and plateau-type character of the forward transformation (Fig. 7.6) can be explained by the growth of this single CVP. Due to low interfacial friction, phase fronts can easily move during the SIMT (Dadda et al. 2006, 2008).

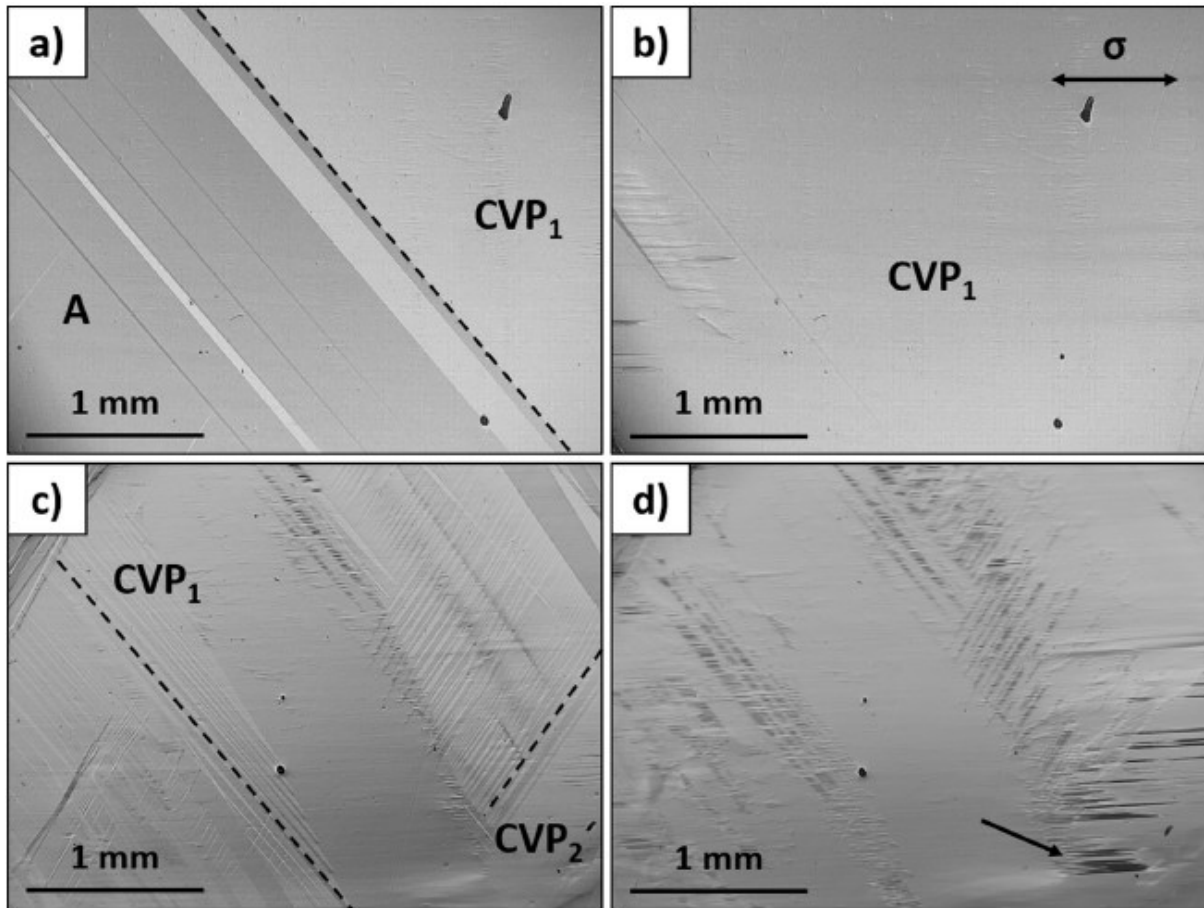


Fig. 7.7: In situ OM analysis of the $[001]$ -oriented $\text{Co}_{49}\text{Ni}_{21}\text{Ga}_{30}$ specimen in the solution-annealed (a, b) and aged (c, d) condition under compression at $100\text{ }^{\circ}\text{C}$. The micrographs show a lateral $[100]$ surface and were recorded at the marked positions of the stress-strain curves in Fig. 7.6, i.e. (a, c) and (b, d) at -3% and -5% strain, respectively. Loading direction is marked in the upper right corner of image (b).

As revealed by the optical micrographs in Fig. 7.7c, d precipitation of nanometric γ' precipitates affects the martensite variant selection and the morphology of the stress-induced martensite. In addition to the initial CVP_1 (Fig. 7.7a, b), the forward transformation of the aged condition is characterized by evolution of HPVs of a second orientation with respect to the loading direction (both orientations are marked by dashed lines in Fig. 7.7c). Furthermore, the phase transformation proceeds by simultaneous formation of numerous interfaces. In contrast to the

well-defined habit planes prevailing during the MT in the solution-annealed condition (Fig. 7.7a), pronounced interactions among these various moving phase boundaries lead to local evolution of distorted interfaces. This phenomenon is observed especially when HPVs of different orientations interact with each other. This complex self-accommodated type of martensite configuration being indicative for a quasi-homogenous MT behavior in SMAs (Shaw and Kyriakides 1995), impedes a reliable identification of the number of variants. Hence bulk data obtained by neutron diffraction experiments were used to shed light on the martensite variants selection. For this purpose, the specimen in the aged condition, which was already probed in the in situ OM analysis (Fig. 7.6 and Fig. 7.7,d), was investigated in a subsequent in situ neutron diffraction experiment at 100 °C at the ISIS neutron source.

The diffractograms shown in Fig. 7.8 correspond to the unloaded, entirely austenitic state before testing (Fig. 7.8a) and to states upon applying strains of -3 % (Fig. 7.8b) and -5 % (Fig. 7.8c), respectively. The diffractogram at -3 % strain shows an austenite reflection (A) in between four martensite domain variant reflections (V_1 - V_4) confirming the aforementioned observations. The formation of habit planes under load leads to a slight misorientation between different austenitic parts of the sample as indicated by vertical splitting of the austenite reflection. Thus, precipitation of finely dispersed γ' - precipitates causes the formation of two differently internally twinned types of HPVs, i.e. CVP_1 and CVP_2 . Based on analysis of the diffraction spots, the martensite domain variants V_1/V_2 and V_3/V_4 each form a CVP. Upon loading to -5 % strain the formation of stress-induced martensite is completed as indicated by the annihilated reflection of austenite. Additional domain variants were not detected as seen in the corresponding diffractogram. However, the optical micrograph at -5 % strain indicates partial detwinning in strip-like structures (as already indicated in (Niklasch et al. 2008)), which are oriented nearly parallel to the loading direction (marked by the black arrow in Fig. 7.7d). Martensite detwinning of internally twinned CVPs is induced by growth of one of the domain variants within a CVP via twin boundary motion. By analyzing the diffraction intensities as a function of the applied compressive strain (Fig. 7.8d) the detwinning process upon loading can be further substantiated. The intensity ratios V_1/V_2 and V_3/V_4 change upon straining from -3 % to -5 %, clearly indicating an increase of volume fraction of one of the domain variants at the expense of the other one, i.e. detwinning.

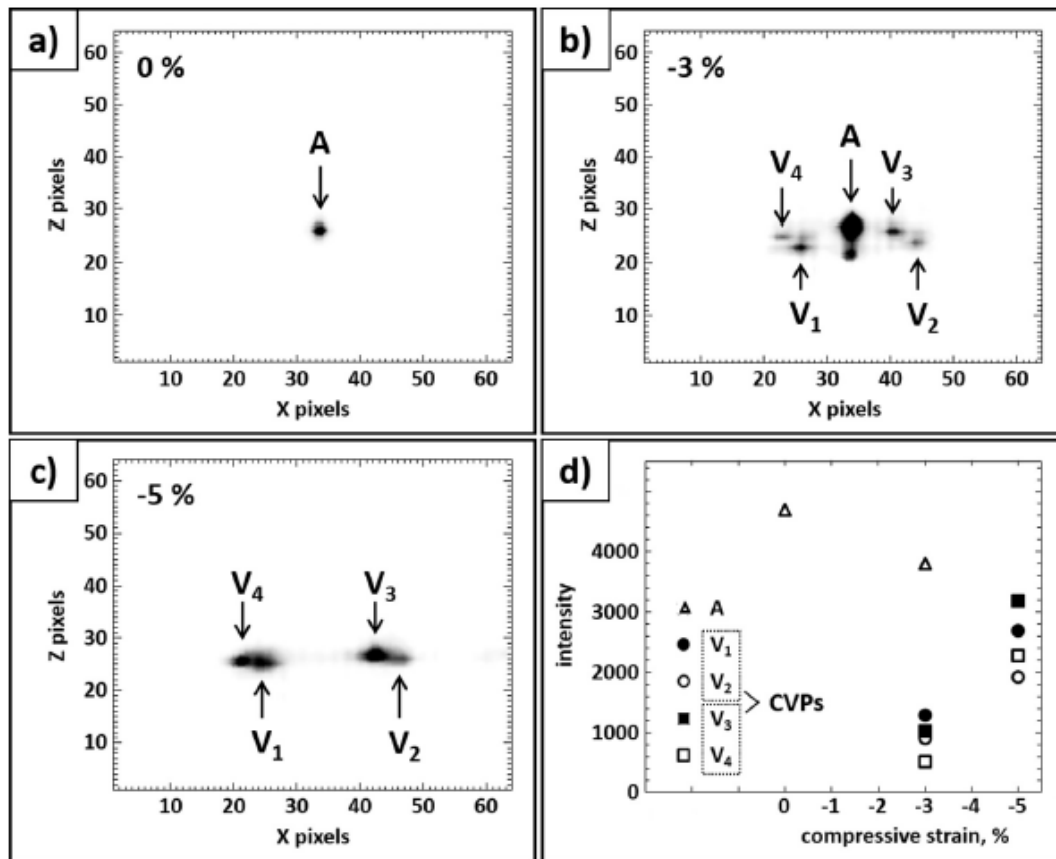


Fig. 7.8: *In situ* neutron diffraction analysis of the [001]-oriented $Co_{49}Ni_{21}Ga_{30}$ specimen in the aged condition during a superelastic single cycle experiment under compressive load at 100 °C. Diffractograms (a-c) were obtained in load-free states as well as upon -3 % and -5 % of strain. The diffraction intensity plotted as a function of compressive strain is illustrated in (d). (See figure A2 in the appendix for diffraction intensities as a function of d -spacing obtained at zero and -5 % macroscopic compressive strain)

Even though only partial detwinning is observed, this is not expected for the [001]-direction under compressive loading in Co-Ni-Ga based on theoretical calculations (Dadda et al. 2008). Furthermore, nanometric precipitates have been reported to hamper the detwinning process (Kireeva et al. 2014). In conclusion, the role of precipitates in SMAs needs to be reconsidered carefully, as new high-performance applications of precipitation-hardened alloy systems are potentially enabled by additional detwinning strains. Indeed, further work is needed to reveal the full potential of differently designed precipitates on the detwinning mechanism.

Beside these observations for Co-Ni-Ga other microstructural factors can lead to a multi-variant martensite selection. Dadda et al. (2006, 2010) demonstrated the presence of a multi-variant self-accommodated martensite morphology upon SIMT owing to diffusion of point defects and

kinetic pinning-induced martensite stabilization (Kustov et al. 2004) at elevated temperatures above 120 °C (Kustov et al. 2004; Dadda et al. 2010). This mechanism is negligible here due to the relatively low test temperature of 100 °C as can be deduced from the heterogeneous transformation behavior of the solution-annealed condition (Fig. 7.6). In the present study the complex martensite microstructure of the aged condition results from coherency stress fields imposed by the nanometric precipitates (Gall and Sehitoglu 1999). Unlike CVP₁, which is favored by the external applied stress, the formation of CVP₂ is obviously promoted due to its favorable orientation to the stress fields existing around the γ' precipitates (Gall and Sehitoglu 1999; Hamilton et al. 2004; Kireeva et al. 2014). In addition, the refinement of the L1₀ martensite (formation of numerous interfaces during stress-induced MT (Fig. 7.7c) results from both, difficulties in shaping the martensite within the irregular stress fields around the precipitates and an increase in elastic energy accumulation owing to significant elastic deformation of the non-transforming particles and the surrounding matrix (Kireeva et al. 2013, 2014). Such a microstructure with pronounced variant-variant interactions is the origin of irreversible process during SIMT contributing to the different stress-strain response in terms of the stress hysteresis, stress hardening and transformation strain in comparison to the single-phase condition (Fig. 7.6). The increased stress hysteresis is also induced by the observed detwinning process, which is known to promote mechanical stabilization of martensite (Chernenko et al. 2004). Further clarification is needed regarding cyclic stability and fatigue life, not only for precipitation-hardened Co-Ni-Ga SMAs, but also for other SMAs, e.g. iron-based SMAs, in which the presence of precipitates is a prerequisite for a thermoelastic MT (Tanaka et al. 2010; Krooß et al. 2014).

7.3 On the impact of nanometric γ' precipitates on the tensile deformation of superelastic $\text{Co}_{49}\text{Ni}_{21}\text{Ga}_{30}$

7.3.1 Aim of this study

In previous investigations (Kireeva et al. 2014; Lauhoff et al. 2019b) the SE response of $\text{Co}_{49}\text{Ni}_{21}\text{Ga}_{30}$ single crystals containing nanometric γ' precipitates showed a significantly increased stress hysteresis width ($\Delta\sigma$, as defined in the inset in (Fig. 7.9) as compared to solution-annealed and as-grown material (Dadda et al. 2010) in compression. The increased stress-hysteresis was rationalized based on the increased frictional energy impeding habit plane motion when γ' precipitates are present. The question remained whether this friction is caused by (i) triggering of microstructures with multiple domains and multiple orientations of habit planes by the γ' precipitates as observed under compression (Lauhoff et al. 2019a) or (ii) direct interaction of γ' precipitates with the moving austenite-martensite phase boundary. To tackle this prevailing research gap, *in situ* experiments using neutron diffraction and optical microscopy were performed focusing on the SE response of $\text{Co}_{49}\text{Ni}_{21}\text{Ga}_{30}$ single crystals under tensile loads for three states of the material: a) as-grown, b) solution-annealed and, c) aged, i.e. only the latter containing well-defined γ' precipitates. In [001]-oriented Co-Ni-Ga single crystals under tensile load, the formation of a multi-variant microstructure is supposed to be suppressed as pointed out by theoretical calculations (Monroe et al. 2010) and experimental results (Niendorf et al. 2013; Krooß et al. 2015, 2016). However, up to now, no studies are available discussing the role of the morphology and variant selection of stress-induced martensite under tensile loading. Focusing on three states of the material, a thorough understanding of the stress-induced martensitic transformation is established. This, in turn, will contribute to a comprehensive knowledge about the complex interrelationships between microstructure, MT and functional properties.

7.3.2 Experimental details

In situ optical microscopy (OM)

Quasi-static uniaxial tension experiments were performed at 100 °C at a nominal strain rate of $1.0 \times 10^{-3} \text{ s}^{-1}$ on a servo-hydraulic load frame in displacement control with a fixed nominal strain of 11 % upon loading and a minimum stress of 50 N for unloading. The SE response of $\text{Co}_{49}\text{Ni}_{21}\text{Ga}_{30}$ single crystals was evaluated in single cycle tensile tests on flat dog-bone tensile specimens with a gauge length of 18 mm and a cross section of 1.5 mm x 1.5 mm. For detailed

information on sample preparation the reader is referred to chapter 6.1. Nominal strain was calculated from displacement data. The selected test temperature of 100 °C ensured a fully austenitic state for all sample conditions prior to SE testing allowing for meaningful comparison with data of previous work (Lauhoff et al. 2019a). *In situ* OM analysis of the transforming specimens was employed at selected load stages of the SE stress-strain hysteresis to characterize stress-induced martensite morphology. Surface images were collected on a representative area using a digital microscope. Furthermore, high resolution confocal laser scanning microscopy (CLSM) was employed on the aged specimen using a higher magnification to assess SIM morphology. The CLSM was equipped with a 408 nm violet laser and has a maximum axial and lateral resolution of 10 nm and 120 nm, respectively.

***In situ* neutron diffraction**

In situ neutron diffraction on a tensile specimen in the as-grown condition was carried out under the same conditions as in case of the *in situ* OM experiments using the STRESS-SPEC diffractometer at FRMII, Munich, as described in chapter 6.3. *In situ* neutron diffraction was carried out to assess SIM domain variant selection at selected and pre-defined load stages of the SE stress-strain curve. Diffraction patterns were recorded at a scattering angle of $2\theta = 56^\circ$ using a wavelength of 1.352 Å. The orientation of the load axis with respect to the incident beam was $\chi = 0^\circ$ (load axis vertical to the scattering plane) and $\chi = 90^\circ$ (load axis in the scattering plane, Fig. 6.4). At each loading stage, rocking scan measurements were performed in 0.1° steps at a fixed ω -orientation (orientation of the main sample table with respect to the incident beam) around $\omega \pm 1.5^\circ$ with 10 s data collection for each step. The software package Stress Texture Calculator (SteCa) was used for data extraction (Randau et al. 2011). For further details on the setup of STRESS-SPEC the reader is referred to Hofmann et al. (2006) and Hoelzel et al. (2013).

In addition, *in situ* neutron diffraction was carried out using the single crystal diffractometer SXD at ISIS neutron source, Rutherford Appleton Laboratory, Oxfordshire as described in chapter 6.3. Uniaxial tension tests were performed on a solution-annealed and subsequently aged specimen (i.e. the same specimen before and after aging) under the same conditions as in the *in situ* OM experiments. Diffraction patterns were recorded on six equatorial detectors during each pre-defined loading stage in the austenitic and martensitic state for 30 and 90 min, respectively. For further details on the setup of SXD, the reader is referred to Keen et al. (2006).

7.3.3 Results

Co-Ni-Ga (as-grown)

Fig. 7.9 shows the tensile SE response at 100 °C of the [001]-oriented $\text{Co}_{49}\text{Ni}_{21}\text{Ga}_{30}$ single crystalline specimen in the as-grown condition. The stress-strain curve is characterized by a narrow stress hysteresis $\Delta\sigma$ of 11 MPa, a low critical stress for the onset of stress-induced martensitic transformation σ_{crit} of about 140 MPa and a plateau-type character. This excellent SE behavior with a fully reversible MT is in good agreement with data already reported for as-grown $\text{Co}_{49}\text{Ni}_{21}\text{Ga}_{30}$ single crystals (Krooß et al. 2015).

Fig. 7.10a shows diffraction patterns of the as-grown tensile specimen collected at nine load stages on the stress plateau (region II), where the load axis was oriented vertical and perpendicular to the scattering plane ($\chi = 0^\circ$). For the sake of brevity, only diffraction data of four out of nine diffraction patterns are displayed for the forward transformation. The experiment in $\chi = 0^\circ$ orientation was performed in the range of 2.5 to 9.3 % strain. As revealed by the diffraction pattern (Fig. 7.10a) a single martensite domain variant V_3 (Bain-correspondence variant BCV_3 out of the three possible BCVs, see text below) is formed at the beginning of the stress plateau at 2.8 % strain. The corresponding diffraction peak in region II arises from the (200) lattice plane of domain variant V_3 . Upon further loading to 8.5 % strain the volume fractions of austenitic and martensitic phase decreased and increased, respectively, as can be deduced from the peak intensities in Fig. 7.10a. Furthermore, with the load axis oriented in the scattering plane ($\chi = 90^\circ$), diffraction patterns were collected at seven load stages during the forward transformation in the elastic austenite region I (not shown) and another seven load stages up to 11 % strain in the elastic martensite region III (Fig. 7.10b). The diffraction patterns (Fig. 7.10b) reveal the presence of the single martensite domain variant (002) V_3 throughout region III as well. The corresponding diffraction peaks in region III arise from the (002) lattice plane of domain variant V_3 . Furthermore, constant diffraction intensities from the (002) lattice plane, indicate a constant volume fraction of this single domain variant.

Fig. 7.10c schematically highlights the formation of a correspondent variant pair (CVP) based on the Bain-correspondence variants (BCVs). In the cubic to tetragonal transformation three possible Bain-correspondence variants BCV_1 , BCV_2 and BCV_3 (BCV_1 is not shown) evolve, each with the four-fold axis (c-axis) along one of the cubic austenite axes. Martensite domain variant orientations are derived from the stress-free intergrowth of two BCVs. This necessitates a rotation of the domain variants in relation to the initial orientation of the BCVs.

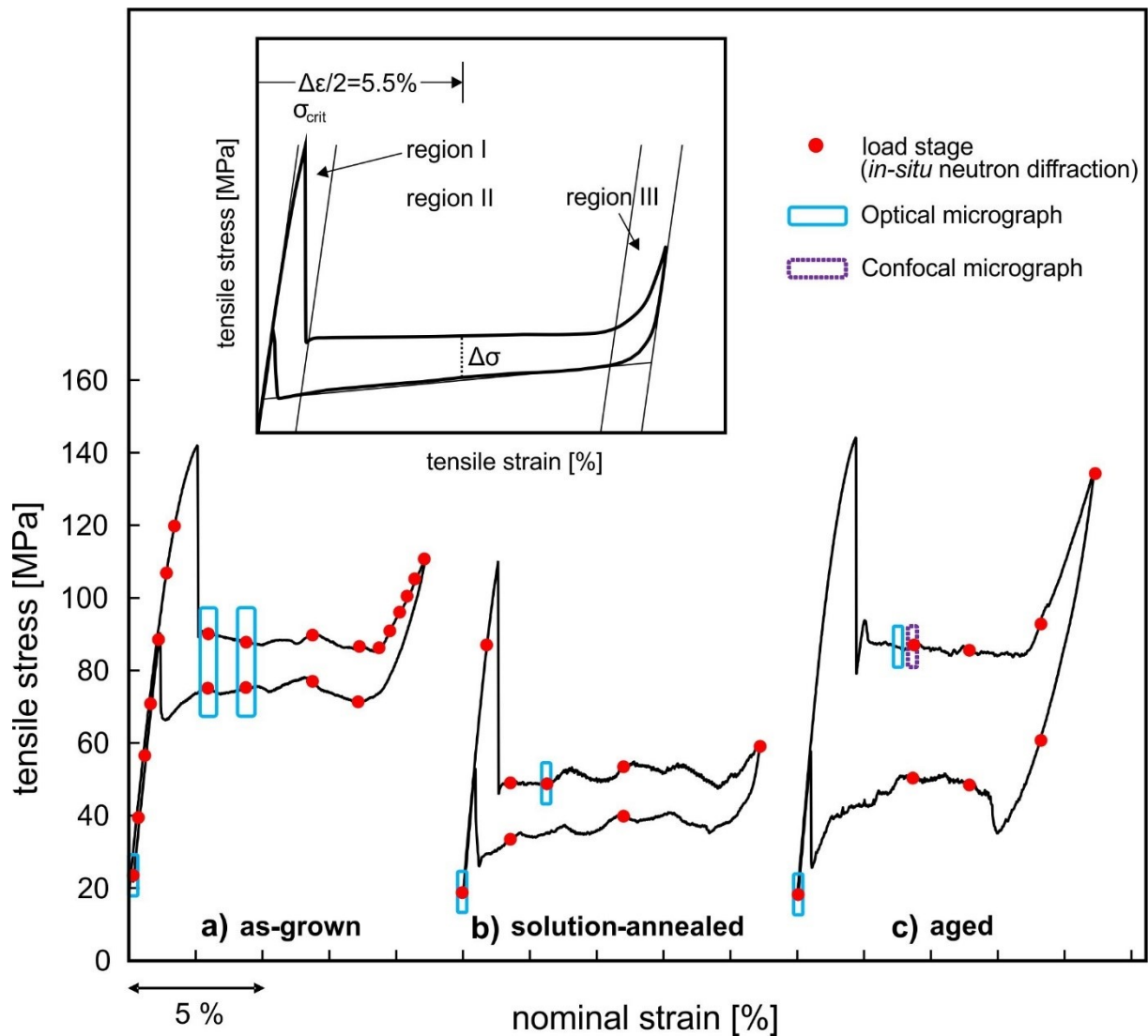


Fig. 7.9: Superelastic stress-strain responses under tensile load at $100\text{ }^{\circ}\text{C}$ of $[001]$ -oriented $\text{Co}_{49}\text{Ni}_{21}\text{Ga}_{30}$ single crystals in the as-grown (a), solution-annealed (b) and aged (c) condition. The stress hysteresis value, $\Delta\sigma$, was measured at half of the applied strain amplitude $\Delta\varepsilon/2$. σ_{crit} is the critical transformation stress level for the onset of stress-induced forward transformation. The elastic austenite region, stress-plateau and elastic martensite region is referred to as region I, region II and region III, respectively. The red dots mark load stages which correspond to the experimental results of neutron diffraction data. The blue and purple rectangles indicate where optical and confocal micrographs, respectively, were taken.

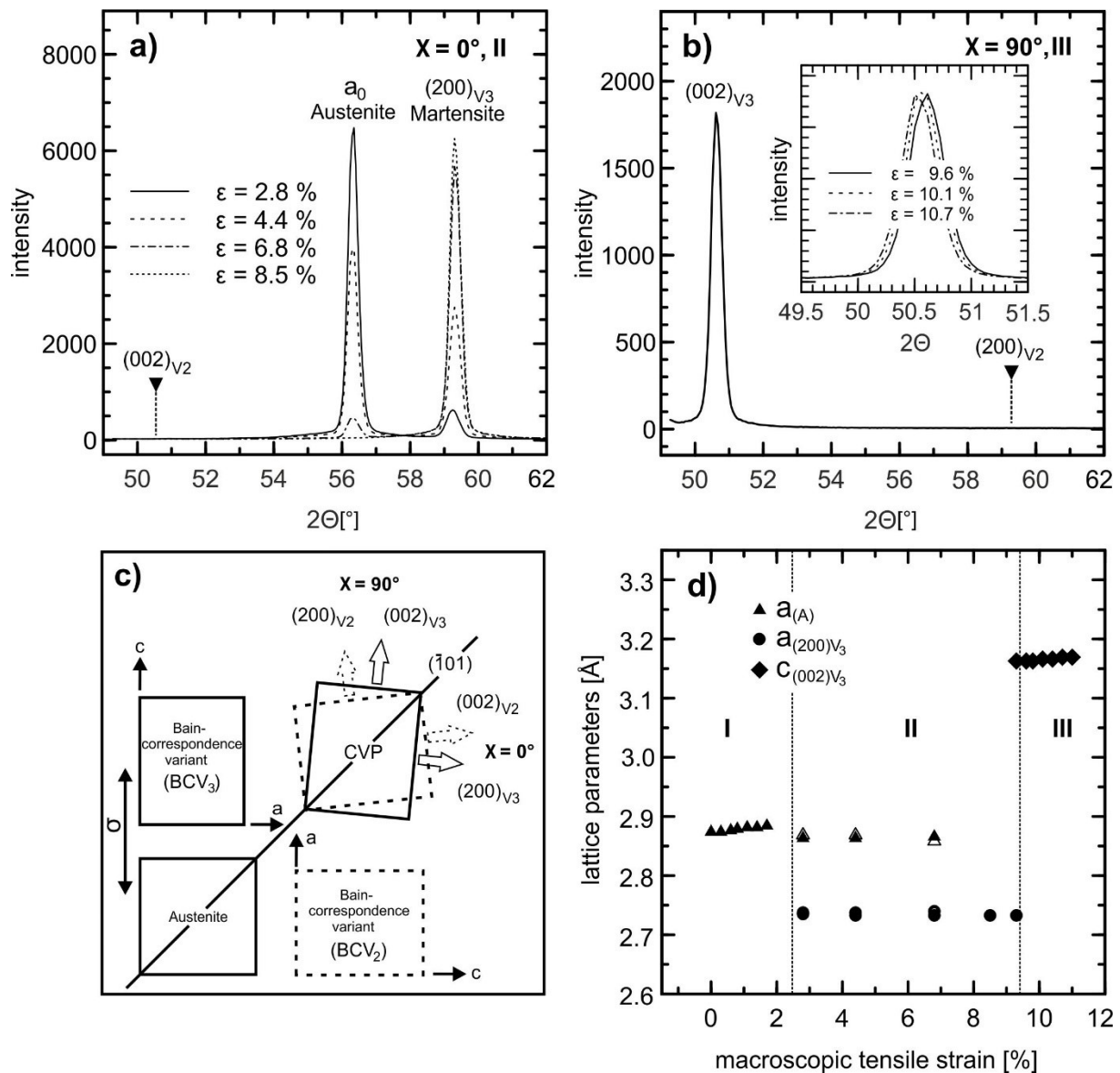


Fig. 7.10: In situ neutron diffraction patterns of a $[001]$ -oriented $\text{Co}_{49}\text{Ni}_{21}\text{Ga}_{30}$ single crystal in the as-grown condition indicate the phase state on the stress plateau (a) and elastic martensite region (b). The schematic (c) illustrates the formation of a correspondent variant pair (CVP) based on the Bain-correspondence variants (BCVs). The CVP comprises domain variant V_2 (dashed rectangle, which is not observed for the present direction of stress) and V_3 (bold rectangle). Lattice parameter evolution as a function of macroscopic strain for austenite (A) and martensite domain variant V_3 is shown in (d). Note, closed and open (region II only) symbols represent the forward and reverse transformation, respectively. The limits of error are within the size of the data points. (See figure A3 and table A2 in the appendix for lattice parameters obtained at each load stage on the stress-strain curve).

Correspondingly, twinning of the pairs BCV_3/BCV_2 , BCV_3/BCV_1 and BCV_2/BCV_1 is possible along a stress-free twin plane of the type $\{110\}$. In the present case, the corresponding domain variants V_2 and V_3 shown in Fig. 7.10c form a CVP. The occurrence of twinned martensite would be revealed by the appearance of two pairs of Bragg-peaks on the corresponding diffraction patterns, i.e. $(200)V_3/(002)V_2$ and $(200)V_2/(002)V_3$ with the load axis vertical to the scattering plane ($\chi = 0^\circ$) and in the scattering plane ($\chi = 90^\circ$), respectively (Fig. 7.10c). Thus, in case of twinned martensite additional diffraction signals would have been detected from $(002)V_2$ and $(200)V_2$ lattice planes at $2\Theta = 50.5$ (Fig. 7.10a) and $2\Theta = 59.5$ (Fig. 7.10b), respectively. However, the obtained diffraction pattern do not indicate such additional domain variants on the stress plateau (Fig. 7.10a) and in the elastic martensite region (Fig. 7.10b). Hence, fully detwinned SIM was observed up to 11 % strain comprising only V_3 (BCV_3), i.e. BCV_1 and BCV_2 , where the extensional c-axis is oriented perpendicular to the $[001]$ tensile load direction, are suppressed.

Space group and lattice parameters are Pm-3m (#221), $a = 2.874(4)$ Å for as-grown austenite in the load free condition and P4/mmm (#123), $a = 2.733(1)$ Å, $c = 3.163(3)$ Å for SIM at the end of the stress-plateau at 9.3 % macroscopic strain (Fig. 7.7d). In region II the lattice parameters of $(200)V_3$ remain nearly constant as a function of strain as the stress is also nearly constant on the stress-strain plateau. In region III, stress increases and, thus, lattice parameters increase correspondingly. A small shift of the $(002)V_3$ peak position to lower 2Θ values indicates an elongation of the BCV_3 c-axis along the tensile loading direction as illustrated by the inset (highlighted for three out of seven load stages in region III) in Fig. 7.10b.

Optical micrographs were obtained during a second SE experiment at specific load stages on the stress-strain curve (cf. blue markers in Fig. 7.9a). Fig. 7.11 shows microstructures of the as-grown $[001]$ -oriented $Co_{49}Ni_{21}Ga_{30}$ tensile specimen, already probed in the neutron diffraction experiment, at 2.8 % and 4.4 % applied strain upon loading (b, c) and unloading (d, e). The loading direction and reference austenitic microstructure of the specimen recorded prior to mechanical testing in the load free condition are displayed in Fig. 7.11a. The forward transformation Fig. 7.11b) is characterized by the formation of a single dominant martensite plate (bottom, V_3) and a shear band with lamellar microstructural features comprising a set of a few well-defined parallel interface boundaries between the untransformed austenite (marked as A in Fig. 7.11b) and martensite. The direct interfaces between the austenitic matrix and martensite, which can be distinguished by an optical contrast, are known as habit planes (hp).

As revealed by in situ neutron diffraction (Fig. 7.10a) the dominant martensite plate and the lamellar martensite plates (martensite lamellae) between the arrangement of parallel habit planes forming a shear band comprise only a single martensite domain variant (V_3).

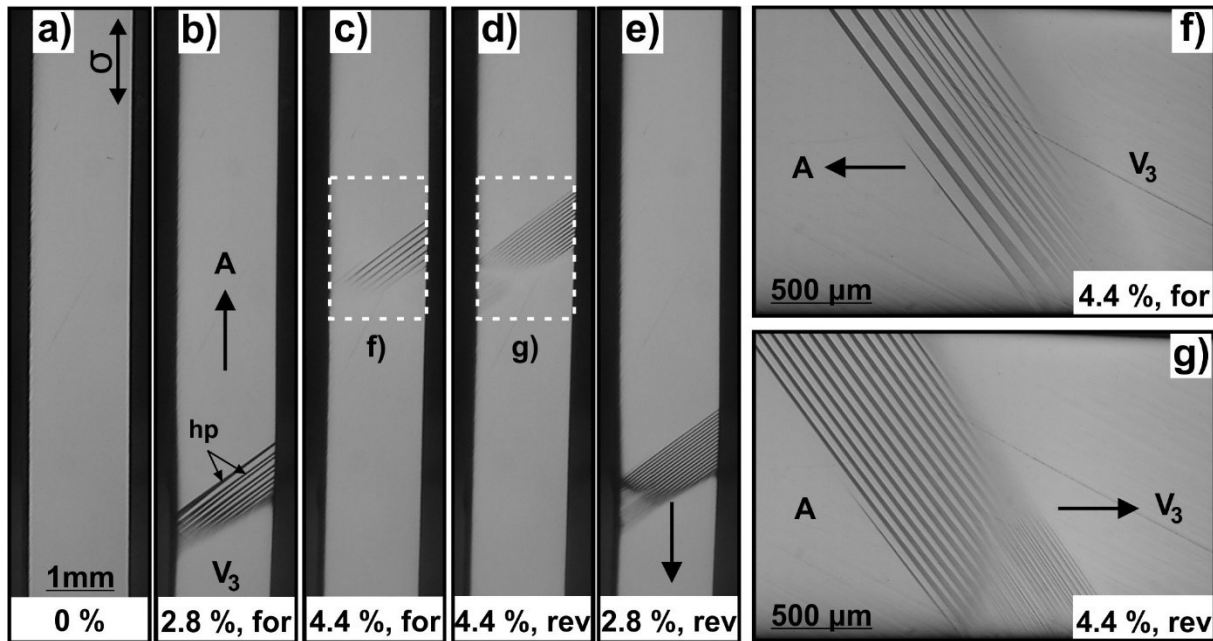


Fig. 7.11: In situ optical micrographs recorded under tension at 100 °C of the as-grown [001]-oriented $Co_{49}Ni_{21}Ga_{30}$ single crystal (the same sample investigated by neutron diffraction, Fig. 7.10). Loading direction is marked in the upper right corner of image (a). Microstructure of SIM at higher magnification is depicted in (f) and (g) at 4.4 % strain during forward and reverse transformation, respectively. The optical contrasts within the shear band are due to alternating austenite/martensite lamellae separated by habit plane (hp) interfaces.

Upon further loading to 4.4 % strain, the martensitic transformation proceeds with the growth of the dominant martensite plate and the movement of the shear band as depicted in Fig. 7.11c and highlighted by the optical micrograph recorded with higher magnification (Fig. 7.11f). The SIM morphology of the moving shear band in Fig. 7.11f is characterized by martensite lamellae between a set of few well-defined parallel habit planes. However, a change of SIM morphology within the shear band becomes obvious during the reverse transformation at 4.4 % and 2.8 % strain (Fig. 7.11d, e and g). Clearly, upon unloading the thickness of the martensite lamellae is reduced (Fig. 7.11g).

Co-Ni-Ga (solution-annealed)

Fig. 7.9b shows the tensile SE response at 100°C of the [001]-oriented $\text{Co}_{49}\text{Ni}_{21}\text{Ga}_{30}$ single crystalline specimen in the solution-annealed condition. The SE behavior is characterized by a narrow stress hysteresis width $\Delta\sigma$ of 11 MPa, a low critical transformation stress σ_{crit} of about 110 MPa and a plateau-type character. These SE characteristics and the fully reversible MT is in good agreement with data already reported for solution-annealed $\text{Co}_{49}\text{Ni}_{21}\text{Ga}_{30}$ single crystals (Monroe et al. 2010; Niendorf et al. 2013).

Diffraction data of the solution-annealed tensile specimen were recorded at nine load stages up to 11 % nominal strain (cf. Fig. 7.9b and Fig. 7.12). For the sake of brevity, only diffraction data of four out of nine diffraction patterns are displayed for the forward transformation. As revealed by the diffraction intensities (Fig. 7.12) the SIM consists of a single domain variant V_3 for both the stress-plateau (region II, 3 % and 6 % in Fig. 7.12) and the elastic martensite region (region III, 11 % in Fig. 7.12).

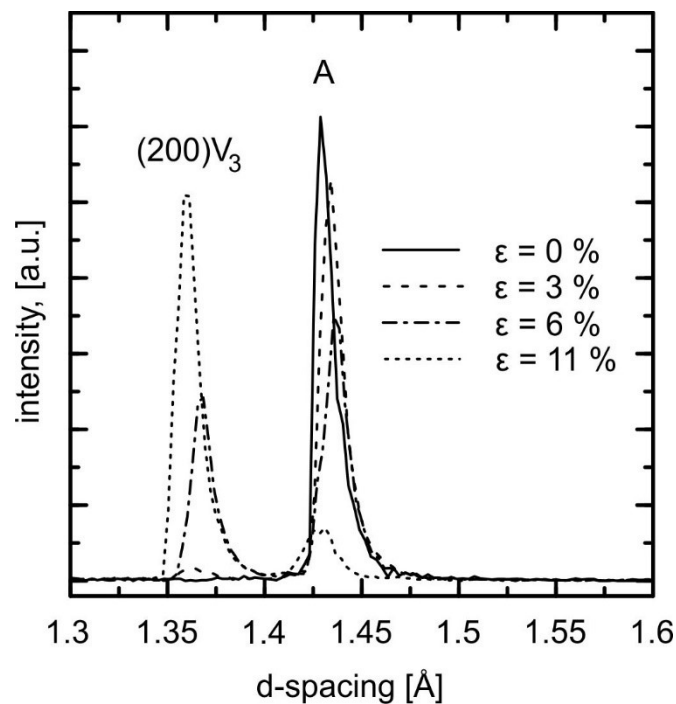


Fig. 7.12: Diffraction intensity as a function of d -spacing obtained at different macroscopically applied tensile strains of a [001]-oriented $\text{Co}_{49}\text{Ni}_{21}\text{Ga}_{30}$ single crystal in the solution-annealed condition. In the transforming specimen only stress-induced martensite domain variant V_3 is found. (See figure A4 and table A3 in the appendix for lattice parameters obtained at each load stage on the stress-strain curve).

In addition, *in situ* OM was previously performed on the same specimen used in the neutron diffraction experiment to assess SIM morphology. Note, as the neutron diffraction experiment revealed the formation of one single domain variant during loading and unloading, optical micrographs are only shown for the forward transformation. Micrographs were recorded at the marked positions of the stress-strain curve in Fig. 7.9b for the reference austenitic microstructure in the unloaded state and at 2.8 % strain upon loading (Fig. 7.13a and b, respectively). The optical micrograph of the solution-annealed tensile specimen recorded at 2.8 % strain upon loading reveals a dominant martensite plate consisting of domain variant V_3 and non-transformed austenite A (Fig. 7.13b). Noteworthy, the shear band is a region of one well-defined martensite lamella and a single habit (hp).

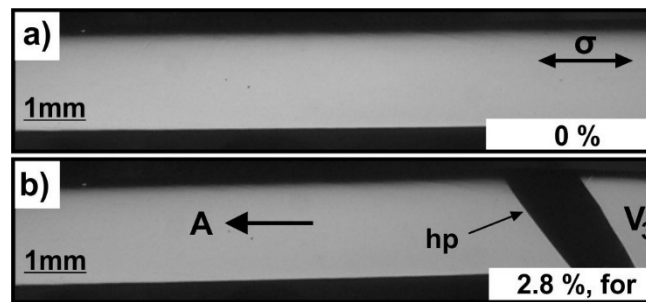


Fig. 7.13: *In situ* optical micrographs of the solution-annealed [001]-oriented $Co_{49}Ni_{21}Ga_{30}$ single crystal (the same sample investigated by neutron diffraction in (Fig. 7.12) under tension at 100 °C. The micrographs were recorded at the marked positions of the stress-strain curve in (Fig. 7.9b) in the unloaded state and at 2.8 % strain upon loading. The loading direction is displayed in the upper right corner of image (a). A: austenite, V_3 : martensite, hp: habit plane, for: forward transformation.

Co-Ni-Ga (aged)

Fig. 7.9c shows the tensile SE response at 100 °C of the [001]-oriented $Co_{49}Ni_{21}Ga_{30}$ single crystalline specimen after aging at 350 °C for 1h. In a previous study (Lauhoff et al. 2019a) it was shown that aging at 350 °C for 1 h leads to the evolution of γ' precipitates with spheroidal shape and sizes up to 5 nm (Fig. 7.14). The segregation of γ' precipitates causes a different stress-strain response in comparison to the as-grown and solution-annealed material states, in particular with respect to $\Delta\sigma$. The SE response is characterized by a fully reversible MT, a plateau-type character and a critical transformation stress σ_{cr} of about 140 MPa. However, the stress hysteresis width $\Delta\sigma$ of 35 MPa is considerably increased (by a factor of about 3).

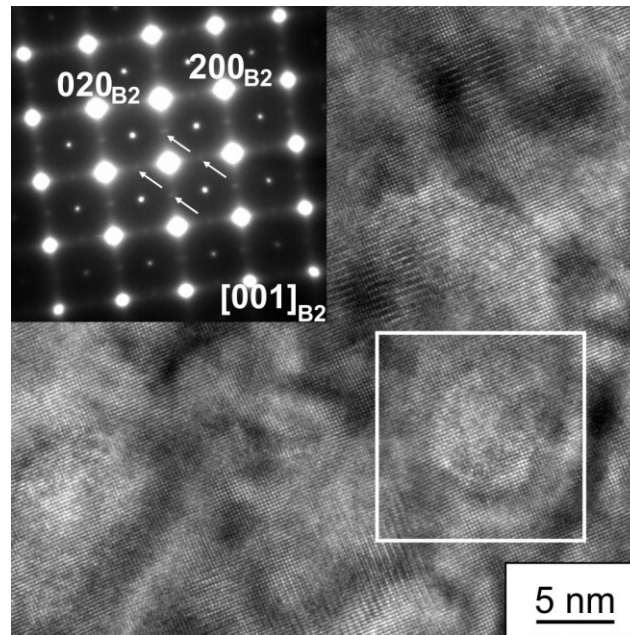


Fig. 7.14: HRTEM image of γ' precipitates formed after aging at 350 °C for 1 h. The spheroidal γ' precipitate within the white rectangle has a size of 5 nm. The inset shows the corresponding SAED pattern with diffuse superlattice reflection spots of the γ' phase marked by the white arrows.

Diffraction data of the aged tensile specimen were recorded at nine load stages up to 11 % nominal strain (cf. Fig. 7.9c). For the sake of brevity again, only diffraction data of four out of nine diffraction patterns are displayed for the forward transformation in Fig. 7.15. As revealed by the diffraction intensities, stress-induced martensite comprises the single domain variant V_3 in both the stress-plateau (region II, 4.3 % and 6.5 % in Fig. 7.15) and the elastic martensite region (region III, 11 % in Fig. 7.15).

In situ OM was performed on the same specimen already used in the neutron diffraction experiment (cf. Fig. 7.15) to assess stress-induced martensite morphology in the presence of γ' precipitates as illustrated in Fig. 7.16b. The optical micrographs were recorded at the marked positions of the stress-strain curve in Fig. 7.9c, i.e. in the unloaded state and at 3.6 % applied strain. The shear band of the aged tensile specimen is characterized by a reduction of martensite lamellae thickness already during the forward transformation in contrast to the few well-defined habit planes and the single habit plane observed in the as-grown and solution-annealed material state, respectively. (Fig. 7.16b). However, difficulties in the visualization of the martensite lamellae within the shear band solely based on OM are obvious (Fig. 7.16b).

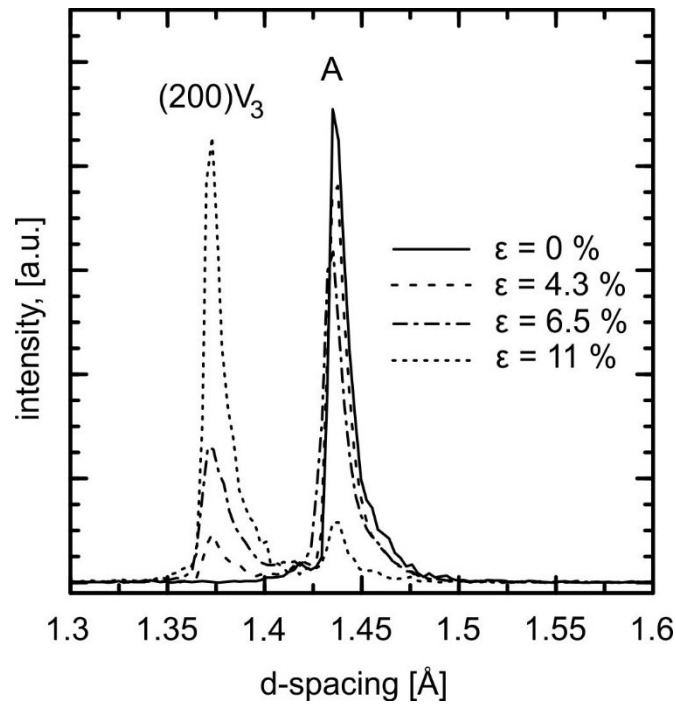


Fig. 7.15: Diffraction intensity as a function of d -spacing obtained at different macroscopically applied tensile strains of a $[001]$ -oriented $Co_{49}Ni_{21}Ga_{30}$ single crystal in the aged (1 h/350 °C) condition. In the transforming specimen only domain variant V_3 is observed. In situ TOF neutron diffraction data are only shown for the forward transformation. (See figure A5 and table A4 in the appendix for lattice parameters obtained at each load stage on the stress-strain curve).

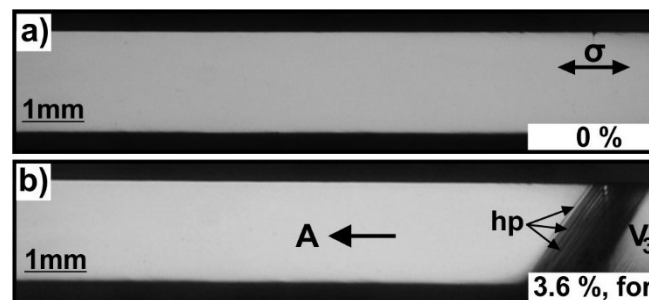


Fig. 7.16: In situ optical micrographs of the aged (1 h/350 °C) $[001]$ -oriented $Co_{49}Ni_{21}Ga_{30}$ single crystal (the same sample investigated by neutron diffraction in (Fig. 7.15) under tension at 100 °C. The micrographs were recorded at the marked positions of the stress-strain curve in (Fig. 7.9c), i.e. in the unloaded state and at 3.6 % strain. Loading direction is marked in the upper right corner of image (a). A: austenite, V_3 : martensite, hp: habit plane, for: forward transformation.

For clarity, a more detailed analysis of the stress-induced martensite morphology within the shear band was conducted by *in situ* confocal laser microscopy. The micrograph shown in Fig. 7.17 was recorded at 4.2 % strain. Besides the obvious reduction of martensite lamellae thickness, lamellae seem to be slightly distorted. Thus, habit planes observed during the forward transformation (Fig. 7.17) are not oriented to the same (well-defined) degree as in case of the as-grown condition (cf. Fig. 7.11f, g).

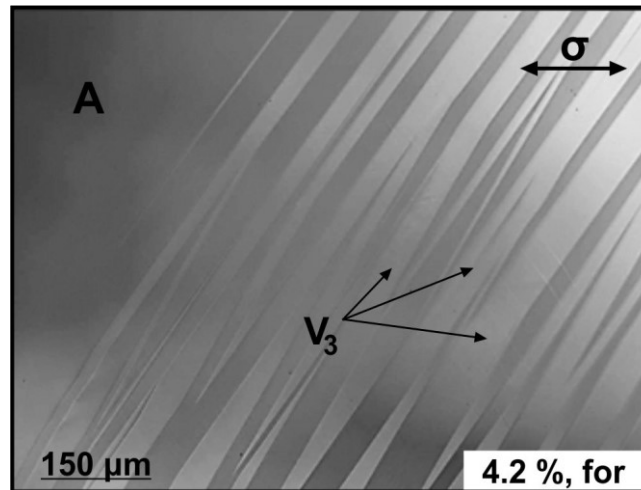


Fig. 7.17: Confocal laser scanning micrograph of the aged (1 h/350 °C) [001]-oriented $\text{Co}_{49}\text{Ni}_{21}\text{Ga}_{30}$ single crystal already shown in Fig. 7.15 and Fig. 7.16. The micrograph was recorded at the marked position of the stress-strain curve in Fig. 7.9c during the forward transformation at 4.2 % strain. Loading direction is marked in the upper right corner. A: austenite, V_3 : martensite, for: forward transformation.

7.3.4 Discussion

The purpose of the present paper is to provide in-depth insights into the underlying microstructural mechanisms leading to the large stress hysteresis width of $\text{Co}_{49}\text{Ni}_{21}\text{Ga}_{30}$ single crystals containing nanometric γ' precipitates (~ 5 nm size) as compared to solution-annealed and as-grown material. Previous investigations (Kireeva et al. 2013, 2014; Lauhoff et al. 2019a) concluded that increased friction of the moving austenite-martensite phase boundary is caused by the γ' precipitates. It was assumed that this could be induced by two different reasons: (i) by triggering of microstructures with multiple domains and multiple orientations of habit planes, which were observed under compressive load eventually leading to pronounced interphase and/or intervariant interactions; (ii) by γ' precipitates acting as obstacles in the path of the moving austenite-martensite phase boundary. In particular, the impact of γ' precipitates on

stress-induced martensite morphology and SE response under tensile loading has not been addressed so far. To provide novel data, *in situ* techniques, i.e. neutron diffraction, optical and confocal laser scanning microscopy, during isothermal single cycle mechanical tests were used to characterize the effect of γ' precipitates in aged specimens in comparison to the solution-annealed reference state being free of any secondary phases and the as-grown condition, which is the most studied material state in literature.

Based on theoretical calculations using the energy minimization theory (Monroe et al. 2010) the formation of one martensite domain variant is favored in tension along the [001] axis. Present bulk information obtained by *in situ* neutron diffraction revealed one single domain variant of stress-induced martensite for all three investigated material conditions being perfectly consistent with theory (Monroe et al. 2010). Thorough diffraction analysis of stress-induced martensite in the as-grown condition demonstrated the presence of a single domain variant V_3 throughout the whole stress plateau (region II, Fig. 7.10a) and elastic martensite region (region III, Fig. 7.10b). In addition, intensities of domain variant V_3 remained constant within the elastic martensite region. Accordingly, the formation of alternative twin domains can be excluded indicating a fully detwinned microstructure during the whole transformation path. Such stress-induced martensitic transformation behavior is also present after both solution-annealing and aging for 1 h at 350 °C, i.e. the thermal treatments conducted have virtually no influence on the martensite variant selection in [001]-oriented single crystals under tensile loading.

Interestingly, the presence of nanometric γ' precipitates following an aging treatment at 350°C for 1 h does not impose multiple domain variants of stress-induced martensite nor habit planes of multiple orientations with respect to the loading direction. As can be deduced from diffraction data in Fig. 7.15, domain variant selection in the aged [001]-oriented $\text{Co}_{49}\text{Ni}_{21}\text{Ga}_{30}$ single crystal does not change up to maximum applied tensile strain of 11 %. In tensile load, Bain-correspondence variant BCV_3 is favored by the external applied stress, whereas Bain-correspondence variants BCV_1 and BCV_2 are suppressed. In compression BCV_1 and BCV_2 are favored while BCV_3 is suppressed (Reul et al. 2018). Previous work (Lauhoff et al. 2019a) on aged $\text{Co}_{49}\text{Ni}_{21}\text{Ga}_{30}$ under compressive load demonstrated the occurrence of multiple domain variants comprising two sets of CVPs formed by BCV_1 and BCV_2 . This phenomenon was attributed to strong coherency stress fields in the matrix due to the formation of small (spheroidal) γ' precipitates (cf. Fig. 7.14). The authors stated that due to the stress fields

introduced by the precipitates multi domain variant microstructures emerge in contrast to material without precipitates in which only a single internally twinned CVP forms under compression (Lauhoff et al. 2019a). The development of strong local stress fields in the matrix due to the formation of small coherent or semi-coherent Ti_3Ni_4 precipitates has been already revealed in NiTi SMAs (Gall et al. 1999). These local stress fields arise from the mismatch in lattice parameters between Ti_3Ni_4 precipitates and the matrix. This resulted in a locally resolved shear stress on the martensite CVPs and the generation of preferential nucleation sites for martensite (Gall et al. 1999). A similar behavior was expected for the aged tensile specimen containing small coherent γ' precipitates (~ 5 nm). In tension, however, the strong local stress fields are not able to promote additional domain variants, as can be deduced from the corresponding diffraction pattern (Fig. 7.15). As a result, despite the presence of nanometric coherent γ' precipitates, the formation of one single domain variant of martensite is favored under tensile load being fundamentally different to the compressive stress state (Lauhoff et al. 2019a).

Optical micrographs revealed significant differences in martensite morphology, in particular, with respect to the number and thickness of martensite lamellae in the shear band. In the as-grown condition, the stress-induced phase transformation proceeds with the propagation of a dominant martensite plate and a shear band of martensite lamellae between a set of few well-defined parallel habit planes (Fig. 7.11b, c). In this material state, the nucleation of few well-defined parallel habit planes during the forward transformation is inferred from chemical inhomogeneities acting as preferential nucleation sites (Dadda et al. 2010; Chumlyakov et al. 2012). During the reverse transformation in the as-grown state, the stress-induced martensite morphology demonstrates an increased number of parallel habit planes in combination with a reduction of martensite lamellae thickness (Fig. 7.11d, e). This effect has been attributed to mismatch dislocations formed during the forward transformation acting as nucleation sites for new interfaces upon unloading (Dadda et al. 2010). In solution-annealed $\text{Co}_{49}\text{Ni}_{21}\text{Ga}_{30}$, the SIMT from B2 to $L1_0$ proceeds with a dominant martensite plate and a well-defined shear band featuring one martensite lamella with one austenite-martensite single interface (Fig. 7.13), which is characteristic for single crystals with low defect density (Salzbrenner and Cohen 1979). In turn, γ' precipitates with spheroidal shape obtained by aging at 350 °C for 1 h (cf. Fig. 7.14) promote the reduction of martensite lamellae thickness and the formation of partially transforming regions within the shear band with slightly distorted, more or less parallel habit planes already during the forward transformation (Fig. 7.16b, Fig. 7.17). This is in good

agreement with the drastic refinement of the martensitic morphology in thermally (Kireeva et al. 2013) and stress-induced martensite (in compression (Lauhoff et al. 2019a)) reported for aged $\text{Co}_{49}\text{Ni}_{21}\text{Ga}_{30}$ single crystals. The refined microstructure was attributed to the elastic deformation of the non-transforming γ' precipitates and the surrounding matrix during MT promoting an increase in elastic energy accumulation and, thus, the reduction in martensite twin thickness (Kireeva et al. 2013).

In the present study for tensile loading the introduction of nanometric γ' precipitates strongly affects the stress-induced martensite morphology and produces a substantially different stress-strain response in relation to the as-grown and solution-annealed (precipitate-free) material. As can be deduced from the stress-strain curves in Fig. 7.9, the stress hysteresis value $\Delta\sigma$ of 35 MPa in the aged condition is about 3 times higher than the solution-annealed and as-grown conditions which showed a $\Delta\sigma$ of 11 MPa. The increase of $\Delta\sigma$ can be attributed to three main energy dissipative processes occurring during MT (Gall and Maier 2002; Monroe et al. 2010; Chumlyakov et al. 2012; Kireeva et al. 2014): The first process is attributed to the dissipation of frictional energy due to the resistance for austenite-martensite phase boundary motion. The second dissipative process is related to the dissipation of stored elastic strain energy due to relaxation of coherency strains at austenite-martensite phase boundaries. The third dissipative process accounts for the dissipation of interfacial energy.

As mentioned before, nanometric γ' precipitates under compressive load impose a complex multi-variant martensite microstructure that has been characterized by two sets of differently oriented parallel habit planes (Lauhoff et al. 2019a). However, the present study focusing on tensile loading revealed only one set of parallel habit planes following an aging heat treatment in $\text{Co}_{49}\text{Ni}_{21}\text{Ga}_{30}$ single crystals and, thus, is characterized by the absence of multi-variant interactions. As a consequence, the increase in frictional energy and its contribution to the large stress hysteresis is mainly attributed to nanometric γ' precipitates acting as obstacles for the moving austenite-martensite phase boundaries.

Concomitantly, there is a strong reduction in martensite lamellae thickness and increased number of habit planes in the shear band due to the elastic deformation of γ' precipitates (Kireeva et al. 2014). Previous studies demonstrated relaxation of coherency strains at austenite-martensite phase boundaries especially when precipitates become incoherent after the transformation (Hamilton et al. 2004) or exceed a critical particle size (Kireeva et al. 2014). In this case, the dislocation density increases at γ' precipitate boundaries causing dissipation of

stored elastic energy eventually increasing the stress hysteresis (Hamilton et al. 2004; Dadda et al. 2008; Kireeva et al. 2014). However, coherent γ' precipitates (~ 5 nm sized) are completely absorbed by the moving habit planes and the whole transformation strain can be accommodated (Kireeva et al. 2013). In this case, dissipation of stored elastic energy is minimized probably due to the absence of dislocations at γ' precipitate boundaries (Kireeva et al. 2013). In consequence, the relaxation of coherency strains at austenite-martensite phase boundaries around coherent γ' precipitates (Hamilton et al. 2004) is of minor importance for the large size of the stress hysteresis in the aged tensile specimen. In addition, γ' precipitate formation comprises a change in the surface and phase boundary energies affecting the macroscopic stress-strain response in terms of $\Delta\sigma$ for stress-induced martensite. Consequently, the reduction of martensite lamellae thickness and increase in number of habit planes (Fig. 7.16) increase interfacial energy contribution and enhance the stress hysteresis width (Kireeva et al. 2014). The small volume fraction of the shear band with respect to the entire sample volume clearly indicates very low, however, detectable interfacial energy dissipation in the aged $\text{Co}_{49}\text{Ni}_{21}\text{Ga}_{30}$ tensile specimen.

The narrow stress hysteresis $\Delta\sigma$ of 11 MPa in both, the solution-annealed and as-grown condition is attributed to an easy propagation of the dominant martensite plate and the shear band due to minimal energy dissipation (Monroe et al. 2010; Chumlyakov et al. 2012). The aged specimen in contrast clearly reveals that the larger stress hysteresis width is governed by nanometric γ' precipitates which act as obstacles for phase boundary movement, while additional contributions to the stress hysteresis such as dissipation of elastic strain energy and interfacial energy play only a minor role. It is worth noting that the introduction of small γ' precipitates (~ 5 nm sized) following an aging treatment at 350 °C for 1 h does not contribute to variant-variant interactions under tensile loading. This fact can be deduced from the occurrence of only one domain variant (Fig. 7.15) in the dominant martensite plate and the shear band (Fig. 7.16). On the other hand, previous work on $\text{Co}_{49}\text{Ni}_{21}\text{Ga}_{30}$ single crystals under compression demonstrated that small γ' precipitates (~ 5 nm sized) trigger multi-variant martensite microstructures, i.e. multiple domains of stress-induced martensite and multiple orientations of habit planes (Lauhoff et al. 2019a). Such kind of microstructure with pronounced variant-variant interactions contributes to dissipation of frictional energy during SIMT which has been concluded to reduce transformation recoverability (Dadda et al. 2010; Krooß et al. 2014, 2015). The present results indicate that aging treatments of Co-Ni-Ga SMAs are not necessarily associated with the formation of multi-variant martensite microstructures. It is

supposed that the impact of γ' precipitates on functional properties in Co-Ni-Ga SMA single crystals is strongly dependent on their size and morphology (Kireeva et al. 2013, 2014).

8 Conclusions

The present study reports on the morphology and domain variant selection of stress-induced martensite in Co-Ni-Ga HT-SMAs. Single cycle compressive and tensile tests were conducted on as-grown, solution-annealed and aged $\text{Co}_{49}\text{Ni}_{21}\text{Ga}_{30}$ single crystals in [001] orientation. Detailed microstructural analysis of stress-induced martensite was performed using *in situ* neutron diffraction, *in situ* optical- and confocal laser scanning microscopy. The main findings can be summarized as follows.

The exploration of the superelastic strain capability has extended the elastic martensite deformation in as-grown [001]-oriented $\text{Co}_{49}\text{Ni}_{21}\text{Ga}_{30}$ single crystals. Detailed structural information on the phase state and domain variant selection from the bulk specimen revealed a simple regular twin structure of stress-induced martensite throughout the whole transformation path. In the cubic to tetragonal transformation twinning of the domain variants V_1 and V_2 is favored with their c-axis perpendicular to the [001] compressive load direction. Both variants form a correspondent variant pair (CVP). Correspondingly, domain variant V_3 with the c-axis parallel to the [001] compressive load direction is suppressed. Lattice strains of elastically deformed martensite were calculated from the lattice spacing along the c- and a-axis of V_1 and V_2 . Lattice strains are non-linear in both crystallographic directions with a maximum of 3.14 % and -1.45 % for V_1 , while V_2 follows a similar trend. The 2: -1 ratio along the c- and a-axis, respectively, of the stress-induced lattice strains reflects the ferroelastic order parameter of tetragonal martensite such that the volume strain is zero, which is characteristic for shape memory behavior. Furthermore, the total lattice strain of V_1 and V_2 also shows a non-linear behavior with a maximum lattice strain of 5 %. However, a small lattice strain difference between loading and unloading was detected for both variants in the order of 0.23 % and 0.25 %. This hysteretic offset is attributed to non-elastic mechanisms during deformation and might be attributed to plastic deformation, detwinning or additional twinning modes to accommodate the deformation. However, plastic deformation of the material can be excluded due to the fully reversible transformation without residual strain to the original austenite state. Furthermore, the volume ratio of both martensite variants remains nearly constant. Hence, the occurrence of detwinning and the activation of additional twinning modes as a potential explanation for the small stress hysteresis width can be excluded as well. Consequently, a stable functional transformation behavior in the Co-Ni-Ga single crystal without deteriorating deformation mechanisms prevails up to the order of 11 %. The stress-induced martensitic phase is able to

withstand about 5 % elastic strain which significantly increases the overall deformation capability of this alloy system. Moreover, the absence of a suitable slip system seems to promote this excellent behavior. This will open up new possibilities for use of Co-Ni-Ga in high-strain applications. However, further studies focusing on role of temperature and cyclic stability will have to be conducted in future.

Aging heat treatment of solution-annealed $\text{Co}_{49}\text{Ni}_{21}\text{Ga}_{30}$ single crystals trigger the formation of γ' -nanoprecipitates in the austenitic phase with significant impact on the stress-induced martensite morphology, domain variant selection and functional properties. In [001] orientation under compressional load the single crystalline $\text{Co}_{49}\text{Ni}_{21}\text{Ga}_{30}$ in the solution-annealed (precipitate-free) condition is characterized by the formation of a dominant martensite plate and lamellar martensite plates between the arrangement of one set of few well-defined parallel habit planes. The parallel habit plane interfaces in the precipitate-free specimen feature the same crystallographic orientation with respect to the loading direction (cf. Fig. 7.7a). Each martensite plate comprises two twin related domain variants that form one correspondent variant pair (CVP). Aging of solution-annealed Co-Ni-Ga for 1 h at 350 °C produces spheroidal γ' precipitates (~5 nm sized) that trigger a complex multi-variant microstructure of stress-induced martensite under compressional load which is characterized by a dominant martensite plate and numerous lamellar martensite plates between two sets of differently oriented parallel habit planes (cf. Fig. 7.7c). In the aged condition the internally twinned stress-induced martensite morphology comprises multiple domain variants that form two sets of correspondent variant pairs (CVPs) as schematically illustrated in Fig. 8.1. The formation of two CVPs is based on the Bain-correspondence variants (BCVs). In the cubic to tetragonal transformation three possible Bain-correspondence variants BCV_1 , BCV_2 and BCV_3 (BCV_3 is not shown) evolve, each with the four-fold (c-axis) axis along on of the cubic austenite axis. Bain-correspondence variants BCV_1 and BCV_2 are favored with their c-axis perpendicular to the [001] compressive load direction. BCV_3 with the c-axis parallel to the compressive load direction is suppressed. Martensite domain variant orientations are derived from the stress-free intergrowth of two BCVs. This necessitates a rotation of the domain variants in relation to the initial orientation of the BCVs. Correspondingly, twinning of the pairs BCV_1 and BCV_2 is possible along a stress-free twin plane of the form $\{110\}$. In the aged specimen twinning of the domain variants V_1/V_2 and V_3/V_4 leads to the formation of two correspondent variant pairs (CVPs), i.e. CVP_1 and CVP_2 , respectively. This phenomenon is attributed to strong coherency stress fields in the matrix due to the formation of spheroidal γ' precipitates. Such kind of

microstructures obtained during stress-induced martensitic transformations with significant variant-variant interactions have been proposed to increase the stress hysteresis width and reduce transformation recoverability.

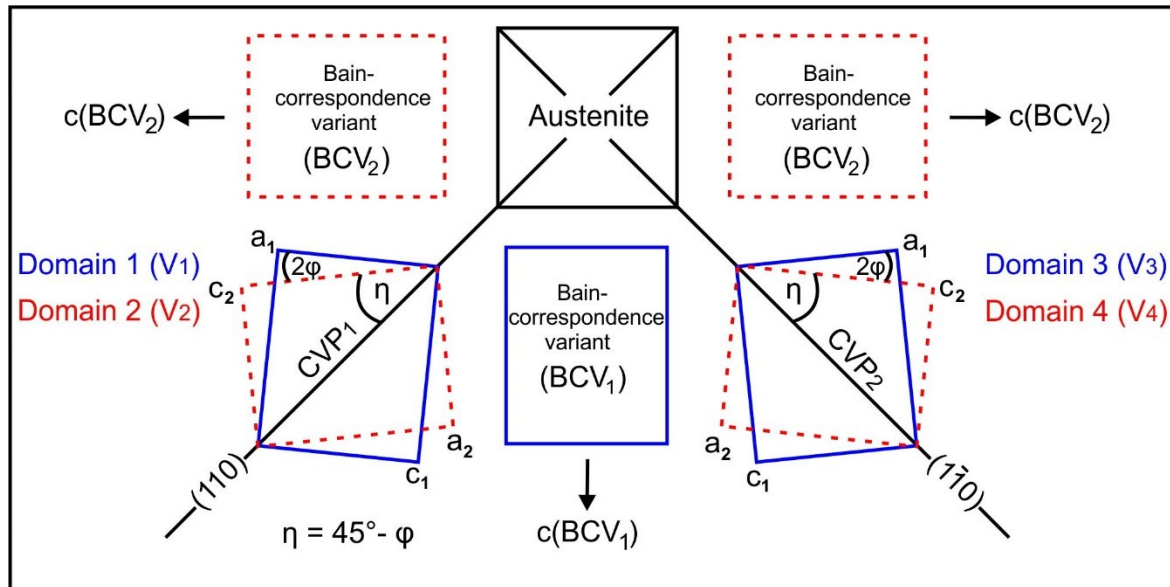


Fig. 8.1: Schematic representation of correspondent variant pair (CVP) formation based on the Bain-correspondence variants (BCVs). BCV_3 with the c -axis parallel to the compressive load direction (perpendicular to BCV_1 and BCV_2) is not shown. CVP_1 and CVP_2 represent twinning of the domain variants V_1/V_2 and V_3/V_4 of, respectively.

However, under tensile load substantial microstructural differences in stress-induced martensite were uncovered comparing three investigated conditions (i.e. as-grown, solution-annealed and aged) in [001] oriented $Co_{49}Ni_{21}Ga_{30}$ single crystals. Spheroidal γ' nanoprecipitates significantly reduce martensite lamellae thickness and increase the number of parallel habit planes within the shear band (cf. Fig. 7.16). In the aged specimen both microstructural effects are more pronounced as in case of the as-grown condition (cf. Fig. 7.11). In contrast, the solution-annealed condition is characterized by a dominant martensite plate and shear band with one martensite lamella and a single habit plane (cf. Fig. 7.13). The formation of γ' precipitates revealed only one set of parallel habit planes indicating the absence of variant-variant interactions upon tensile loading. One single domain variant of martensite (“fully detwinned”) is present throughout the whole transformation path for all three investigated conditions. Correspondingly, from three possible BCVs in the cubic to tetragonal transformation only BCV_3 with the c -axis parallel to the loading axis is favored. BCV_1 and BCV_2 with their c -axis transversal to the loading direction are suppressed. All specimens revealed a fully reversible SE

response. However, γ' precipitates significantly increase the stress hysteresis width ($\Delta\sigma$) as compared to the solution-annealed and as-grown condition. Most important, the impact of nanometric γ' precipitates upon aging treatment for 1 h at 350 °C is not necessarily associated with the formation of stress-induced multi-variant martensite microstructures under tensile loading. Hence, interactions between austenite-martensite phase boundaries and the γ' precipitates cause the significant increase of the stress hysteresis $\Delta\sigma$. This fact is attributed to the nanometric γ' precipitates which act as obstacles in the path of the moving austenite-martensite phase boundary in aged $\text{Co}_{49}\text{Ni}_{21}\text{Ga}_{30}$ single crystals. However, systematic investigations on the functional properties for envisaged damping applications need to be addressed in a follow up study. In particular further aging heat treatment carried out in the austenitic phase by variation of aging temperatures and -times are required to tailor the size and morphology of γ' precipitates and their influence on the superelastic material behavior.

9 References

- Besseghini, S., Villa, E., and Tuissi, A. (1999) Ni-Ti-Hf shape memory alloy: Effect of aging and thermal cycling. *Materials Science and Engineering A*, 273–275, 390–394.
- Bhattacharya (2003) *Microstructure of Martensite - Why it forms and how it gives rise to the shape-memory effect*, 288 p. Oxford University Press.
- Bowles, J.S., and Mackenzie, J.K. (1954) The crystallography of martensite transformations I. *Acta Metallurgica*, 2, 129–137.
- Buehler, W.J., Gilfrich, J. V., and Wiley, R.C. (1963) Effect of Low-Temperature Phase Changes on the Mechanical Properties of Alloys near Composition TiNi. *Journal of Applied Physics*, 34, 1475–1477.
- Cesari, E., Pons, J., and Chandrasekaran, M. (1994) The influence of γ precipitates on the martensitic transformation and related effects in Cu-based shape memory alloys. *Transactions Of The Materials Research Society Japan*, 18B, 903–909.
- Chernenko, V.A., Pons, J., Cesari, E., and Zasimchuk, I.K. (2004) Transformation behaviour and martensite stabilization in the ferromagnetic Co-Ni-Ga Heusler alloy. *Scripta Materialia*, 50, 225–229.
- Chernenko, V.A., Besseghini, S., Villa, E., Gambardella, A., and Pérez-Landazabal, J.I. (2007) Elastic and superelastic properties of Co₄₉Ni₂₂Ga₂₉ single crystal. *Applied Physics Letters*, 90, 201914.
- Chumlyakov, Y.I., Kireeva, I. V., Panchenko, E.Y., Timofeeva, E.E., Pobedennaya, Z. V., Chusov, S. V., Karaman, I., Maier, H., Cesari, E., and Kirillov, V.A. (2008) High-temperature superelasticity in CoNiGa, CoNiAl, NiFeGa, and TiNi monocrystals. *Russian Physics Journal*, 51, 1016–1036.
- Chumlyakov, Y.I., Kireeva, I. V., Panchenko, E.Y., Kirillov, V.A., Timofeeva, E.E., Kretinina, I. V., Danil'son, Y.N., Karaman, I., Maier, H., and Cesari, E. (2012) Thermoelastic martensitic transformations in single crystals with disperse particles. *Russian Physics Journal*, 54, 937–950.
- Dadda, J., Maier, H.J.J., Karaman, I., Karaca, H.E.E., and Chumlyakov, Y.I.I. (2006)

- Pseudoelasticity at elevated temperatures in [001] oriented Co₄₉Ni₂₁Ga₃₀ single crystals under compression. *Scripta Materialia*, 55, 663–666.
- Dadda, J., Canadinc, D., Maier, H.J., and Karaman, I. (2007) Stress – strain – temperature behaviour of [001] single crystals of Co₄₉ Ni₂₁ Ga₃₀ ferromagnetic shape memory alloy under compression. *Philosophy Magazine*, 87, 2313–2322.
- Dadda, J., Maier, H.J., Niklasch, D., Karaman, I., Karaca, H.E., and Chumlyakov, Y.I. (2008) Pseudoelasticity and Cyclic Stability in Co₄₉Ni₂₁Ga₃₀ Shape-Memory Alloy Single Crystals at Ambient Temperature. *Metallurgical and Materials Transactions A*, 39, 2026–2039.
- Dadda, J., Maier, H.J., Karaman, I., and Chumlyakov, Y.I. (2009) Cyclic deformation and austenite stabilization in Co₃₅Ni₃₅Al₃₀ single crystalline high-temperature shape memory alloys. *Acta Materialia*, 57, 6123–6134.
- Dadda, J., Maier, H.J., Karaman, I., and Chumlyakov, Y. (2010) High-temperature in-situ microscopy during stress-induced phase transformations in Co₄₉Ni₂₁Ga₃₀ shape memory alloy single crystals. *International Journal of Materials Research*, 101, 1503–1513.
- Dogan, E., Karaman, I., Chumlyakov, Y.I., and Luo, Z.P. (2011) Microstructure and martensitic transformation characteristics of CoNiGa high temperature shape memory alloys. *Acta Materialia*, 59, 1168–1183.
- Duerig, T., Pelton, A., and Stöckel, D. (1999) An overview of nitinol medical applications. *Materials Science and Engineering*, 275, 149–160.
- Es-Souni, Mohammed, Es-Souni, Martha, and Fischer-Brandies, H. (2005) Assessing the biocompatibility of NiTi shape memory alloys used for medical applications. *Analytical and Bioanalytical Chemistry*, 381, 557–567.
- Evirgen, A., Karaman, I., Santamarta, R., Pons, J., and Noebe, R.D. (2015) Microstructural characterization and shape memory characteristics of the Ni_{50.3}Ti_{34.7}Hf₁₅ shape memory alloy. *Acta Materialia*, 83, 48–60.
- Firstov, G.S., Van Humbeeck, J., and Koval, Y.N. (2004) High-temperature shape memory alloys Some recent developments. *Materials Science and Engineering A*, 378, 2–10.

- Gall, K., and Maier, H.J. (2002) Cyclic deformation mechanisms in precipitated NiTi shape memory alloys. *Acta Materialia*, 50, 4643–4657.
- Gall, K., and Sehitoglu, H. (1999) Role of texture in tension-compression asymmetry in polycrystalline NiTi. *International journal of plasticity*, 15, 69–92.
- Gall, K., Sehitoglu, H., Chumlyakov, Y.I., Kireeva, I. V., and Maier, H.J. (1999) The influence of aging on critical transformation stress levels and martensite start temperatures in NiTi: Part I- Aged microstructure and micro-mechanical modeling. *Journal of Engineering Materials and Technology, Transactions of the ASME*, 121, 19–27.
- Gerstein, G., L'vov, V.A., Kosogor, A., and Maier, H.J. (2018) Internal pressure as a key thermodynamic factor to obtain high-temperature superelasticity of shape memory alloys. *Materials Letters*, 210, 252–254.
- Golberg, D., Xu, Y., Murakami, Y., Otsuka, K., Ueki, T., and Horikawa, H. (1995) High-temperature shape memory effect in Ti50Pd50-xNix (x = 10, 15, 20) alloys. *Materials Letters*, 22, 241–248.
- Hamilton, R.F., Sehitoglu, H., Chumlyakov, Y., and Maier, H.J. (2004) Stress dependence of the hysteresis in single crystal NiTi alloys. *Acta Materialia*, 52, 3383–3402.
- Hamilton, R.F., Sehitoglu, H., Efstathiou, C., Maier, H.J., Chumlyakov, Y., and Zhang, X.Y. (2005) Transformation of Co-Ni-Al single crystals in tension. *Scripta Materialia*, 53, 131–136.
- Hartl, D.J., and Lagoudas, D.C. (2007) Aerospace applications of shape memory alloys. *Proceedings of the Institution of Mechanical Engineers, Part G: Journal of Aerospace Engineering*, 221, 535–552.
- Hoelzel, M., Gan, W.M., Hofmann, M., Randau, C., Seidl, G., Jüttner, P., and Schmahl, W.W. (2013) Rotatable multifunctional load frames for neutron diffractometers at FRM II - Design, specifications and applications. *Nuclear Instruments and Methods in Physics Research, Section A: Accelerators, Spectrometers, Detectors and Associated Equipment*, 711, 101–105.
- Hofmann, M., Schneider, R., Seidl, G.A., Rebelo-Kornmeier, J., Wimpory, R.C., Garbe, U.,

- and Brokmeier, H.G. (2006) The new materials science diffractometer STRESS-SPEC at FRM-II. *Physica B: Condensed Matter*, 385–386, 1035–1037.
- Hsieh, S.F., and Wu, S.K. (1998) A Study on Ternary Ti-rich TiNiZr Shape Memory Alloys. *Materials Characterization*, 41, 151–162.
- Ishida, K., Kainuma, R., Ueno, N., and Nishizawa, T. (1991) Ductility enhancement in NiAl (B2)-Base Alloys by Microstructural Control. *Metallurgical transactions. A*, 22A, 441–446.
- Kadletz, P.M., Krooß, P., Chumlyakov, Y.I., Gutmann, M.J., Schmahl, W.W., Maier, H.J., and Niendorf, T. (2015) Martensite stabilization in shape memory alloys - Experimental evidence for short-range ordering. *Materials Letters*, 159, 16–19.
- Kainuma, R., Ise, M., Jia, C.C., Ohtani, H., and Ishida, K. (1996) Phase equilibria and microstructural control in the Ni-Co-Al system. *Intermetallics*, 4, 151–158.
- Karaca, H.E., Karaman, I., Lagoudas, D.C., Maier, H.J., and Chumlyakov, Y.I. (2003) Recoverable stress-induced martensitic transformation in a ferromagnetic CoNiAl alloy. *Scripta Materialia*, 49, 831–836.
- Karsten, E., Gerstein, G., Golovko, O., Dalinger, A., Lauhoff, C., Krooss, P., Niendorf, T., Samsonenko, A., and Maier, H.J. (2019) Tailoring the Microstructure in Polycrystalline Co–Ni–Ga High-Temperature Shape Memory Alloys by Hot Extrusion. *Shape Memory and Superelasticity*, 5, 84–94.
- Kaufman, L., and Cohen, M. (1958) Thermodynamics and kinetics of martensitic transformations. *Progress in Metal Physics*, 7, 165–246.
- Keen, D.A., Gutmann, M.J., and Wilson, C.C. (2006) SXD - The single-crystal diffractometer at the ISIS spallation neutron source. *Journal of Applied Crystallography*, 39, 714–722.
- Khalil-Allafi, J., Eggeler, G., Schmahl, W.W., and Sheptyakov, D. (2006) Quantitative phase analysis in microstructures which display multiple step martensitic transformations in Ni-rich NiTi shape memory alloys. *Materials Science and Engineering A*, 438–440, 593–596.
- Kimura, Y., Miura, S., Suzuki, T., and Mishima, Y. (1994) Microstructure and Mechanical Properties of Two-Phase Alloys Based on the B2-Type Intermetallic Compound CoAl in

- the Co-Al-Ni Ternary System. *Materials Transactions*, 35, 800–807.
- Kireeva, I.V., Pons, J., Picornell, C., Chumlyakov, Y.I., Cesari, E., and Kretinina, I.V. (2013) Influence of γ' nanometric particles on martensitic transformation and twinning structure of L10 martensite in Co-Ni-Ga ferromagnetic shape memory single crystals. *Intermetallics*, 35, 60–66.
- Kireeva, I.V., Picornell, C., Pons, J., Kretinina, I.V., Chumlyakov, Y.I., and Cesari, E. (2014) Effect of oriented γ' precipitates on shape memory effect and superelasticity in Co-Ni-Ga single crystals. *Acta Materialia*, 68, 127–139.
- Kireeva, I. V., Pobedennaya, Z. V., Chumlyakov, Y.I., Pons, J., Cesari, E., and Karaman, I. (2009) Effect of orientation on the high-temperature superelasticity in Co₄₉Ni₂₁Ga₃₀ single crystals. *Technical Physics Letters*, 35, 186–189.
- Kretinina, I. V., Kuts, O.A., Kuksgauzen, D.A., Poklonov, V. V., Pobedennaya, Z. V., and Platonova, Y.N. (2015) Influence of particles on the functional properties of single crystals of high-strength ferromagnetic alloys. *IOP Conference Series: Materials Science and Engineering*, 71.
- Krooß, P., Somsen, C., Niendorf, T., Schaper, M., Karaman, I., Chumlyakov, Y., Eggeler, G., and Maier, H.J. (2014) Cyclic degradation mechanisms in aged FeNiCoAlTa shape memory single crystals. *Acta Materialia*, 79, 126–137.
- Krooß, P., Niendorf, T., Kadletz, P.M., Somsen, C., Gutmann, M.J., Chumlyakov, Y.I., Schmahl, W.W., Eggeler, G., and Maier, H.J. (2015) Functional Fatigue and Tension–Compression Asymmetry in [001]-Oriented Co₄₉Ni₂₁Ga₃₀ High-Temperature Shape Memory Alloy Single Crystals. *Shape Memory and Superelasticity*, 1, 6–17.
- Krooß, P., Kadletz, P.M., Somsen, C., Gutmann, M.J., Chumlyakov, Y.I., Schmahl, W.W., Maier, H.J., and Niendorf, T. (2016) Cyclic Degradation of Co₄₉Ni₂₁Ga₃₀ High-Temperature Shape Memory Alloy: On the Roles of Dislocation Activity and Chemical Order. *Shape Memory and Superelasticity*, 2, 37–49.
- Kustov, S., Pons, J., Cesari, E., and Van Humbeeck, J. (2004) Pinning-induced stabilization of martensite Part I . Stabilization due to static pinning of interfaces, 52, 3075–3081.

- Lagoudas, D.C. (2008) *Shape Memory Alloys: Modeling and Engineering Applications*, 435 p. (D.C. Lagoudas, Ed.). Springer, New York.
- Laplanche, G., Birk, T., Schneider, S., Frenzel, J., and Eggeler, G. (2017) Effect of temperature and texture on the reorientation of martensite variants in NiTi shape memory alloys. *Acta Materialia*, 127, 143–152.
- Lauhoff, C., Krooß, P., Langenkämper, D., Somsen, C., Eggeler, G., Kireeva, I., Chumlyakov, Y.I., and Niendorf, T. (2018) Martensite aging in $\langle 0\ 0\ 1 \rangle$ -oriented Co₄₉Ni₂₁Ga₃₀ single crystals in tension. *Functional Materials Letters*, 11, 15–18.
- Lauhoff, C., Reul, A., Langenkämper, D., Krooß, P., Somsen, C., Gutmann, M.J., Kireeva, I., Chumlyakov, Y.I., Schmahl, W.W., and Niendorf, T. (2019a) Effect of nanometric γ' -particles on the stress-induced martensitic transformation in $\langle 001 \rangle$ -oriented Co₄₉Ni₂₁Ga₃₀ shape memory alloy single crystals. *Scripta Materialia*, 168, 42–46.
- Lauhoff, C., Vollmer, M., Krooß, P., Kireeva, I., Chumlyakov, Y.I., and Niendorf, T. (2019b) Pathways Towards Grain Boundary Engineering for Improved Structural Performance in Polycrystalline Co–Ni–Ga Shape Memory Alloys. *Shape Memory and Superelasticity*, 5, 73–83.
- Lauhoff, C., Fischer, A., Sobrero, C., Liehr, A., Krooß, P., Brenne, F., Richter, J., Kahlert, M., Böhm, S., and Niendorf, T. (2020a) Additive Manufacturing of Co-Ni-Ga High-Temperature Shape Memory Alloy: Processability and Phase Transformation Behavior. *Metallurgical and Materials Transactions A: Physical Metallurgy and Materials Science*, 51, 1056–1061.
- Lauhoff, C., Sommer, N., Vollmer, M., Mienert, G., Krooß, P., Böhm, S., and Niendorf, T. (2020b) Excellent superelasticity in a Co-Ni-Ga high-temperature shape memory alloy processed by directed energy deposition. *Materials Research Letters*, 8, 314–320.
- Liu, J., Xie, H., Huo, Y., Zheng, H., and Li, J. (2006) Microstructure evolution in CoNiGa shape memory alloys. *J. Alloys Compd.*, 420, 145–157.
- Ma, J., Karaman, I., and Noebe, R.D. (2010) High temperature shape memory alloys. *International Materials Reviews*, 55, 257–315.

- Mackenzie, J.K., and Bowles, J.S. (1954) The crystallography of martensite transformations II. *Acta Metallurgica*, 2, 138–147.
- Martin, J.W. (1980) *Micromechanisms in particle-hardened alloys*, 1st ed., 201 p. Cambridge University Press, Cambridge.
- Melton, K.N., and Mercier, O. (1979) The effect of the martensitic phase transformation on the low cycle fatigue behaviour of polycrystalline NiTi and CuZnAl alloys. *Materials Science and Engineering*, 40, 81–87.
- Miyazaki, S., Otsuka, K., and Suzuki, Y. (1981) Transformation pseudoelasticity in NiTi. *Scripta Metallurgica*, 15, 287–292.
- Miyazaki, S., Ohmi, Y., Otsuka, K., and Suzuki, Y. (1982) Characteristics Of Deformation And Transformation Pseudoelasticity In Ti-Ni Alloys. *Journal de Physique (Paris), Colloque*, 43, 255–260.
- Miyazaki, S., Kimura, S., Takei, F., Miura, T., Otsuka, K., and Suzuki, Y. (1983) Shape Memory Effect and Pseudoelasticity in a Ti-Ni Single Crystal. *Scripta Metallurgica*, 17, 1057–1062.
- Miyazaki, S., Kimura, S., Otsuka, K., and Suzuki, Y. (1984) The habit plane and transformation strains associated with the martensitic transformation in Ti-Ni single crystals. *Scripta Metallurgica*, 18, 883–888.
- Miyazaki, S., Imai, T., Igo, Y., and Otsuka, K. (1986) Effect of Cyclic Deformation on the Pseudoelasticity Characteristics of Ti-Ni Alloys. *Metallurgical transactions. A, Physical metallurgy and materials science*, 17 A, 115–120.
- Miyazaki, S., Kohiyama, Y., Otsuka, K., and Duerig, T.W. (1991) Effects of Several Factors on the Ductility of the Ti-Ni Alloy. *Materials Science Forum*, 56–58, 765–770.
- Mohd Jani, J., Leary, M., Subic, A., and Gibson, M.A. (2014) A review of shape memory alloy research, applications and opportunities. *Materials and Design*, 56, 1078–1113.
- Molnár, P., Šittner, P., Novák, V., and Lukáš, P. (2008) Twinning processes in Cu-Al-Ni martensite single crystals investigated by neutron single crystal diffraction method. *Materials Science and Engineering A*, 481–482, 513–517.

- Monroe, J.A., Karaman, I., Karaca, H.E., Chumlyakov, Y.I., and Maier, H.J. (2010) High-temperature superelasticity and competing microstructural mechanisms in Co₄₉Ni₂₁Ga₃₀ shape memory alloy single crystals under tension. *Scripta Materialia*, 62, 368–371.
- Niendorf, T., Dadda, J., Lackmann, J., Monroe, J.A., Karaman, I., Panchenko, E., Karaca, H.E., and Maier, H.J. (2013) Tension - Compression Asymmetry in Co₄₉Ni₂₁Ga₃₀ High-Temperature Shape Memory Alloy Single Crystals. *Materials Science Forum*, 738–739, 82–86.
- Niendorf, T., Krooß, P., Somsen, C., Eggeler, G., Chumlyakov, Y.I., and Maier, H.J. (2015) Martensite aging - Avenue to new high temperature shape memory alloys. *Acta Materialia*, 89, 298–304.
- Niendorf, T., Lauhoff, C., Karsten, E., Gerstein, G., Liehr, A., Krooß, P., and Maier, H.J. (2019) Direct microstructure design by hot extrusion – High-temperature shape memory alloys with bamboo-like microstructure. *Scripta Materialia*, 162, 127–131.
- Niklasch, D., Dadda, J., Maier, H.J., and Karaman, I. (2008) Magneto-microstructural coupling during stress-induced phase transformation in Co₄₉Ni₂₁Ga₃₀ ferromagnetic shape memory alloy single crystals. *Journal of Materials Science*, 43, 6890–6901.
- Nishida, M., Wayman, C.M., and Honma, T. (1986) Precipitation processes in near-equiatomic TiNi shape memory alloys. *Metallurgical Transactions A*, 17, 1505–1515.
- Noebe, R., Gaydosch, D., Padula II, S., Garg, A., Biles, T., and Nathal, M. (2005) Properties and potential of two (Ni,Pt)Ti alloys for use as high-temperature actuator materials. *Smart Structures and Materials 2005: Active Materials: Behavior and Mechanics*, 5761, 364.
- Oikawa, K., Ota, T., Gejima, F., Ohmori, T., Kainuma, R., and Ishida, K. (2001) Phase Equilibria and Phase Transformations in New B2-type Ferromagnetic Shape Memory Alloys of Co-Ni-Ga and Co-Ni-Al Systems. *Materials Transactions*, 42, 2472–2475.
- Oikawa, K., Ota, T., Imano, Y., Omori, T., Kainuma, R., and Ishida, K. (2006) Phase equilibria and phase transformation of Co-Ni-Ga ferromagnetic shape memory alloy system. *Journal of Phase Equilibria and Diffusion*, 27, 75–82.
- Otsuka, K., and Ren, X. (2005) Physical metallurgy of Ti-Ni-based shape memory alloys.

- Progress in Materials Science, 50, 511–678.
- Otsuka, K., and Wayman, C.M. (1999) Shape memory materials, 147 p. Cambridge University Press, Cambridge.
- Padula, S., Bigelow, G., Noebe, R., Gaydos, D., and Garg, A. (2008) Challenges and progress in the development of high-temperature shape memory alloys based on nitix compositions for high-force actuator applications. SMST-2006 - Proceedings of the International Conference on Shape Memory and Superelastic Technologies, 787–802.
- Picornell, C., Pons, J., and Cesari, E. (2001) Stabilisation of martensite by applying compressive stress in Cu-Al-Ni single crystals. Acta Materialia, 49, 4221–4230.
- Picornell, C., Pons, J., Cesari, E., Chumlyakov, Y.I., and Dutkiewicz, J. (2009) Effect of Aging under Compressive Stress along [100] in Co-Ni-Ga Single Crystals. Functional Materials Letters, 02, 83–86.
- Pons, J., Sade, M., Lovey, F.C., and Cesari, E. (1993) Pseudoelastic cycling and two-way shape memory effect in β Cu-Zn-Al alloys with γ -precipitates. Materials Transactions, JIM, 34, 888–894.
- Randau, C., Garbe, U., and Brokmeier, H.G. (2011) StressTextureCalculator: A software tool to extract texture, strain and microstructure information from area-detector measurements. Journal of Applied Crystallography, 44, 641–646.
- Reul, A., Lauhoff, C., Krooß, P., Gutmann, M.J., Kadletz, P.M., Chumlyakov, Y.I., Niendorf, T., and Schmahl, W.W. (2018) In Situ Neutron Diffraction Analyzing Stress-Induced Phase Transformation and Martensite Elasticity in [001]-Oriented Co₄₉Ni₂₁Ga₃₀ Shape Memory Alloy Single Crystals. Shape Memory and Superelasticity, 4, 61–69.
- Rondelli, G. (1996) Corrosion resistance tests on NiTi shape memory alloy. Biomaterials, 17, 2003–2008.
- Salzbrenner, R.J., and Cohen, M. (1979) On the thermodynamics of thermoelastic martensitic transformations. Acta Metallurgica, 27, 739–748.
- Schäfer, A. (2012) Werkstoffwissenschaftliche Untersuchung zur Bildung und Wachstum von Martensit in NiTi-Formgedächtnislegierungen unter Spannung. Ruhr-Universität Bochum.

- Sehitoglu, H., Karaman, I., Anderson, R., Zhang, X., Gall, K., Maier, H.J., and Chumlyakov, Y. (2000) Compressive response of NiTi single crystals. *Acta Materialia*, 48, 3311–3326.
- Sehitoglu, H., Patriarca, L., and Wu, Y. (2017) Shape memory strains and temperatures in the extreme. *Current Opinion in Solid State and Materials Science*, 21, 113–120.
- Shaw, J.A., and Kyriakides, S. (1995) Thermomechanical aspects of NiTi. *Journal of the Mechanics and Physics of Solids*, 43, 1243–1281.
- Shimizu, S., Xu, Y., Okunishi, E., Tanaka, S., Otsuka, K., and Mitose, K. (1998) Improvement of shape memory characteristics by precipitation-hardening of Ti-Pd-Ni alloys. *Materials Letters*, 34, 23–29.
- Stebner, A.P., Bigelow, G.S., Yang, J., Shukla, D.P., Saghayan, S.M., Rogers, R., Garg, A., Karaca, H.E., Chumlyakov, Y., Bhattacharya, K., and others (2014) Transformation strains and temperatures of a nickel-titanium-hafnium high temperature shape memory alloy. *Acta Materialia*, 76, 40–53.
- Strnadel, B., Ohashi, S., Ohtsuka, H., Miyazaki, S., and Ishihara, T. (1995) Effect of mechanical cycling on the pseudoelasticity characteristics of TiNi and TiNiCu alloys. *Materials Science and Engineering A*, 203, 187–196.
- Tanaka, Y., Himuro, Y., Kainuma, R., Sutou, Y., Omori, T., and Ishida, K. (2010) Ferrous polycrystalline shape-memory alloy showing huge superelasticity. *Science*, 327, 1488–1490.
- Van Humbeeck, J. (2003) Damping capacity of thermoelastic martensite in shape memory alloys. *Journal of Alloys and Compounds*, 355, 58–64.
- Vollmer, M., Krooß, P., Segel, C., Weidner, A., Paulsen, A., Frenzel, J., Schaper, M., Eggeler, G., Maier, H.J., and Niendorf, T. (2015) Damage evolution in pseudoelastic polycrystalline Co-Ni-Ga high-temperature shape memory alloys. *Journal of Alloys and Compounds*, 633, 288–295.

10 Appendix

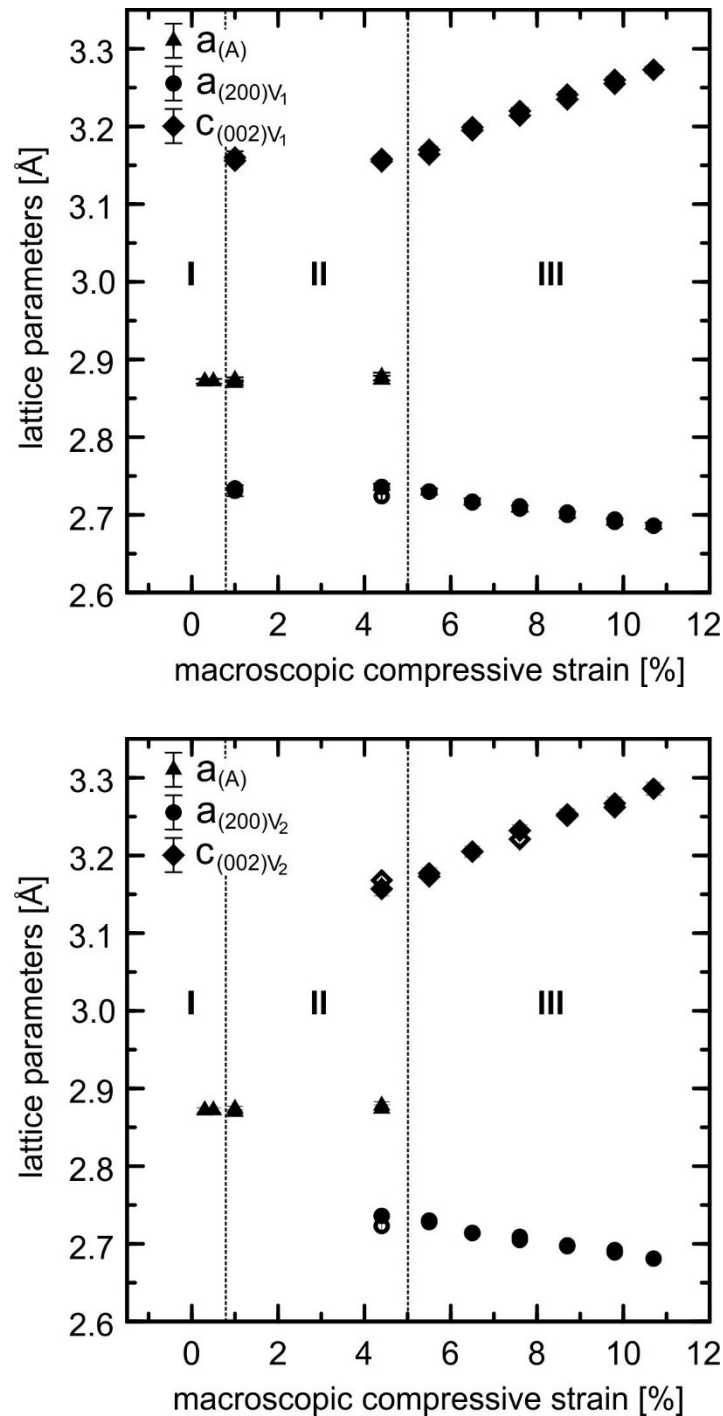


Figure A1: Lattice parameters as a function of macroscopic compressive strain of the [001]-oriented $\text{Co}_{49}\text{Ni}_{21}\text{Ga}_{30}$ single crystal in the as-grown condition (cf. Fig. 7.1j). The elastic austenite region, stress-plateau and elastic martensite region is referred to as region I, region II and region III, respectively. A: austenite, V_1 (top) and V_2 (bottom): martensite. Note, closed and open symbols represent the forward and reverse transformation, respectively. The limits of error are within the size of the data points.

$a_{(A)}$ [Å]	$a_{(200)V1}$ [Å]	$c_{(002)V1}$ [Å]	$a_{(200)V2}$ [Å]	$c_{(002)V2}$ [Å]	strain [%]	stress [MPa]
2.872(3)	-	-	-	-	0.3	18.7
2.872(3)	-	-	-	-	0.5	39.6
2.874(3)	2.731(7)	3.160(8)	-	-	1.0	39.7
2.877(5)	2.736(4)	3.158(4)	2.736(8)	3.157(9)	4.4	43.3
-	2.730(4)	3.170(4)	2.730(5)	3.177(7)	5.5	128.3
-	2.717(4)	3.199(4)	2.714(5)	3.205(7)	6.5	294.4
-	2.708(4)	3.220(4)	2.705(5)	3.232(7)	7.6	476.4
-	2.700(4)	3.241(4)	2.697(5)	3.253(7)	8.7	672.1
-	2.691(4)	3.260(4)	2.689(6)	3.267(8)	9.8	872.2
-	2.686(4)	3.273(4)	2.681(5)	3.286(8)	10.7	1029.0
-	2.694(4)	3.255(4)	2.692(4)	3.262(7)	9.8	790.1
-	2.703(4)	3.235(4)	2.698(4)	3.251(7)	8.7	575.1
-	2.711(4)	3.214(4)	2.709(5)	3.221(8)	7.6	382.5
-	2.716(4)	3.195(4)	2.714(5)	3.205(7)	6.5	217.7
-	2.730(4)	3.164(4)	2.728(5)	3.173(8)	5.5	77.1
2.874(5)	2.724(4)	3.155(3)	2.723(5)	3.168(8)	4.4	10.1
2.870(3)	2.734(6)	3.156(9)	-	-	1.0	12.7
2.872(3)	-	-	-	-	0.3	6.6

Table A1: Refinement results obtained from neutron diffraction data of the [001]-oriented Co₄₉Ni₂₁Ga₃₀ single crystal in the as-grown condition. Lattice parameters for austenite (A) and martensite (V₁ and V₂) at each load stage on the stress-strain curve (cf. Fig. 7.1j).

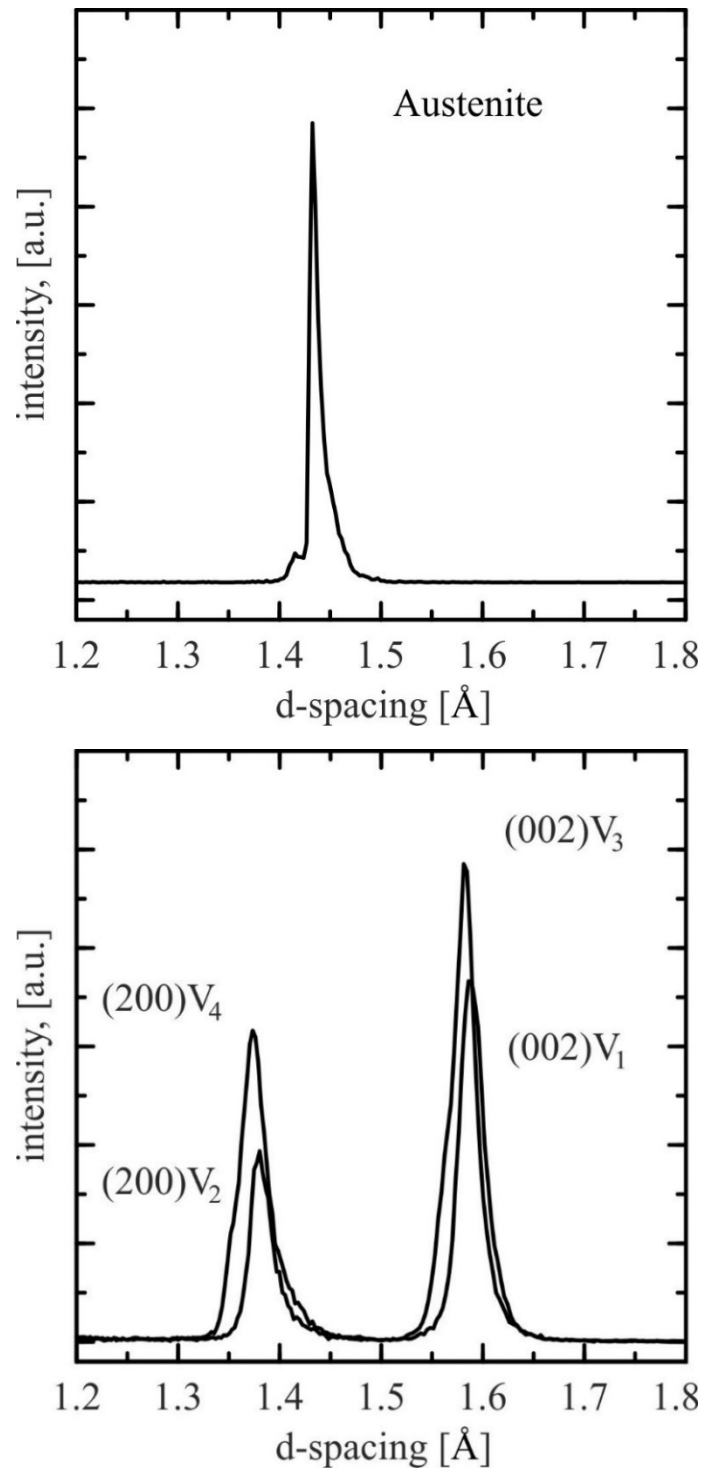


Figure A2: Diffraction intensity as a function of d-spacing obtained at zero strain (top, c.f. Fig. 7.8 a) and - 5 % macroscopically applied compressive strain (bottom, c.f. Fig. 7.8 c) of a [001]-oriented $Co_{49}Ni_{21}Ga_{30}$ single crystal in the aged (1 h/350 °C) condition. The in situ neutron diffraction experiment was performed at 100 °C. A: austenite, V_1 , V_2 , V_3 and V_4 : martensite. The martensite domains V_1/V_2 and V_3/V_4 form a correspondent variant pair (CVP), respectively.

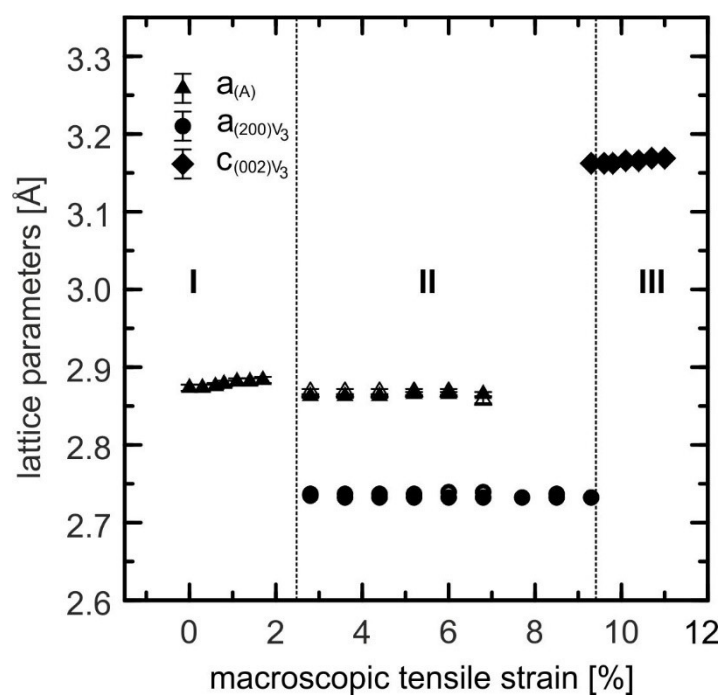


Figure A3: Lattice parameters as a function of macroscopic tensile strain of the [001]-oriented $\text{Co}_{49}\text{Ni}_{21}\text{Ga}_{30}$ single crystal in the as-grown condition (cf Fig. 7.9a). The elastic austenite region, stress-plateau and elastic martensite region is referred to as region I, region II and region III, respectively. A: austenite, V_3 : martensite. Note, closed and open symbols represent the forward and reverse transformation, respectively. The limits of error are within the size of the data points.

$a_{(A)}$ [Å]	$a_{(200)V_3}$ [Å]	$c_{(002)V_3}$ [Å]	tensile strain [%]	tensile stress [Mpa]	χ [°]
2.874(4)	-	-	0.0	17.4	90
2.874(4)	-	-	0.3	40.4	90
2.876(4)	-	-	0.6	60.6	90
2.879(4)	-	-	0.8	73.3	90
2.882(4)	-	-	1.1	91.5	90
2.882(4)	-	-	1.4	107.1	90
2.884(4)	-	-	1.7	119.8	90
2.863(3)	2.735(1)	-	2.8	90.3	0
2.863(3)	2.733(1)	-	3.6	89.2	0
2.863(3)	2.733(1)	-	4.4	87.7	0
2.866(3)	2.733(1)	-	5.2	87.7	0
2.866(3)	2.733(1)	-	6.0	88.3	0
2.866(3)	2.733(1)	-	6.8	89.9	0
-	2.733(1)	-	7.7	87.4	0
-	2.733(1)	-	8.5	86.2	0
-	2.733(1)	3.163(3)	9.3	85.6	0/90
-	-	3.163(3)	9.6	88.3	90
-	-	3.163(3)	9.8	91.5	90
-	-	3.166(3)	10.1	95.4	90
-	-	3.166(3)	10.4	99.3	90
-	-	3.169(3)	10.7	104.3	90
-	-	3.169(3)	11.0	109.8	90
-	2.737(1)	-	8.5	71.4	0
2.858(4)	2.740(1)	-	6.8	77.6	0
2.869(4)	2.740(1)	-	6.0	76.6	0
2.869(4)	2.737(1)	-	5.2	74.2	0
2.869(4)	2.737(1)	-	4.4	74.9	0
2.869(4)	2.737(1)	-	3.6	73.8	0
2.869(4)	2.737(1)	-	2.8	25.2	0

Table A2: Refinement results obtained from neutron diffraction data of the [001]-oriented $Co_{49}Ni_{21}Ga_{30}$ single crystal in the as-grown condition. Lattice parameters for austenite (A) and martensite (V_3) at each load stage on the stress-strain curve (cf. Fig. 7.9a). The orientation of the load axis (cf. Fig. 6.4) with respect to the monochromatic incident beam was $\chi = 0^\circ$ (load axis vertical to the scattering plane) and $\chi = 90^\circ$ (load axis in the scattering plane).

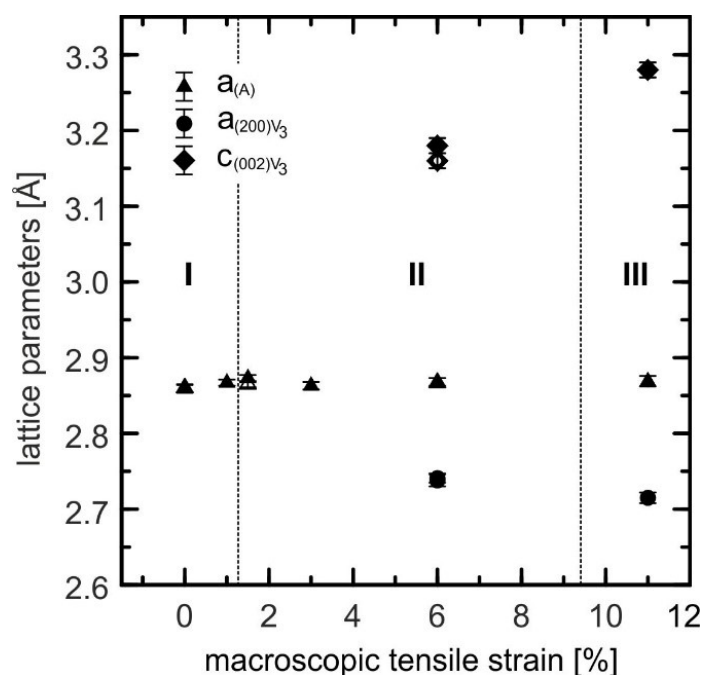


Figure A4: Lattice parameters as a function of macroscopic tensile strain of the [001]-oriented $\text{Co}_{49}\text{Ni}_{21}\text{Ga}_{30}$ single crystal in the solution-annealed condition (cf Fig. 7.9b). The elastic austenite region, stress-plateau and elastic martensite region is referred to as region I, region II and region III, respectively. A: austenite, V_3 : martensite

$a_{(A)}$ [Å]	$a_{(200)V_3}$ [Å]	$c_{(002)V_3}$ [Å]	tensile strain [%]	tensile stress [MPa]
2.859(5)	-	-	0.0	17.5
2.867(4)	-	-	1.0	93.3
2.873(4)	-	-	1.5	48.8
2.863(5)	-	-	3.0	49.1
2.868(5)	2.738(8)	3.178(14)	6.0	53.3
2.869(7)	2.715(7)	3.276(15)	11.0	59.2
2.867(6)	2.741(6)	3.160(11)	6.0	40.1
2.865(4)	-	-	1.5	31.7
2.860(5)	-	-	0.0	24.0

Table A3: Refinement results obtained from neutron diffraction data of the [001]-oriented $\text{Co}_{49}\text{Ni}_{21}\text{Ga}_{30}$ single crystal in the solution-annealed condition. Lattice parameters for austenite (A) and martensite (V_3) at each load stage on the stress-strain curve (cf Fig. 7.9b).

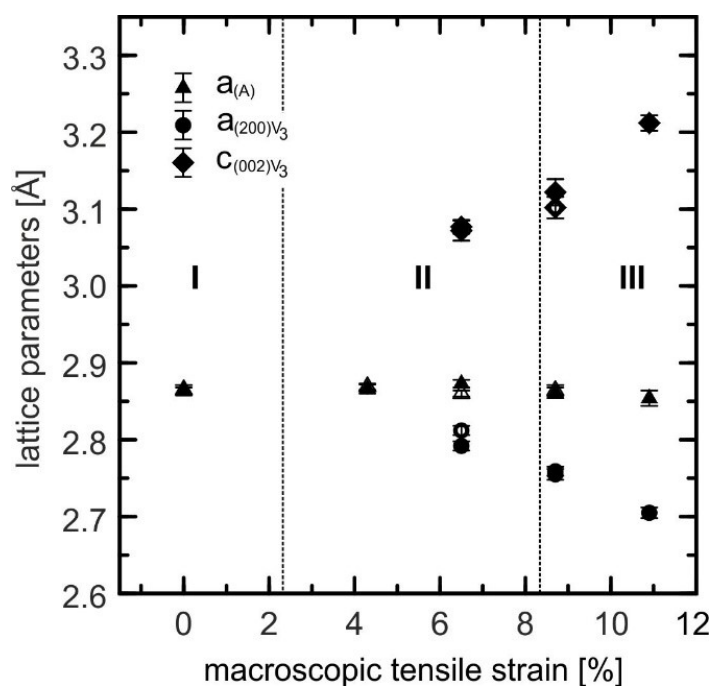


Figure A5: Lattice parameters as a function of macroscopic tensile strain of the [001]-oriented $Co_{49}Ni_{21}Ga_{30}$ single crystal in the aged (1 h/350 °C) condition (cf. Fig. 7.9c). The elastic austenite region, stress-plateau and elastic martensite region is referred to as region I, region II and region III, respectively. A: austenite, V_3 : martensite.

$a_{(A)}$ [Å]	$a_{(200)V_3}$ [Å]	$c_{(002)V_3}$ [Å]	tensile strain [%]	tensile stress [MPa]
2.863(5)	-	-	0.0	17.1
2.866(6)	-	-	4.3	87.2
2.873(5)	2.792(6)	3.071(13)	6.5	85.5
2.861(7)	2.755(7)	3.122(18)	8.7	85.9
2.854(10)	2.705(7)	3.212(11)	11.0	134.9
2.864(7)	2.759(6)	3.102(15)	8.7	51.9
2.860(4)	2.812(6)	3.077(9)	6.5	48.7
2.869(4)	-	-	4.3	50.4
2.865(6)	-	-	0.0	16.9

Table A4: Refinement results obtained from neutron diffraction data of the [001]-oriented $Co_{49}Ni_{21}Ga_{30}$ single crystal in the aged (1 h/350 °C) condition. Lattice parameters for austenite (A) and martensite (V_3) at each load stage on the stress-strain curve (cf. Fig. 7.9c).

Acknowledgements

Financial support by Deutsche Forschungsgemeinschaft (DFG) within the Research Unit Program “Hochtemperatur-Formgedächtnislegierungen” (Contract nos. SCHM930/13-2, NI1327/3-2, EG101/22-2 and SO505/2-2) and the Ministry of Science and Education of Russian Federation (State Task no. 16.6554.2017/6.7) is gratefully acknowledged.

I want to express my keen gratitude to my supervisor Prof. Dr. Wolfgang Schmahl who gave me the opportunity to work within the DFG research unit program *FOR1766*. I am deeply grateful for his valuable advices and support in the course of my thesis.

I want to thank the colleagues Prof. Dr. Thomas Niendorf, Philipp Krooß and Christian Lauhoff from the Institute of Materials Engineering (University of Kassel) for the outstanding collaboration, continuous support and helpfulness during the past years. My special thanks to Philipp Krooß, Christian Lauhoff and Peter Kadletz for the great time during beamtime, conferences and vacation.

I want to gratefully thank the staff of the beamlines SXD (ISIS neutron source, Oxfordshire) and STRESS-SPEC (FRM-II, Garching) for support and inspiration during the experiments.

I want to thank all colleagues from the research unit program FOR1766 for the valuable collaboration and support.

I highly appreciated the work and all other activities with my colleagues of the Section of Crystallography, -Mineralogy and the mechanical workshop at the LMU.

My special thanks to my doctorate colleagues Benedikt Röska, Felix Hentschel, Kai Tandon, Iphigenia Anagnostopoulos and Korbinian Schiebel for the close friendship from the beginning of our B.Sc. studies

Finally, I want to thank my family and especially my girlfriend Joy for their love, patience and support during my life as a Ph.D student.